A.I. Alikhanyan National Science Laboratory
(Yerevan Physics Institute)

Vachik H. Khachatryan

AN OXYGEN ACTIVE TARGET FOR LOW ENERGY NUCLEAR REACTION STUDIES

A thesis submitted for the degree of candidate of physical-mathematical sciences in division scientific code: 01.04.16 (Nuclear, elementary particles, and cosmic ray physics)

Scientific Supervisor
Candidate of phys.-math. sciences Amur Margaryan

Yerevan 2019

Table of Contents

Abstract and main points of the dissertation

The dissertation is devoted to an oxygen active target that has been developed for a low energy nuclear reaction studies. It is a position and time-sensitive detector system based on the low-pressure MWPC technique and Si detectors. The few Torr pressure of methylal ($(OCH_3)_2CH_2$) serves as working gas for the MWPC operation, and in addition, the oxygen atoms of the methylal molecules serve as an experimental target. The main advantage of this new target-detector system is a high sensitivity to the low-energy, highly ionizing particles, produced after photodisintegration of ^{16}O, and insensitivity to γ-rays and minimum ionizing particles, thus allowing us to detect only the products of the nuclear reaction of interest. The threshold energy for the detection of α particles and ^{12}C nuclei is about 50 keV and 100 keV, respectively. Timing and position resolution of low-pressure MWPC modules were investigated using an α-particle source and fission fragments in laboratory conditions, as well as, using bremsstrahlung photon beam from MeV Electron beam. The detector system is proposed to be used to:

- Study of the cluster states at 15.1 MeV in ^{16}O using proton beams from the Yerevan proton cyclotron and laser Compton backscattered photon beams at the ELI-NP facility. (Ajvazyan et al. 2018)
- Measure the $^{16}O(\gamma,\alpha)^{12}C$ cross section at HIγS (High Intensity Gamma-Ray Source) with a Low-Pressure MWPC based Active Target
- Study of the decay pion spectroscopy of light hypernuclei at electron and proton-beam facilities, using the recoil distance technique for separation of produced hypernuclei and a magnetic spectrometer for precise measurement of the decay pion momentum. (Margaryan et al. 2019)
- Measure the ionization energy losses and ranges of low-energy alpha particles in methylal and carbon dioxide. (Khachatryan 2019)

Introduction

A brief history of nuclear astrophysics

Every atom in our bodies was created from the nuclear reactions occurred billions of years ago in stars. All atoms that are the building blocks of our body, our bike, on every rock, plant, animal, water and the air we breath owes its reality to far off suns. Those suns are long lived giant stars. The extreme temperatures caused by strong gravity force atoms to collide and merge, creating new elements. In the last stage of their lives these stars will explode, and throw all the byproduct elements millions of miles away spreading them into the Universe over the lifetime of the Galaxy before the solar system itself formed four and one-half billion years ago.

In the process of the Big Bang about 14 billion years ago only three chemical elements - mostly hydrogen and helium and small proportion of lithium were produced. Bye the force of gravity over time the gas molecules were pulled towards each other. Subsequently, the density of the matter started to increase, these made even hotter clouds. The clouds began to gather into clusters known as protogalaxies. Material inside them over time gather even more mass and formed even denser clusters. Most stars were formed from those clusters. In the Milky Way galaxy stars are being born with this mechanism. Inside the stars the heavier elements are fused from lighter atoms mentioned above. In fact changing the lightweight components into heavier ones is what the stars do. In fact, Hans Bethe was one of the founders of explanation of the nuclear fusion processes late in 1939. For this work in 1967 Hans Bethe was awarded with the Nobel Prize in Physics.

The evolution of chemical elements

The bigger the star the stronger the temperatures and pressures so the heavier are the elements it can synthese.The core of our home star, the sun, is about 15

million degrees Celsius which can seems striking. However our sun is ordinary average-size star and it does not get hot enough to forge the heavier atoms than helium. The lifetime of the star depends on its mass. Smaller stars do not explode but rather gently expand due to the collapse of their iron core, the lightweight elements are pushed away and the star is expanding like a growing ball. These small stars such as our sun will swollen and become red giants. For heavier element synthesis than helium, the stars must be at least eight times more massive than our sun, nevertheless they can make up elements up to iron, the 26th element in the Mendeleev periodic table. To make even heavier elements the stars must explode. The end of the massive stars is very different. After burning up all its fuel the core collapses. This increases its internal temperature and density so much that in an instant the elements heavier than iron are forged. Such fast fusion results in releasing so much energy in such small times that it triggers star to expand which stops the synthesis. So the collapsing process starts again, and new elements are produced. These pulsing process repeats several times during a few seconds. The cumulative energy realise in such small time results in self destruction of the star with huge explosion. This fireworks in cosmic scales are called supernova explosions and this is what makes all elements heavier than iron. In the end they become reused by the procedures that structure new stars and even planets. There are many elements in our body which came from supernova explosions. As one of the great astronomers Carl Sagan said, "*We're made of star stuff*".

As a matter of fact, the synthesis of elements heavier than platinum(78th element) and gold (79th element), demands even violent scenarios in cosmic scales: the collisions between stars. For example the collision of neutron stars(even though they are extremely rare) can be possibly an account for all of the gold in the universe.

The mystery of Hoyle state

Life as we know it would not be possible without carbon and oxygen - elements 6 and 8 in the periodic table. Be that as it may, carbon and oxygen

themselves would not exist in sufficient amounts for life without the odd nature of their nuclear structure, which presently can not seem to be completely comprehended. Current theoretical models does not fully explain the excited states - a specific arrangement of nucleons, of their nuclei. The understanding of the nature of these excited states is one of the most seriously explored inquiries in nuclear astrophysics.

About seventy years ago, in 1956, the core ideas concerning the nuclear reaction processes and the overall chemical evolution of the Universe were formulated. Since then advanced works have been conducted both in theoretical and experimental fronts, to identify the cross-section of the nuclear reactions that drive nucleosynthesis.

It is known that four protons fuse together to make helium nucleus (alpha particles) is the beginning of stellar nucleosynthesis. The later fusion of these alpha particles leads to creation of ^{8}Be, ^{12}C, ^{16}O which are two, three and four times the number of neutrons and protons as alpha particles. But there is one problem here. Initially the two alphas should combine to make ^{8}Be, however, beryllium is extremely short-lived, that has only $8*10^{-17}$ s lifetime. Hence these state does not wait until third alpha would fuse to create heavier elements such as ^{12}C and later ^{16}O(Hoyle 1960). The probability of such an event should be extremely low and therefore the observed abundance could not be accounted. This mystery was explained in 1953 by the British astronomer Fred Hoyle. According to Hoyle since we exist and carbon is observed to be fourth most abundant element in the Universe (see Fig.1), there should be some mechanism that would increase the production rate of carbon in stars.

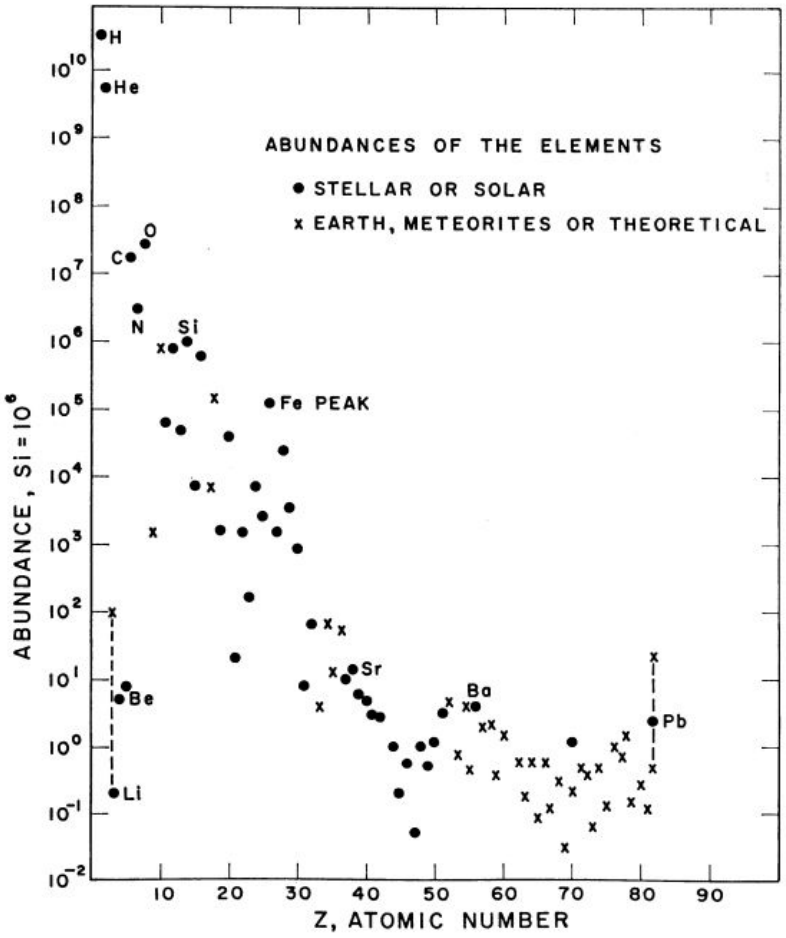

Fig.1 The abundance curve of the chemical elements. Circles are stellar and solar values, taken from Goldberg, Muller and Aller (Goldberg, L., Muller, E.A., and Aller, L.H. 1960). Crosses are from the terrestrial, meteoritic and theoretically adjusted values given by Suess and Urey (Suess and Urey 1956) and Cameron (Cameron 1959). Dashed lines connect elements for which there are large differences in their determinations. Notice that C and O are the fourth and third most common elements. (Greenstein 1961, fig. 1)

This mechanism is similar to the ground and discrete excited states of atoms, however this time it is for nuclei. According to Hoyle the existence of such excited states in ^{12}C serves as a middle of the road step in the carbon synthesis process. This so called "Hoyle state", which by emitting gamma ray would come to ground state would act like a "resonance" that increases by about seven orders of magnitude the

production of ^{12}C. For this to work it is needed that Hoyle state should have specific excitation energy which can be searched experimentally.

It is easy to calculate that the ground state of the ^{12}C has 7.28 MeV more energy than the binding energy of ^{8}Be and alpha combined. This means that if alpha and 8Be combaines at rest energy the ^{12}C nuclei should have 7.28 MeV excitation energy- because of the law of conservation of energy. However, in the hot core of stars these ions are not at rest but rather have thermal energy, which they pass to the ^{12}C when these ions are fused together. According to Hoyle calculations(Burbidge et al. 1957) the energy of this short lived excitation state should be ~7.68 MeV with positive parity and zero nuclear spin.

The initial experiments to find Hoyle state were performed by Ward Whaling from the Kellogg Radiation Laboratory at the California Institute of Technology, who was Hoyle's experimental colleagues (Fowler 1984). The essence of the experiment was to bombard a ^{14}N with deuterons and measure the energy spectrum of alphas and ^{12}C with magnetic spectrometer. By using the conservation of energy they showed that such state suggested by Hoyle actually exists.

So can we state that the carbon production mystery have been solved? In the experimental point of view we can partially say yes, because the rate of carbon with these excited state was increased so it could overcome the fact that 8Be is short-lived and create an abundance of carbon we have today. Nevertheless, this state cannot be explained with either of models of atomic nuclei even after 70 years passed. The nature of the Hoyle state remains one of the most hardest open questions in nuclear physics. (Balantekin 2013)

The theoretical explanations of Hoyle state

Our current understanding of nucleus is based on the nuclear shell model which was formalized in 1949 about four years before the Hoyle state have been found. In a nutshell the shell model says that neutrons and protons act like

independent particles inside the nucleus and fill up shells like electrons do in atoms. This model successfully describes ground and excited states especially in light nuclei such as lowest excited states in ^{12}C. Nevertheless it badly fails for the Hoyle state. None of the predicted states with shell model is close to the Hoyle state and similar states for other nuclei such as Hoyle-like states in ^{16}O. It was suggested that Hoyle state can be better described if we assume that this state consist of clusters of alpha particles. This hypothesis was alluded by Haruhiko Morinaga, particularly he emphasized that Hoyle state can be interpreted as a linear chain of alpha particles(Suhara et al. 2014). Similarly in ^{16}O, ^{20}N and ^{24}Mg should be existing similar states consisted of four, five and six alpha particles. However, it is obvious that this model is an over-simplification, as the alpha particles should be in constant movement because of Heisenberg's uncertainty principle, which states that in the confined small distances the momentum, and so the speed of alpha particles should exceed the value given by the Planck constant. To put it simply, Morinaga's model of clusters shows the time-averaged picture of the dynamic nuclear system.

Current best theoretical models describe the Hoyle state as a gas-like system of weakly interacting alpha particles moving in a larger distances than nuclear scales(Funaki, Horiuchi, von Oertzen, Roepke, et al. 2009). In addition, Hoyle state is also considered to be in a superposition of two states: 70% of three alpha particles and 30% of shell model state (Tohsaki, Horiuchi, Schuck, and Roepke 2017).

There is only one hypothesis that possibly can compete with Morinaga's model. It states that because alpha particles are bosons(have zero spin), they obey Bose statistics and therefore they can form a Bose-Einstein condensate(BEC) in the Hoyle state (Raduta et al. 2011). An alpha particle system with low internal temperature may form a BEC, which is like the atomic condensates. Many questions arise while considering this idea. It is not clear how the theory of atomic condensates can be applied to the nuclear condensates, if they exist.

Solving the properties of nuclei from first principles requires a theory of proton-neutron interaction in nuclei and numerical solution of many body Schrodinger equation.The first one was described by S. Weinberg in 1990 and called

"chiral effective field theory"(Weinberg 1990). The second one still requires enormous computer power, but nowadays many exciting simulations were carried out. The first solely theoretical calculations of Hoyle state was performed in 2011 by E. Epelbaum using Lattice Monte Carlo simulation and Weinberg's approach - the quark gluon theory - for nuclear interaction. The state with zero spin and positive parity and around 7 MeV above ground state, that they found, appears to be the Hoyle state. In 2012 they published another paper where alpha cluster structure was emerged from their calculations. In his work Epelbaum stated that in the ground state of the ^{12}C alpha particles are arranged in a compact triangle (Epelbaum et al. 2012), whereas in the Hoyle state they are in a bent arm configuration(Fig. 2).

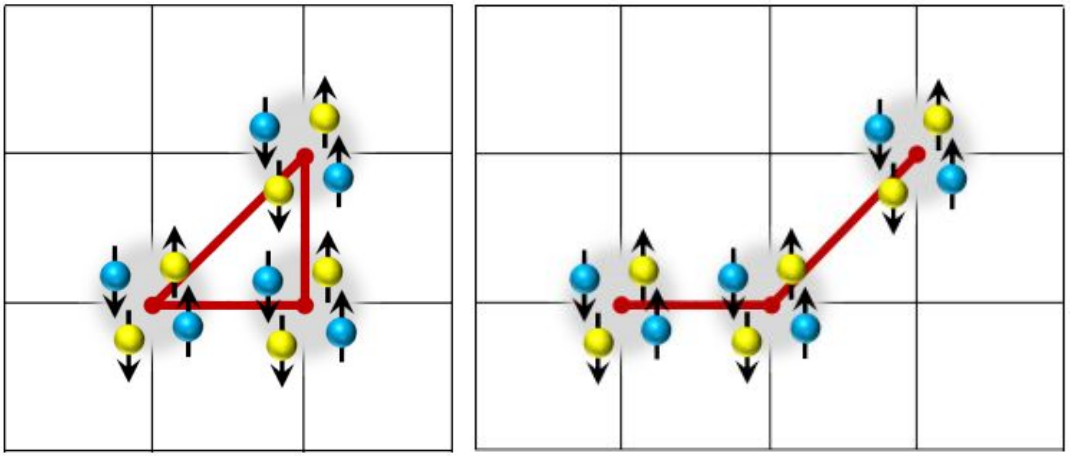

Fig. 2. The structure of the Hoyle state according to Epelbouer's work.
a) comact triangle - ground state of the 12C b) bent arm - configuration corresponds to Hoyle state

Although the energy of the Hoyle state experimentally has been determined by 0.05% from very rare decays (7 events out of 106) experiments are now beginning to provide clues for its true nature. One promising way of describing the Hoyle state is so called rotational excitations of the Hoyle state. This idea goes back to 1956 and belongs to Morinaga. According to him, the Hoyle state can represent the linear chain system of alpha particles, and like molecular chain it could have discrete rotation. For

each discrete state there should be a rotational energy levels with 2^+, 4^+, 6^+, etc spin and parity. The moment of inertia of those levels could indicate the compactness of arrangement of alpha particles. No matter the importance of the problem and the efforts the experimentalists have been put on it, the search of rotational excitation states still continues. One of the significant results was the identification of 2^+ state by M. Freer and his team (Freer et al. 2009).

Nuclear reaction rates play a critical role in the understanding of stellar evolution and explosions. However, in many cases nuclear reaction rates still carry large uncertainties due to the paucity of experimental data and incomplete theoretical understanding of the underlying reaction mechanisms. New experimental methods and techniques, combined with the development of new theoretical tools, have exposed fresh avenues to pursue nuclear reactions of significance for nucleosynthesis at, or near, the actual temperatures of stellar burning. Nuclear astrophysics has entered a period characterized by unprecedented demands for new information and for improved accuracy. This challenge is being driven by the quality and breadth of current observational data, a direct consequence of impressive advances in observational technology.

This thesis provides an overview of the most critical nuclear reactions for a number of nucleosynthesis environments and suggests some new methods to overcome the difficulties from experimental point of view.

Chapter 1:

The Multi-Wire Proportional Chambers

Ionization chambers

The ionization chamber is a gas detector with the help of which the ionization losses of charged particles are recorded. The measurements are carried out by recording a signal from charged couple, which is generated on anode and cathode electrodes. If the particles is fully absorbed in the chamber, the full energy of the particle can be reconstructed. In the simplest case, the ionization chamber consists of a parallel electrode system. The voltage given to them forms a homogeneous electric field. The pair of electrodes are placed in a gas-filled chamber where the electrons and ions can perform a drift movement. Instead of gas, it is sometimes used as liquid or solid materials, but this does not affect the overall structural features as such.

Let's assume that charged particle with X_0 distance from the anode, is moving parallel to the electrodes. Depending on the particle type and energy it is ionizing the gas. U_0 voltage is taken so that no gas amplification occurs (Grupen and Shwartz 2008):

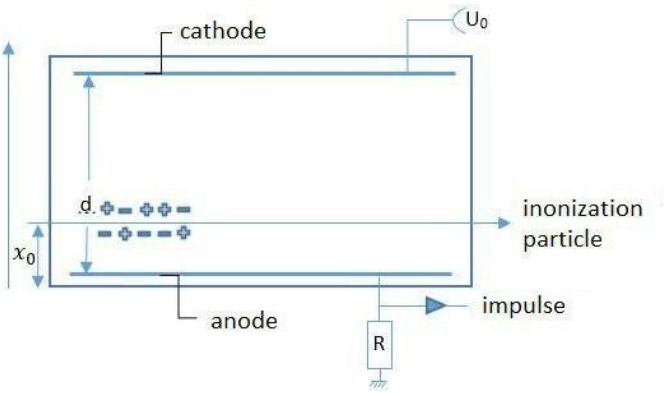

Fig. 3. The principle of the ionization chamber operation

The electric field inside the chamber is given

$$|\vec{E}| = E_x = \frac{U_0}{d} = const \quad (1)$$

We also assume that the resulting charge is fully transferred to electrodes, secondary ionization processes are absent. The charged particles reach the electrodes and charge the system as a capacitor. The capacitor discharging (passing through R resistance) generates a signal that is processed by the preamplifier. Suppose N pair of charged particles emerge along the ionizing particle movement. If we prescribe the capacity of the capacitor with C and take into consideration that it is discharged due to moving charges, from U^0 to U and the accumulated energy drops from $\frac{1}{2}CU_0^2$ to $\frac{1}{2}CU^2$

$$\frac{1}{2}CU^2{}_0 = \frac{1}{2}CU^2{}_0 - N\int_x^{x_0} qE_x dx \quad (2)$$

$$\frac{1}{2}CU^2{}_0 - \frac{1}{2}CU^2 = \frac{1}{2}C\left(U_0 + U\right)\left(U_0 - U\right) = -NqE_x\left(x - x_0\right) \quad (3)$$

However, the decline in voltage will be insignificant

$$U + U_0 = 2U_0 \qquad U_0 - U = \Delta U \qquad (4)$$

Placing $E_x = \frac{U_0}{d}$ We get.

$$\Delta U = -\frac{Nq}{Cd}\left(x - x_0\right) \qquad (5)$$

The signal width depends on the cumulative signals from ions and electrons. If v^+ and v^- are the drift velocity of ions and electrons, then we have

$$\Delta U^{\pm} = -\frac{Nq}{Cd} v^{\pm} \Delta t^{\pm} \qquad (6)$$

($\Delta t^{\pm}$ is corresponding times fro ions and electrons)

Because the $v^+ << v^-$ the signal width would increase becoming

$$\Delta U_1 = -\frac{Nq}{cd}\left(-x_0\right) \qquad (7)$$

And then when ions reach the cathode the width of the signal would increase by the amount of

$$\Delta U_2 = -\frac{Nq}{cd}\left(d - x_0\right) \qquad (8)$$

The overall width of the signal would be the sum of above two equations

$$\Delta U = \Delta U_1 + \Delta U_2 = \frac{Ne}{Cd} x_0 - \frac{Nq}{Cd}\left(d - x_0\right) \qquad (9)$$

And considering that $q = +e$

$$\Delta U = -\frac{Ne}{C} \qquad (10)$$

Thus we have that the width of the signal does not depend on the distance x_0 .

The Proportional chambers

There is no gas amplification in the ionization chambers, meaning that the number of initially born charged particles does not increase. However if the energy for initial electrons that have been created from the ionization of the primary particle is enough to create new electrons capable of ionizing the medium, then avalanche occurs. This can be achieved if between the anodes and cathodes wires voltage corresponding to a few hundred volts per millimeter is applied. Because there is no time delay before the avalanche(see Fig. 4) occurs, the resulting signals have good timing properties, with the rise and fall times of a few nanoseconds, as compared with other types. The width of the impulse is determined by the equation

$$\Delta E = -\frac{eN}{C}A \quad (11)$$

where A is the gas amplification coefficient.

The linear gas amplification of the detector is due to the fact that the gas amplification coefficient A is constant, and the measured amplitude of the signal is proportional to the ionization. The number of pairs generated by electrons during the avalanche in the unit length is called the first Townsend coefficient(Townsend 1915, 1947; Loeb 1960) and is denoted as α. If the ionization cross section is σ_{ion} than

$$\alpha = \frac{\sigma_{ion} N_A}{V_{mol}} \quad (12)$$

where N_A is Avogadro's constant, and V_{mol} is the molar volume of the gas.

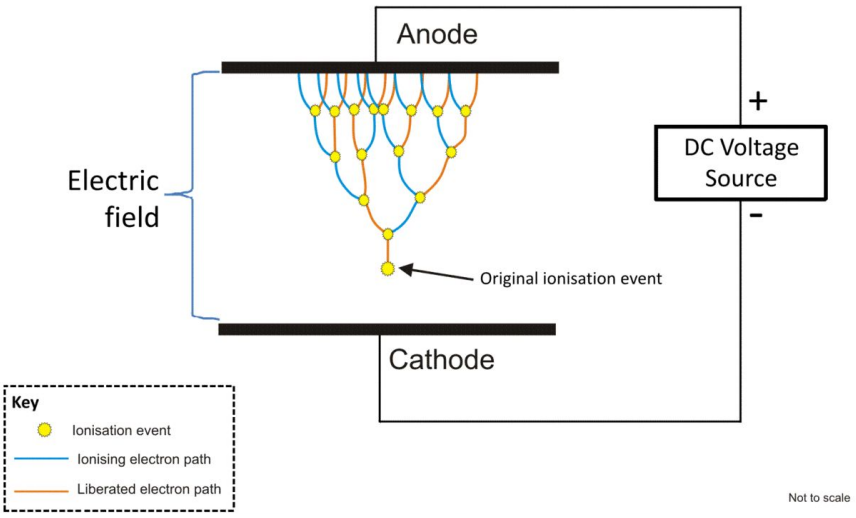

Fig. 4 Visualisation of Townsend avalanche (taken from (Wikipedia contributors 2019).

If N_0 is the initial number of electrons the N number of charged pair in the point x will be determined with the following equation.

$$N(x) = N_0 A = N_0 e^{\alpha x} \quad (13)$$

If the applied U_0 $>>U_{th}$ where U_{th} is the threshold voltage for the detector, than the gas amplification constant can be written as

$$A = \text{const} \cdot e^{\frac{U_0}{U_{ref}}} \quad (14)$$

Where U_{ref} is some constant depending from gas parametres.

In the case of MWPC detector, however, the primary electrons are uniformly distributed along the trajectory of a particle, with $\rho(z) = N_0/D$ ($\rho(z)$ represents the density of the number of primary electrons along the particle trajectory), where D is the distance between the cathode and anode plates (Kumagai et al. 2013). Therefore, the integrated number of avalanche electrons N becomes

$$N = \int_0^D \frac{N_0}{D} exp(\alpha z)\, dz = \frac{N_0}{\alpha D}\{exp(\alpha D) - 1\} \quad (15)$$

Because $e^{\alpha D} >> 1$

$$N = \frac{N_0}{\alpha D} exp(\alpha D) \quad (16)$$

If we put x = D we will get that

$$N \rightarrow \frac{N_0}{\alpha D} \quad (17)$$

The coefficients D = 3 mm and α = 30 cm^{-1} (corresponding to a mean-free path of 0.3 mm for ionization), which are typical parameters for our LPMWPC detectors, resulting in αD ≈e^9 ≈8000.

The Low Pressure Multi-Wire Proportional Chamber (LPMWPC) Detector.

Construction of single units

The LPMWPC is a proportional counter with three electrodes (two cathodes and one anode) having parallel-plane symmetry. The operational mechanism of the LPMWPC combines the principles of a regular multiwire proportional chamber (MWPC) and a parallel-plate avalanche counter (PPAC). MWPCs (Charpak and Sauli 1979)that operate at normal gas are not suitable for time measuring, because their time resolutions are typically on the order of several tens of nanoseconds. This is due to the long drift time of electrons, released in the sensitive volume towards the sense wire, where amplification occurs. The first measurements at low pressure (P =3 Torr) have shown that a time resolution of about 2.5 ns (FWHM) could be reached with 5.5 MeV α-particles (Binon et al. 1971). This result was simply attributed to a faster drift time at higher reduced fields. Further investigations (Breskin, Chechik, and Zwang 1979; Overbeck et al. 1990; Assamagan et al. 1999) have clearly shown that the amplification mechanism at low pressure is entirely different. In this section the detailed construction process of LPMWPC is described.

At first the LPMWPC modules were designed and prepared and developed in AANL and Yerevan Telecommunication Research Institute. The detector module consists of two wired-cathode and three wired-anode plates stacked on top of each other. The designed anode and cathode plates with their dimensions are depicted in

Fig. 5. The electrodes are made of G10 (epoxy) with a thickness of 3 mm, which is also the plane spacing. The designed plates then were cut and processed to make sure all edges are smooth to make wiring easy. Then several times it was cleaned with acetone, alcohol, and distilled water to avoid the emerging unwanted gases when running the vacuum.

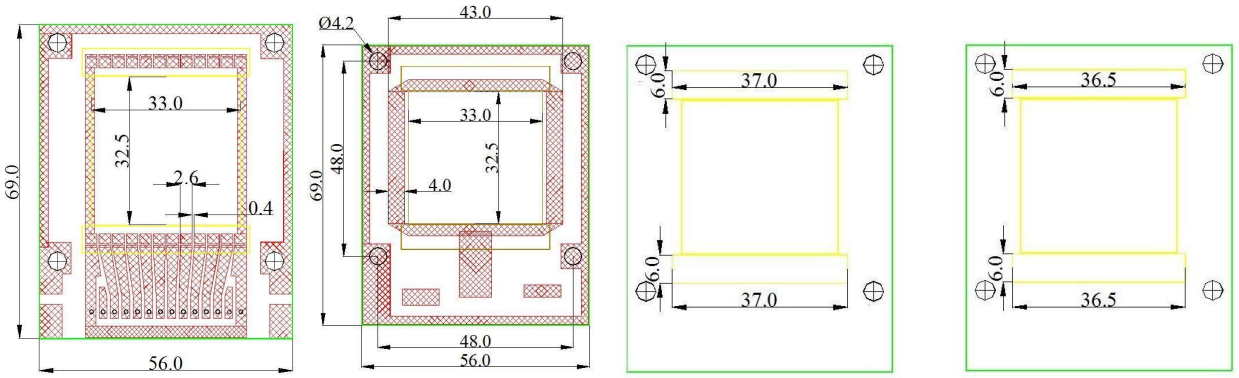

Fig.5. The schematic view of cathode and anode planes from left to right.

Specific equipment was used which is based on equal space bolt stand to provide 1mm spacing between wires in anode and cathode. To make the wires very tight with the same tension 50g loads were hanged from every pair of wires and soldered together. Because of the 20-micrometer diameter, gold-plated tungsten wires were used, they were broken from slightly high tension making the whole process to start again. On every step of assembling either the wires or the soldering electronic components, the remaining of t he soldering oil were carefully removed with acetone, then with alcohol and distilled water several times. Even the tiniest dust particles or oil in the wires can cause bad signals on the output. All planes have a wire spacing of 1mm. The anode plane used 20 μm diameter gold-plated tungsten wire, while the cathode and guard planes used 40 μm diameter copper-beryllium wires (the process is depicted step by step in Fig.6, the schematic view is in Fig.7).

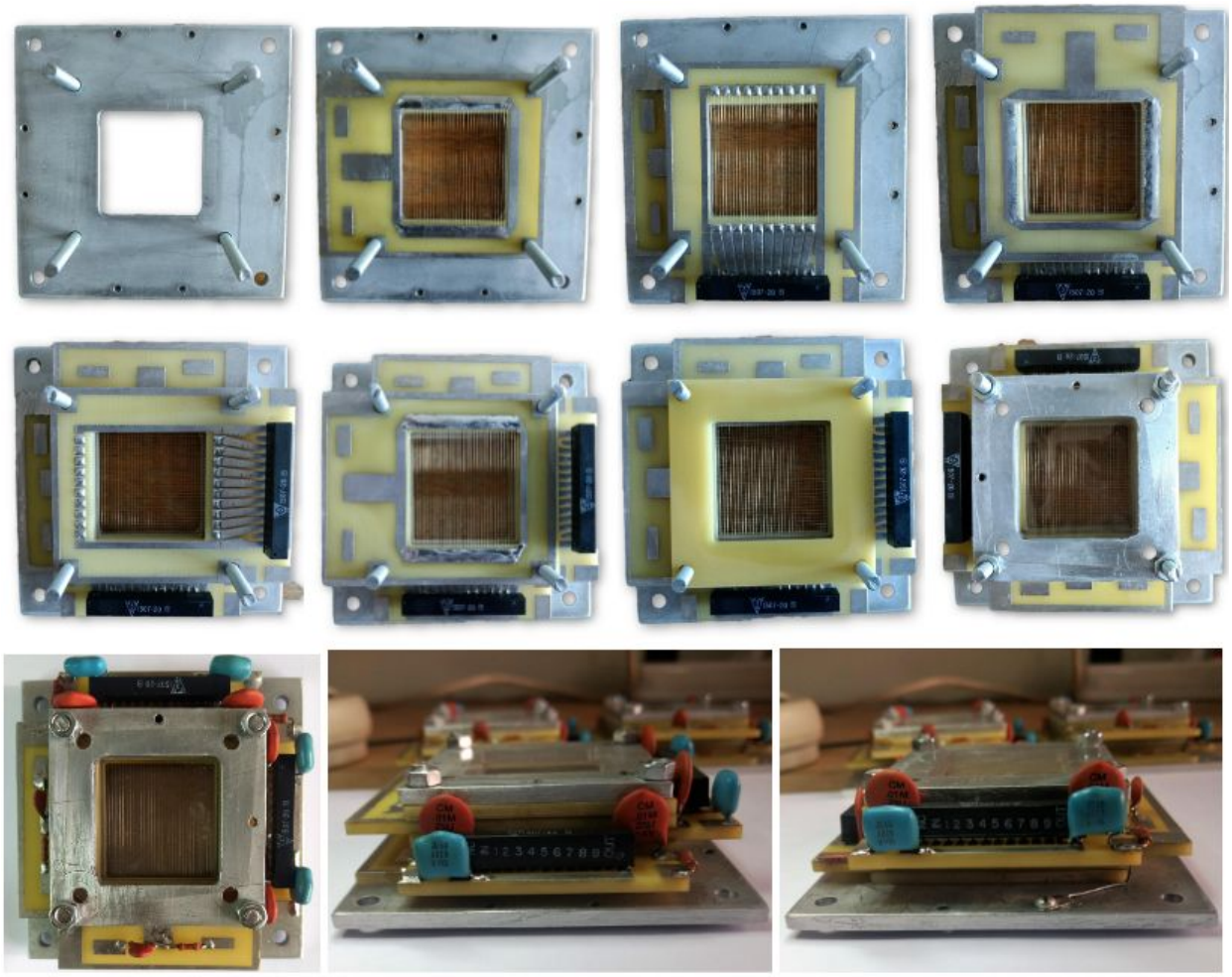

Fig. 6. Step by step assembly of MWPC single unit.

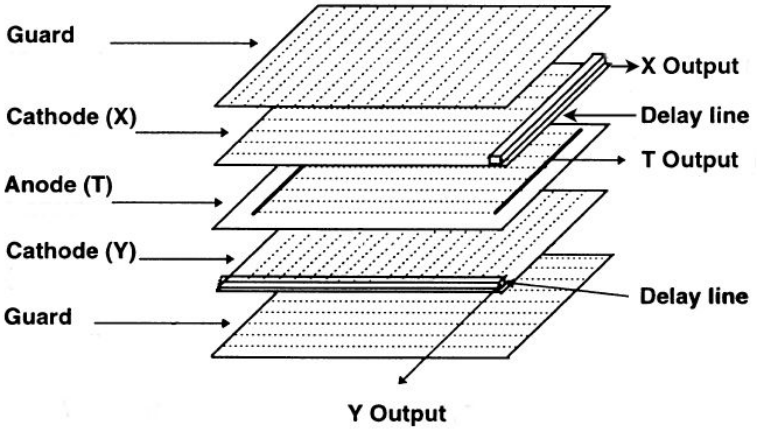

Fig. 7: Schematic diagram of the single unit of MWPC.

Groups of three cathode wires are connected to tapped delay lines (2 ns/tap) to provide position information using the method of time difference. This readout provides ~1 mm position resolution. Tap by tap readout would allow position reconstruction with sub 100μm precision. However we used the time difference between the anode pulse and induced cathode pulse propagating towards the end of a delay line, because ~1 mm resolution satisfies the requirements of the planned experiments.

Schematic drawings of the anode and cathode electrodes showing the readout of time and position signals are presented in Fig. 8 and Fig.9 respectively.

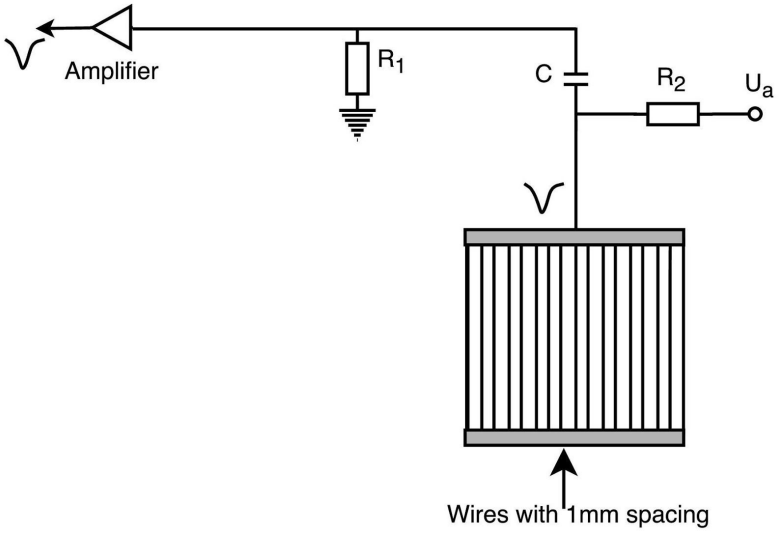

Fig. 8. Schematic of the anode plane readout: R1 = 150 Ω, R2 = 1 MΩ, C = 260 pF.

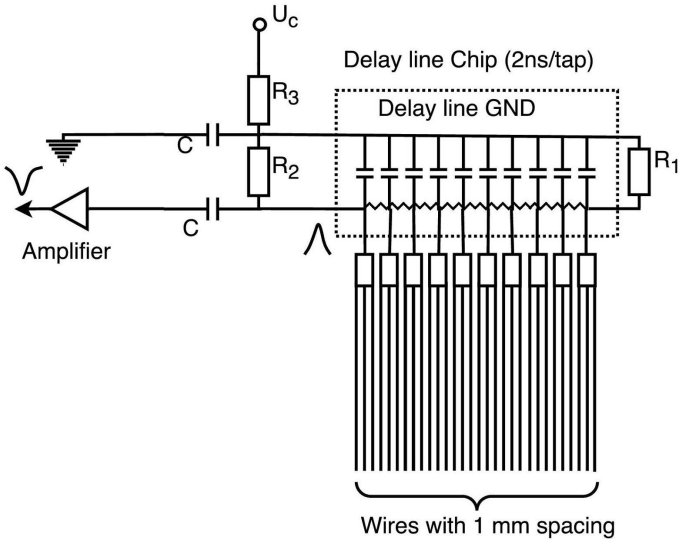

Fig. 9. Schematic of the cathode plane readout: R1 = 100 Ω, R2 = 10 kΩ, R3 = 1 MΩ, C = 10 nF.

The positive signals induced on the cathodes are used for the position (x, y) read-out, one coordinate from each plane. The two outer wire planes function as guard planes against electrons from ionization taking place outside of the chamber region, and as additional electrodes to provide double step amplification.

Development of test setup

A test experimental setup was developed in order to investigate the operational modes of the LPMWPC units and to measure the timing and position characteristics using a 0.14 mg/cm^2 thick, 30×30 mm^2 Pu-239 α-particle source, which has three lines: 11% - 5.099, 20% - 5.137 and 69% - 5.150 MeV. It consists of two MWPC1 and MWPC2 units, mounted at 5.5 cm distance from each other. Mylar absorbers with 1 mm diameter hole in the center were used to collimate the α particles(see Fig. 10).

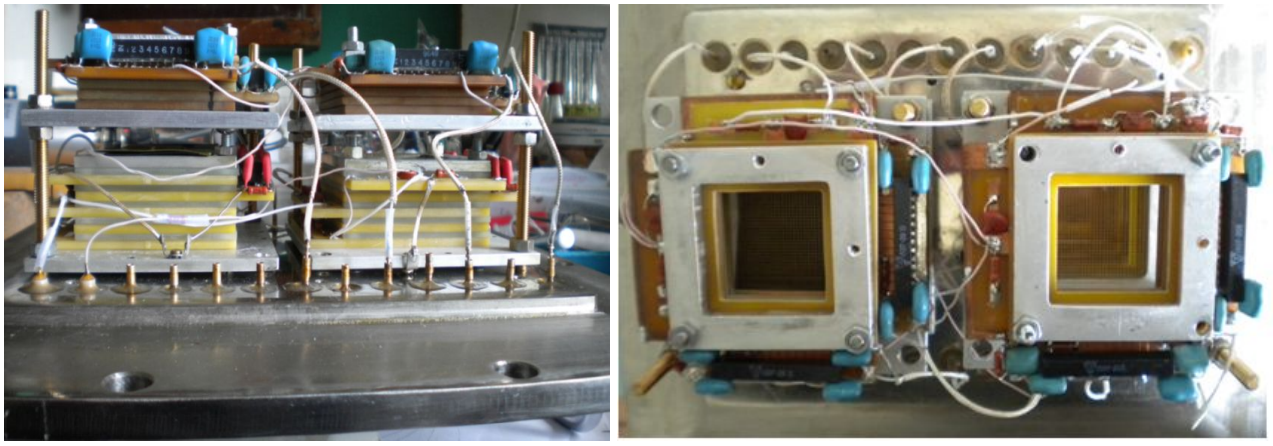

Fig. 10. The side and front view of LPWMPC test setup. The detector system was placed in vacuum valve.

Using this setup time and position resolutions and dE/dx distributions in the MWPCs were studied. The geometry of the test setup is shown in Fig. 11.

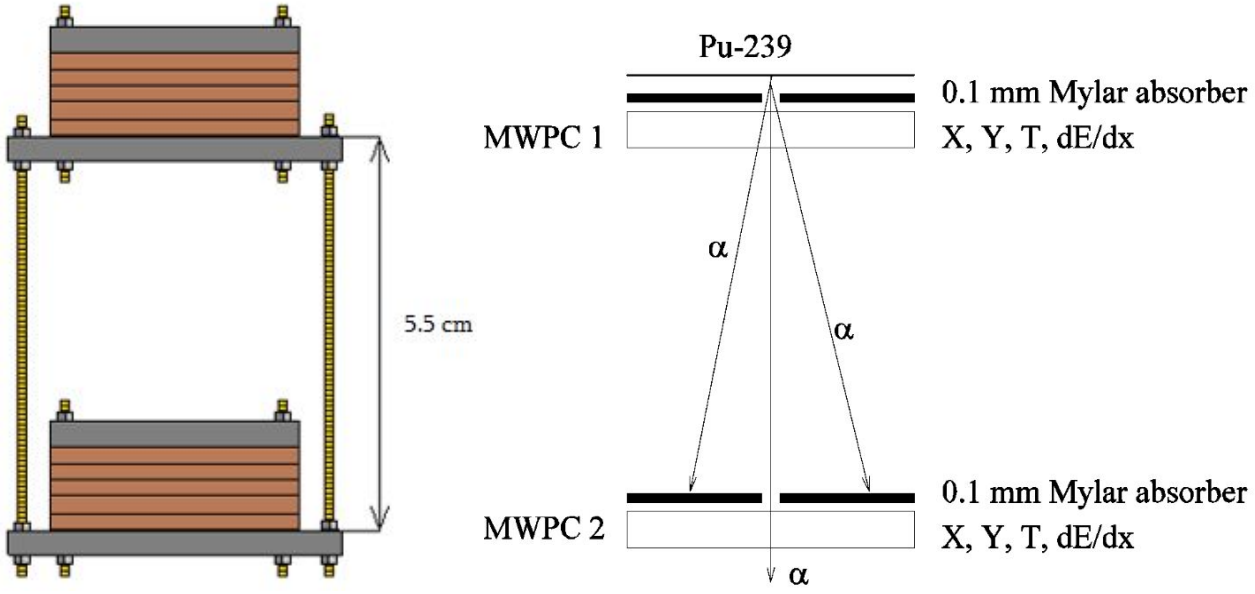

Fig. 11. Schematic representation of the test setup.

The MWPCs and SSDs are mounted in a rectangular vacuum chamber (Fig. 12), which has windows for beam entrance and exit. Lemo connectors, fastened on the walls of the vacuum chamber, provide access to electronics outside the vacuum chamber. The chamber can operate from 2-10 Torr of methylal vapor.

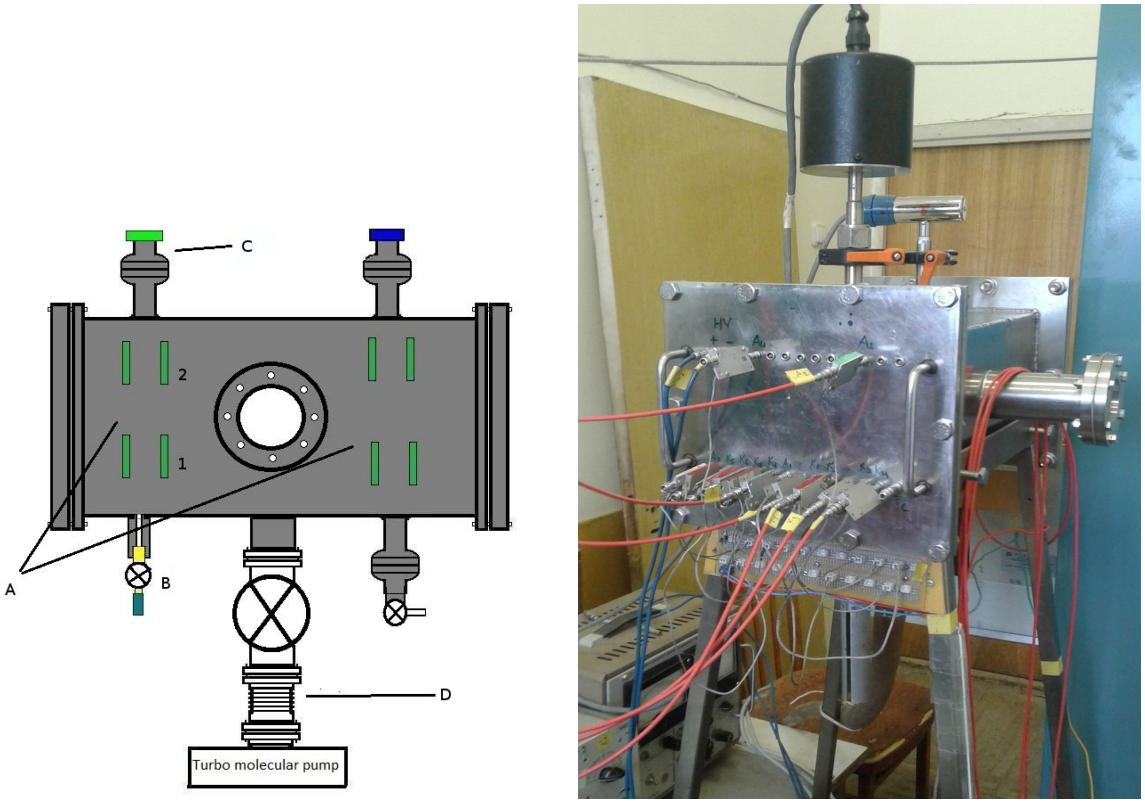

Fig. 12. Schematic and real appearance of the detector. A - LPMWPC modules, C - vacuum gauge meter, B- Methylal gas, D - vacuum pump.

High-frequency transimpedance amplifiers for LPMWPC

For amplification of the resulting signals with a high ratio of the signal by the noise four types of high-frequency transimpedance amplifiers with different magnification factors has been designed and manufactured. To ensure a wide spectrum of frequencies, the "Texas Instruments" high-band and super-low noise operational amplifier chips were used. In addition, these amplifiers differ in input and output signals.

At the entrance of the first type of amplifier ~5 ns negative signal was given, and the output signal out of 50-ohm load comes negative 150 times amplified.

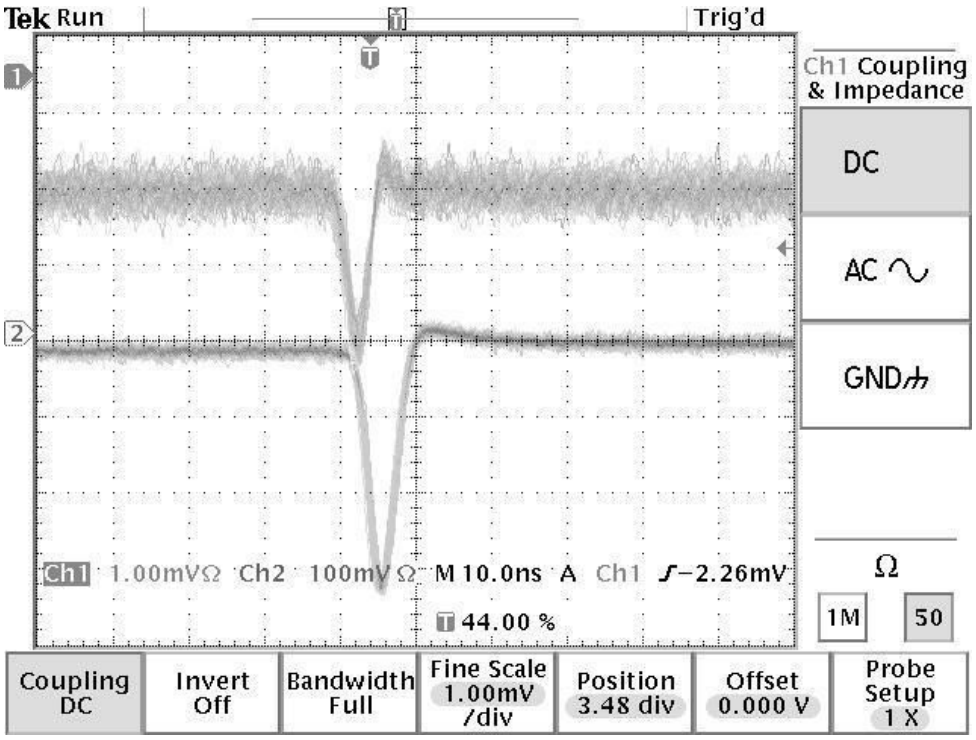

Fig. 13. The input and output signals of the first type amplifier registered on a digital scope.

The second type amplifier is given a positive signal of ~5 ns, and the output signal out of 50-ohm load comes negative 250 times amplified. The amplifiers are powered by a ± 5 V voltage and use about 30 mA current.

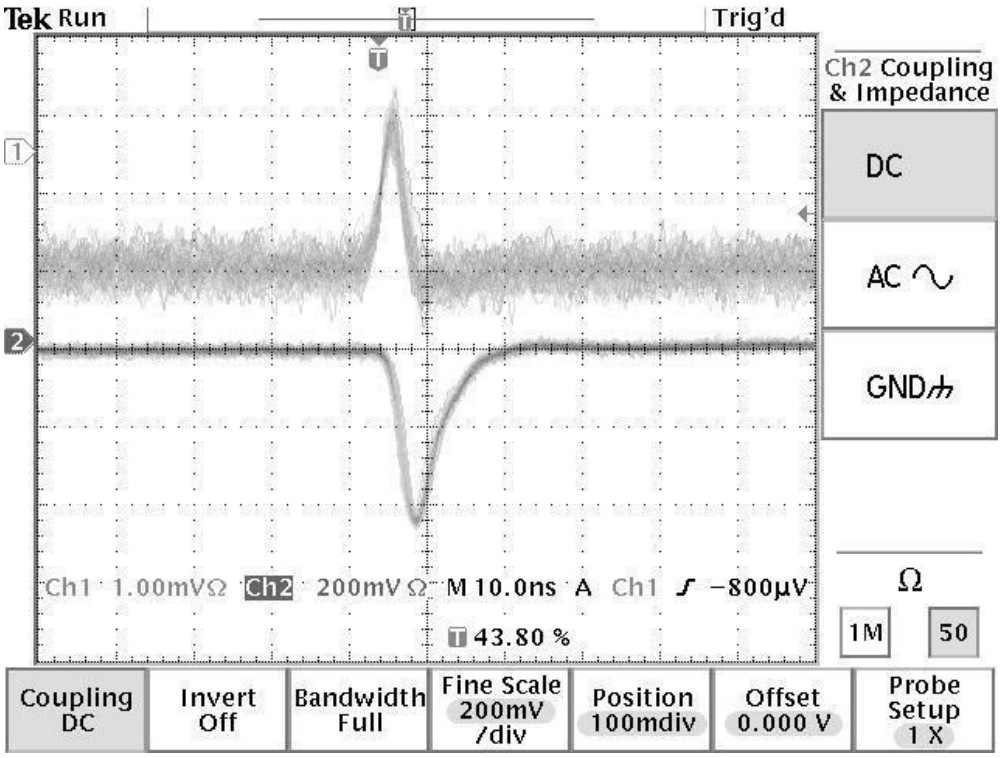

Fig. 14. The input and output signals of the second type amplifier registered on a digital scope.

At the entrance of the third-generation amplifier, a sine wave signal is given, and at the output of 50-ohm load, we receive a sine wave signal approximately 100 times amplified. The frequency range reaches to about 350 MHz.

The fourth type of amplifier is made with an amplification factor of 30, 40 and 50 times. At the entrance of the fourth type of the amplifier ~ 5 ns negative signal was given, and the output signal out of 50-ohm load comes also negative.

Because the anode impulses are negative and relatively large, the amplification factor has been chosen to be ~500:600 times. The signals coming from cathode planes are positive and small. Thus the signal coming from cathode thave been amplified 1000 times(see Fig 15, 16)

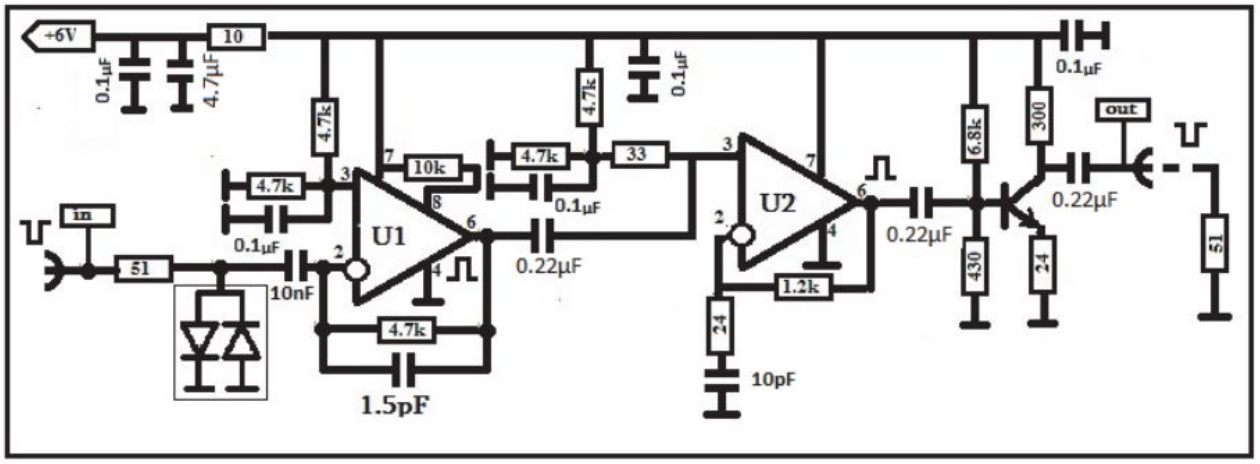

Fig. 15. Amplifier scheme for signals from the anode plane. (Vardanyan 2017)

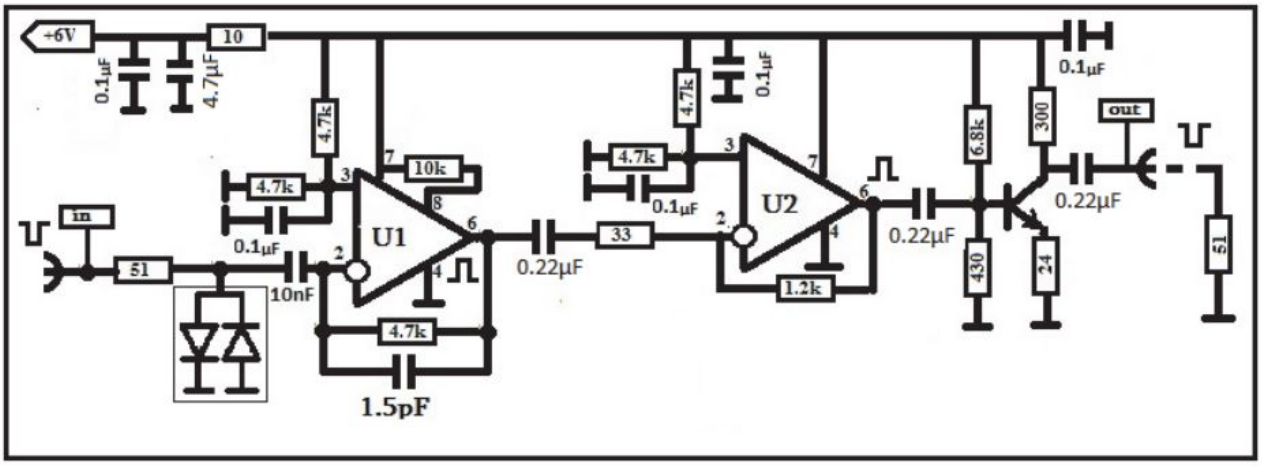

Fig 16 Amplifier scheme for signals from the cathode plane. (Vardanyan 2017)

Below the linearity of amplifiers is presented. Demonstrating that the amplifier working with the negative input signal (which is the main scheme) is quite linear and by increasing the source voltage it remain mainly linear in working range.

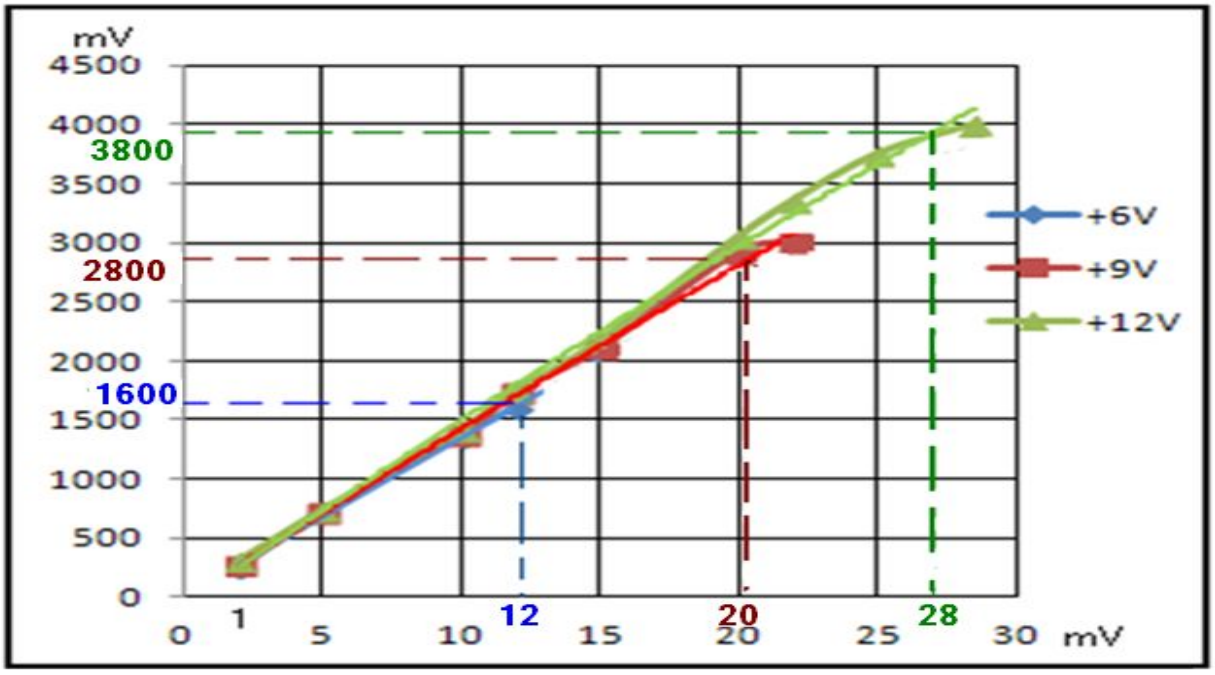

Fig.17 The linearity of the amplifiers depending from source voltage

The power supply of this type of amplifier runs from +6 Volt voltage. The amplifiers then were fitted in an aluminum box of 40x22x5mm^3.

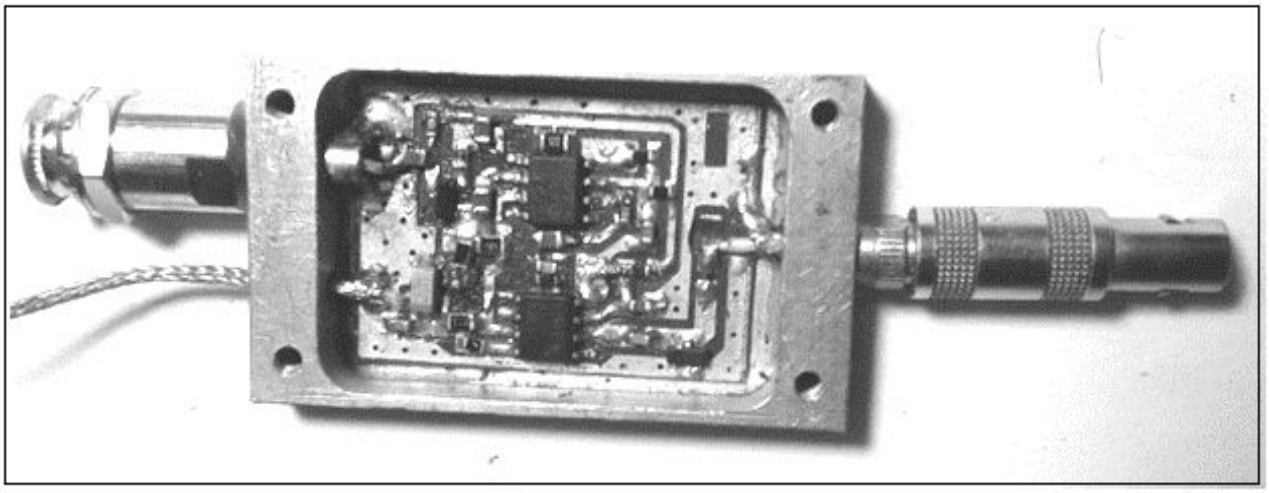

Fig. 18 The real view of amplifiers. The output and input are realized via LEMO connectors.

In addition to the LPMWPC's, the semiconductor detector is also supposed to be used. That's why there was a need to design and prepare a spectrometric amplifier

with large input resistance (Fig. 19) . In the basis of the high-speed amplifier circuit, the BF862-field transistor with super-low noise (0.8nV/Hz) was added to the input.

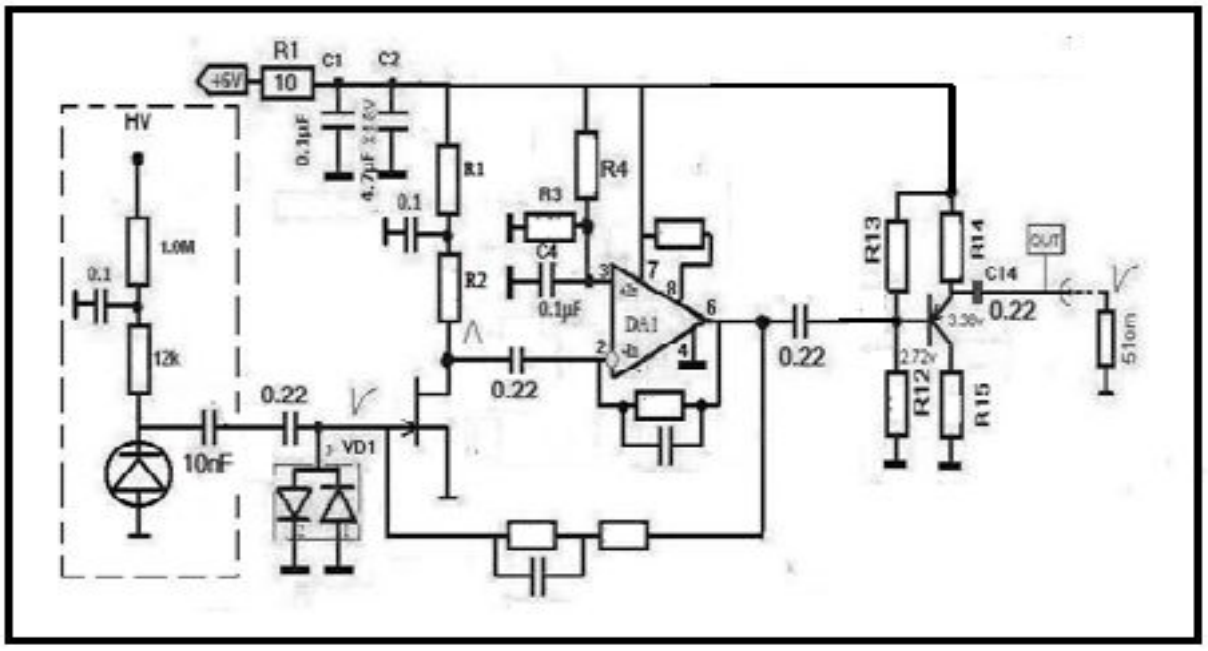

Fig.19 The block scheme of the spectrometric amplifier with amplification coefficient of 16 times.

The energy spectra of alpha particles was measured from 235U (see Fig. 20) and 238Pu(see Fig, 21) sources. The measurements were carried out in a black box to minimize the light intervention to Si detector. The signals were processed online via Labview Software.

Fig. 20 The energy spectra of Si semiconductor detector from 239Pu source

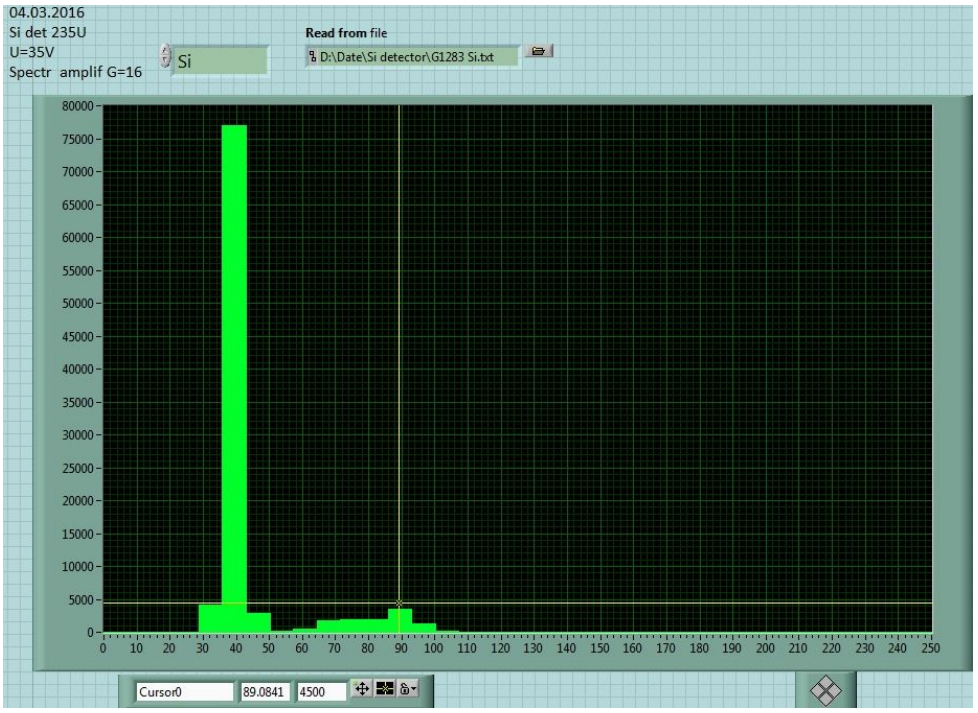

Fig. 21 The energy spectra of Si semiconductor detector from 235U source

Chapter 2

Test experimental results of Multi-Wire Proportional Chambers

The electronics of the experimental setup

The fast, ultra-low-noise amplifiers for amplification of nanosecond signals from the anode and cathode wires and SSDs are mounted outside the vacuum chamber. The chamber can be evacuated to a pressure of 10^{-3} Torr and is equipped with valves for gas handling and two pressure gauges. The chamber volume, connected to a reservoir of liquid methylal ($(OCH_3)_2CH_2$), hexane (C_6H14), or heptane C_7H_{16} with a reducing valve, and it was filled with a 2-3 torr vapour.

The low-pressure MWPC system can operate in the so-called single-step and double-step modes (Margaryan et al. 2010; Breskin, Chechik, and Zwang 1980; Assamagan et al. 1999) and references therein). In the case of single step the typical potentials applied to the anode, cathode, and guard planes are U_a = +400, U_c = -100 and U_g = 0 V respectively and the resulting signals from the α-particles have a few 10's of mV amplitudes. In the case of double step, the typical potentials are U_a = +300, U_c = 0 and U_g = -300 V respectively and amplitudes of the resulting signals increased by an order of magnitude, compared to the single-step case. The typical signals from anode and cathode planes generated by α-particles in MWPC1 (double-step operational mode) and registered by 500 MHz oscilloscope (ROHDE&SCHWARZ HMO 3004 Series) are shown in Fig. 22. The diagram of the signal readout and data acquisition electronics is shown in Fig. 24.

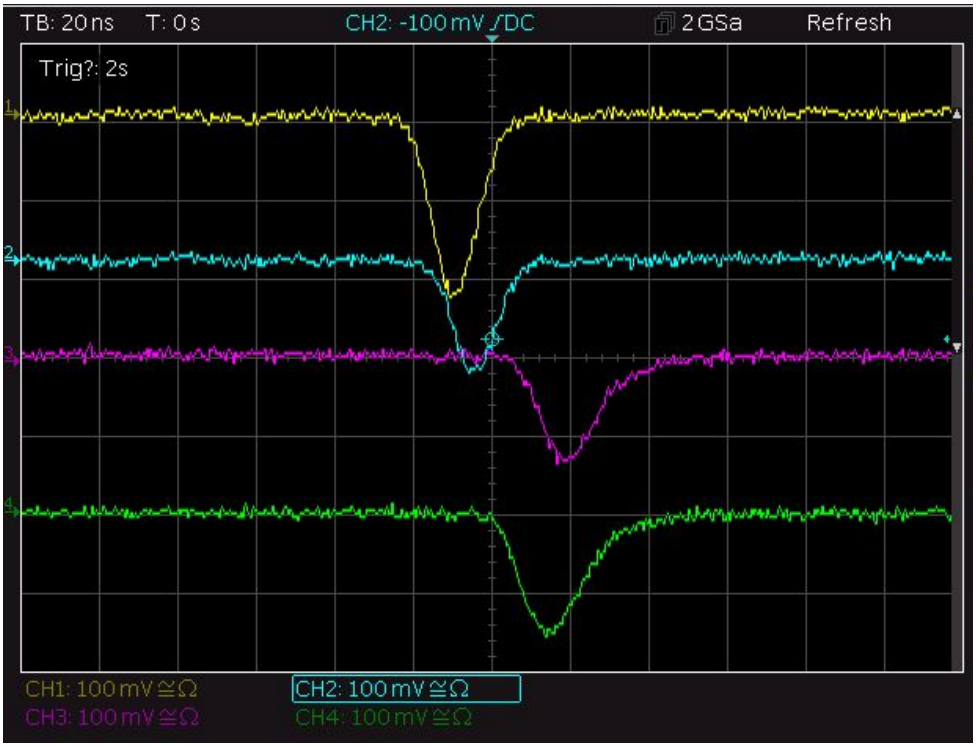

Fig 22. Typical signals from anode and cathode planes after amplification for operating conditions: Methylal 3.3 Torr, +300 V on the anode, 0 V on the cathodes and -300 V on the guard planes. Trace 1 (yellow), 2 (cyan): signals from anode planes of the top and bottom MWPC units. Trace 3 (magenta), 4 (green): signals from two cathode planes of the top MWPC unit. The time scale is 20 ns/division and amplitude scale of 100 mV/division.

For time measurement all signals are connected to Constant fraction Discriminator (CFD) to exclude the effects of amplitude changes. From Fig 23 we can see the electronics and logic of the detector system assembled via CAMAC crate:

Fig 23. The electronics of the detector system in the lab room.

In the right side of the Fig. 23 is the vacuum chamber inside which the LPMWPC are placed. The signals are extracted with signal wires(red) and connected to CAMAC crate(middle) and oscilloscope. In the scope we monitor signal shapes online, give threshold and write files to computer memory if everything is alright. In the CAMAC crate the signals are processed, digitized and transfer to the computer(left) where we can see the online histograms of the signals.

The signals are connected to the Analog to Digital Convertors(ADC-Lc2249A) and Time to Digital Convertors (TDC-Lc2228A) (Fig. 24)

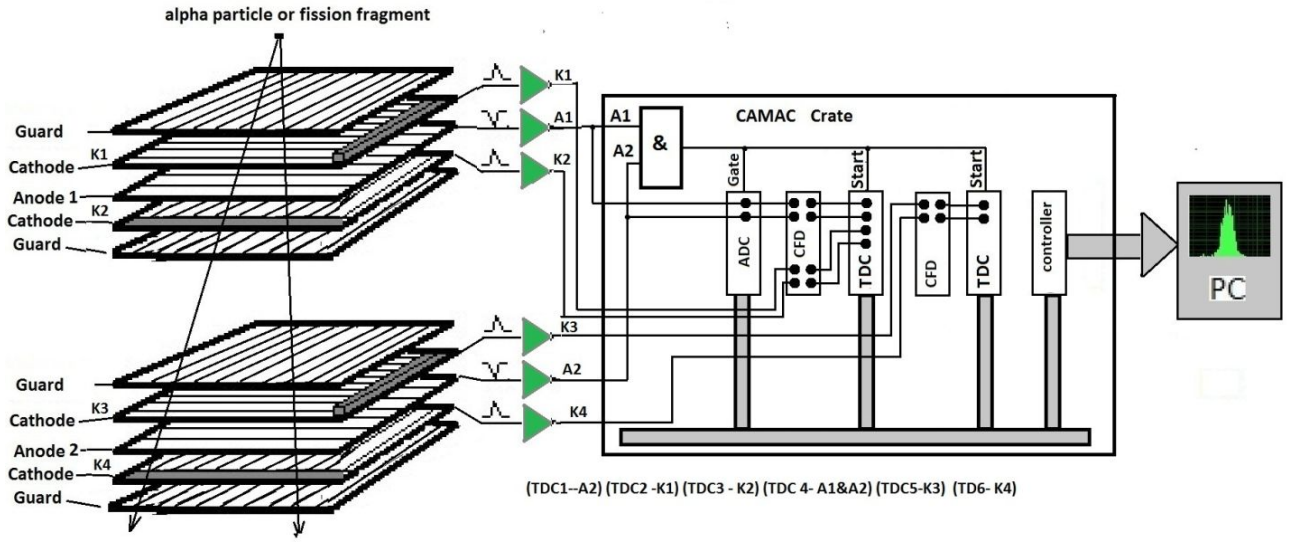

Fig. 24. The block scheme of detector system.

Two start signals, Start1 and Start2 are formed by using coincidences of anode signals from MWPC1 and MWPC2, where the timing of the Start1 and Start2 signals is determined by the MWPC1 and MWPC2 anode signals, respectively. These start signals are used for measuring the time difference between the two anode planes (time-of-flight (TOF) timing resolution) and between the anode and corresponding cathode planes (position measurement resolution) of the MWPC1 and MWPC2 units. A copy of the Start1 signal is also used to generate an ADC Gate signal for digitizing of both anode signals.

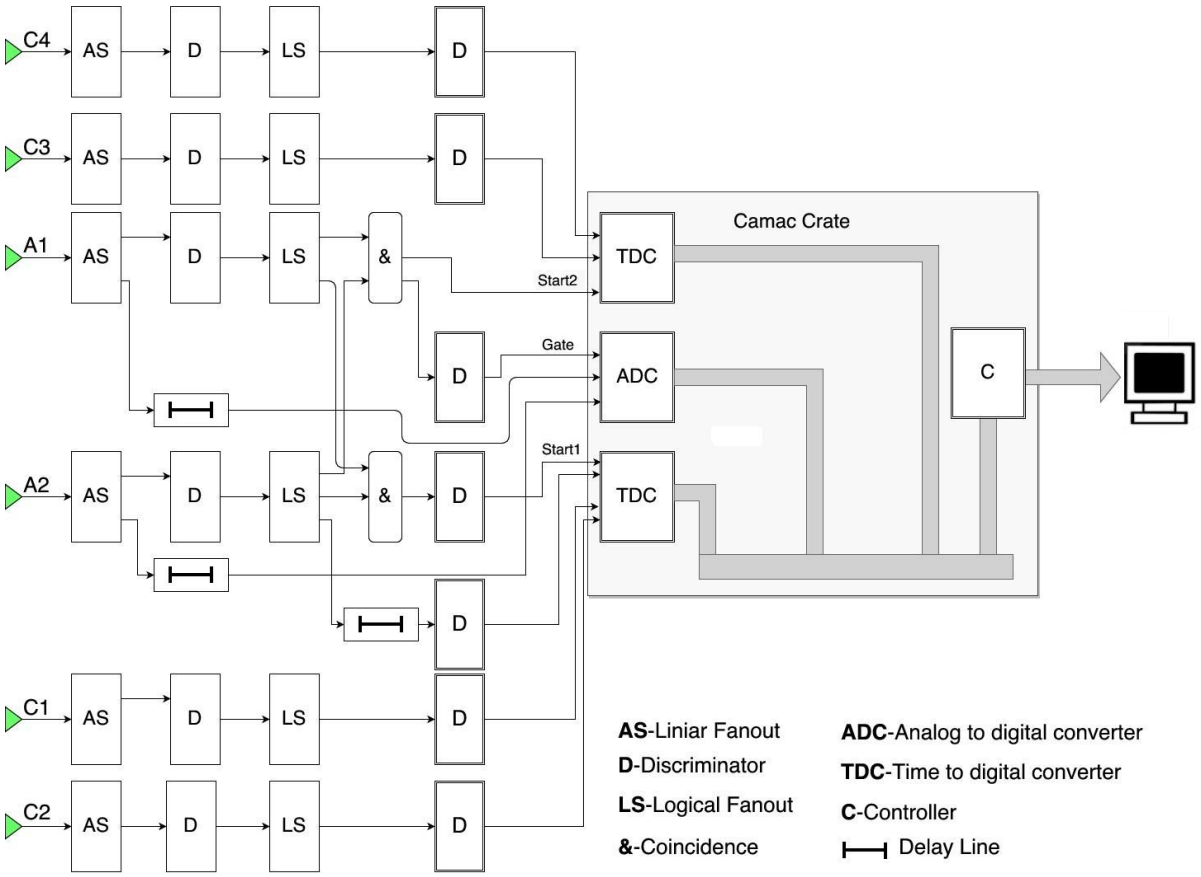

Fig. 25. Block diagram of electronics.The C1-C4 are the cathode signals the A1-A2 are the anode signals coming from MWPC corresponding planes.

From the TDC data the time difference distribution of the particle flying from one module to another is being reconstructed. This can be normalized to build the velocity spectrum of particles. In the other hand signals from ADC can be used to reconstruct the energy losses left by the particle in the detector's volume(dE/dx). After collecting all statistics, all data is transferred to the computer using Lc 8901A Controller. A LabView software have been written to read and write the data into files for later analysis, and simultaneously recreates the histogram of all channels. The data is being written in the .txt file as 8 different columns. Each column represents the channel number of the digitized value. One channel pixel corresponds to 50 ps.

In the Fig. 26 the laboratory test results are depicted for the timing coordinate and amplitude distributions. The tests have been carried out for different radioactive sources, detector pressure and voltage.

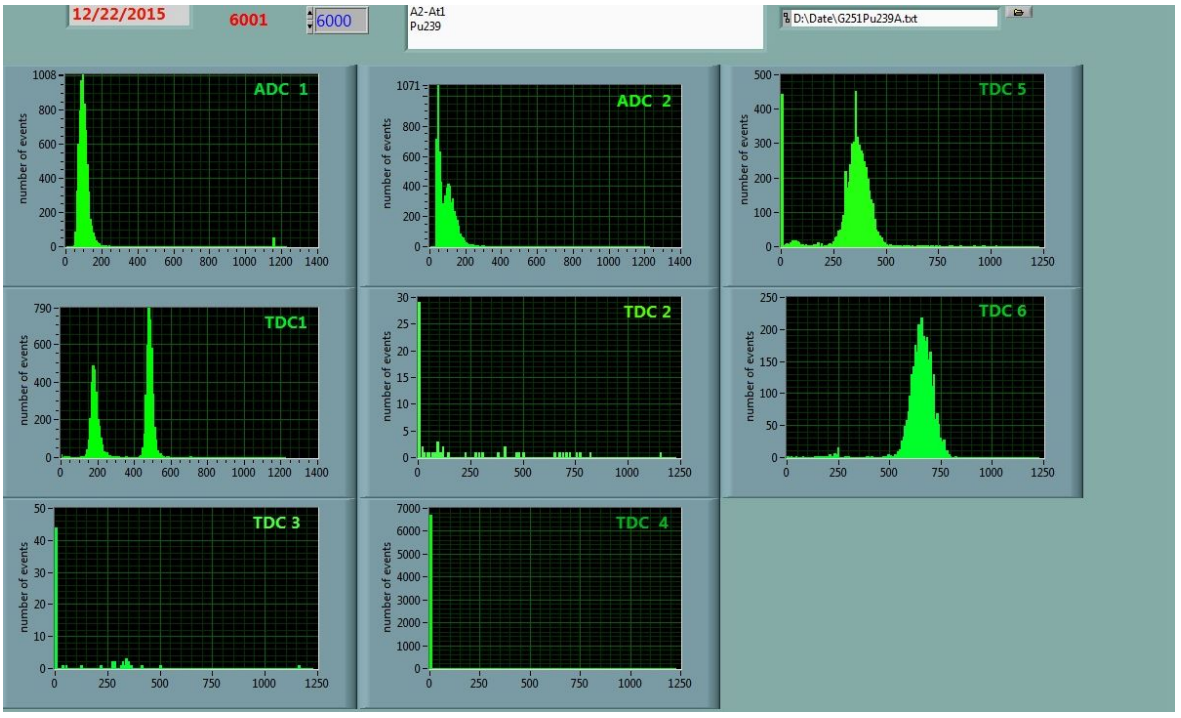

Fig. 26 The sample distribution of signals coming from ^{235}U radioactive source.

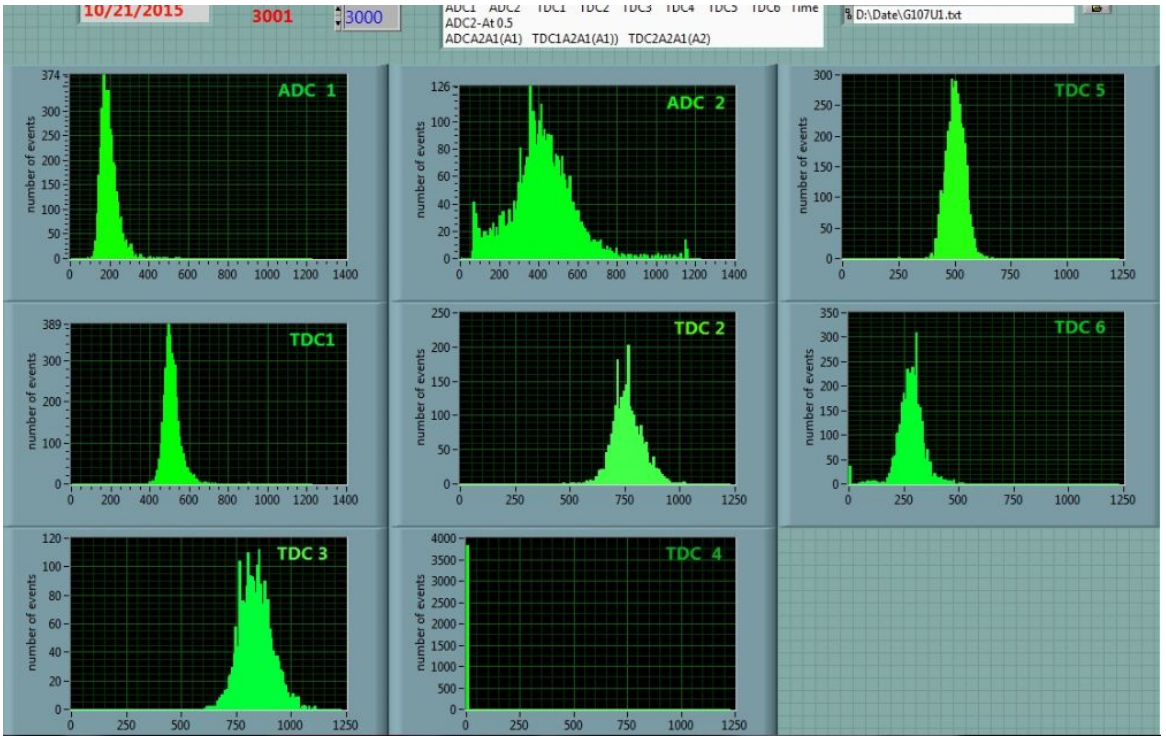

Fig 27 The sample distribution of signals coming from ^{239}Pu radioactive source.

Investigation of the timing and position measuring characteristics with an α-source

For the data analysis the ROOT (Brun and Rademakers 1997) package with C++ language and Python analytics tools have been used. In Fig. 28 the TOF distribution is shown. From this distribution, we can determine the time resolution of the MWPC units, which is equal to $638/2^{1/2} \approx 450$ ps.

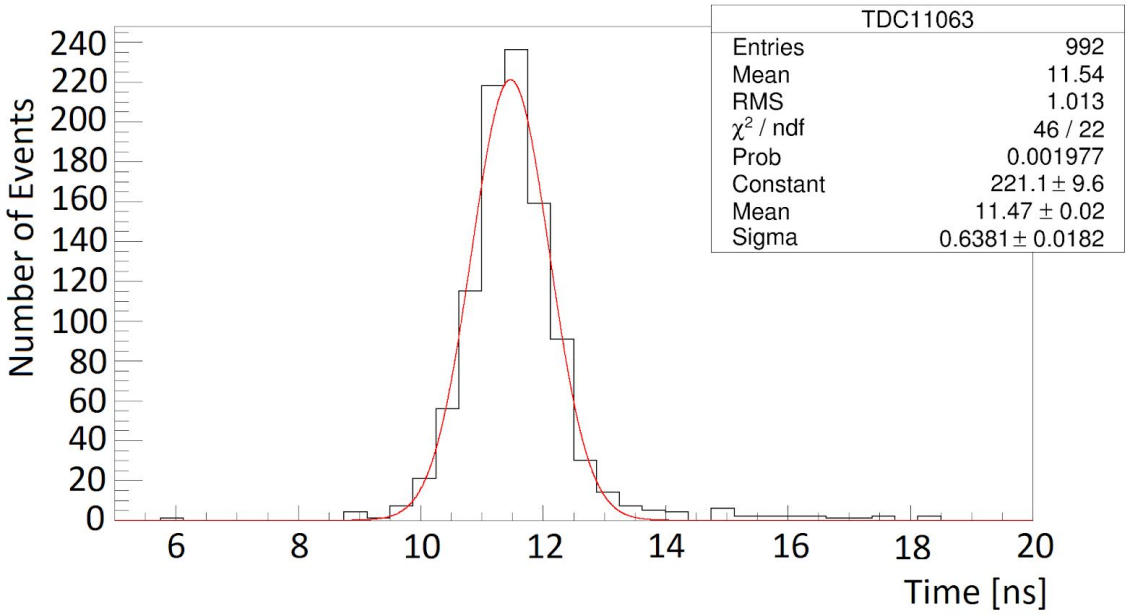

Fig. 28. Time difference between signals from the anode planes of MWPC1 and MWPC2.

In Fig. 29 the time-difference spectrum between the anode and one cathode plane of MWPC1 is presented. The sigma of this distribution is about 1 ns, which results in 1.5 mm position resolution.

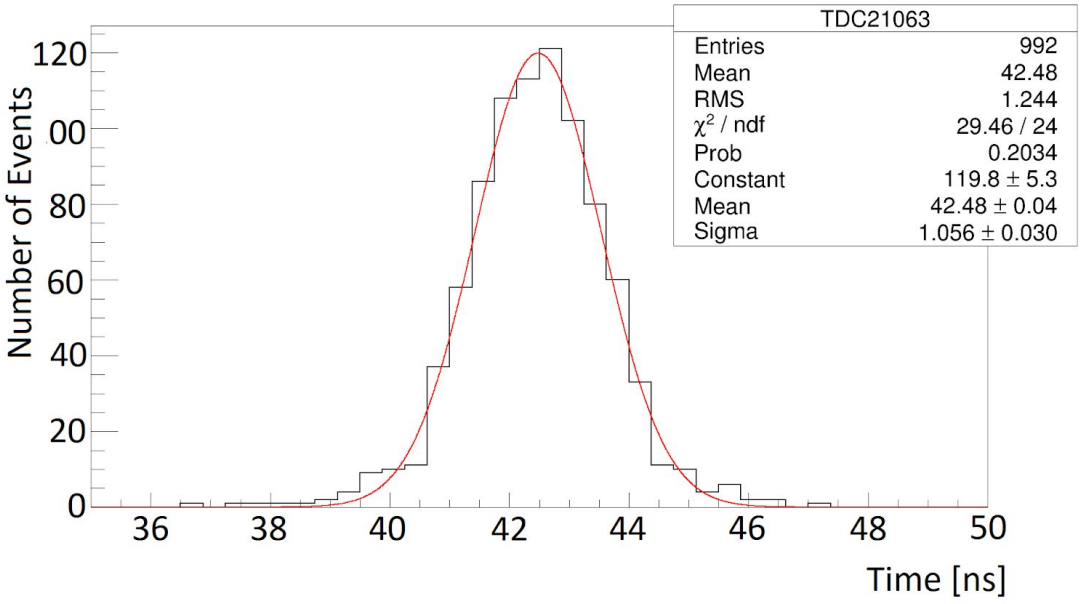

Fig. 29. Time difference between the anode and one cathode plane of MWPC1.

The typical measured spectrum of amplitudes of the MWPC1 anode signals, which are proportional to the ionization energy losses dE/dx of charged particles (Margaryan et al. 2010), is presented in Fig. 30.

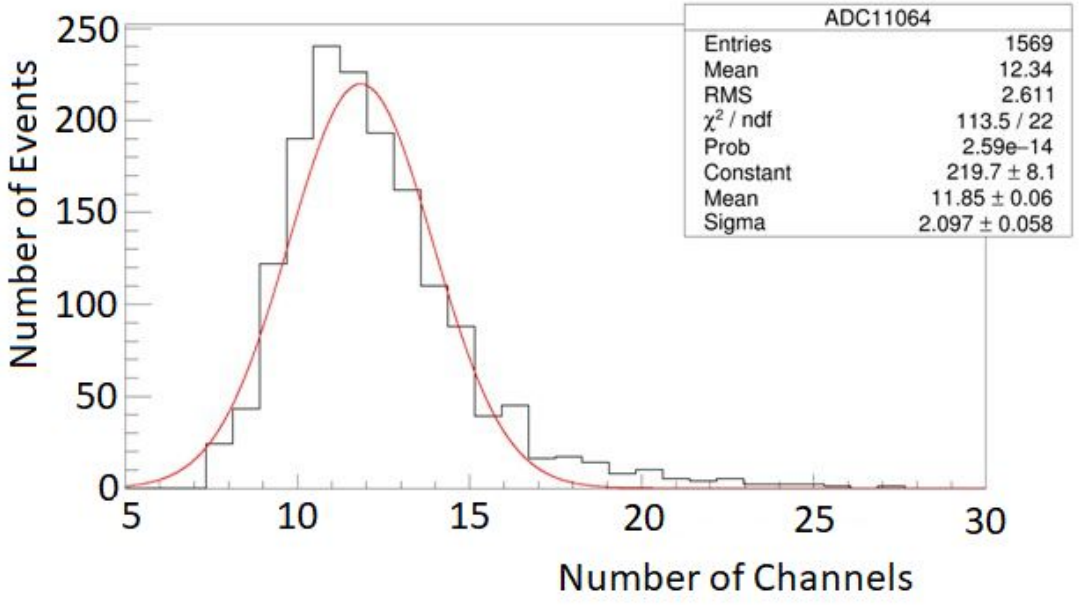

Fig. 30. Distribution of the amplitudes of MWPC1 anode signals.

The time resolution of the MWPC unit, as a function of methylal vapor pressure, is displayed in Fig. 31. It shows that a pressure range of 2-3 Torr is optimal for the best time resolution.

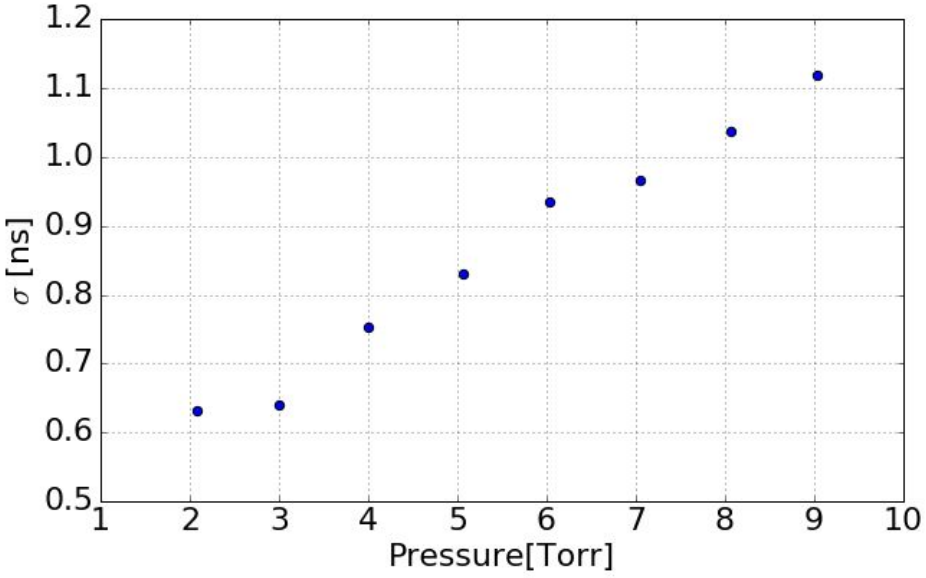

Fig. 31. Resolution of the time difference distribution between signals from the anode planes of MWPC1 and MWPC2 as a function of methylal vapor pressure.

Electron Beam Test

In this part we will present the Low-Pressure Multi Proportional Chambers (LPMWPC) and four types of amplifiers testing using bremsstrahlung photon beam from 20 MeV Electron beam. This is a proof of concept experiment that the MWPC modules can operate with gamma beam, producing high enough signals distinguishable from large background.

The test detector is schematically depicted in Fig. 32, and its general picture is shown in Fig. 33. It mainly consists of 2 MWPC chambers which are placed in a vacuum chamber. The spontaneous decay of alpha particles and fission fragments

were used. In Fig. 34 the typical signals of alpha particles, while in Fig. 35 the signals are of fission fragments are depicted using a digital scope.

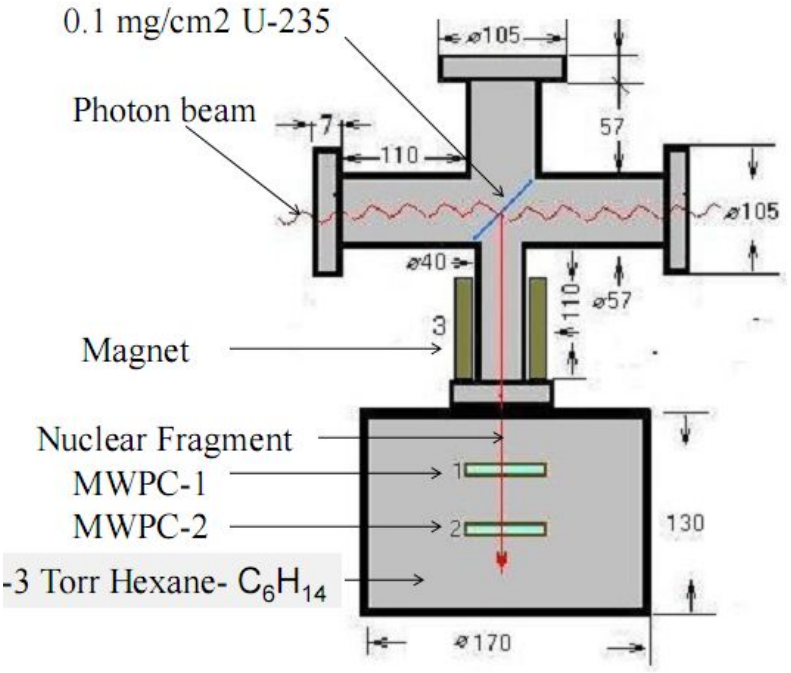

Fig 32. The schematic view of the detector.

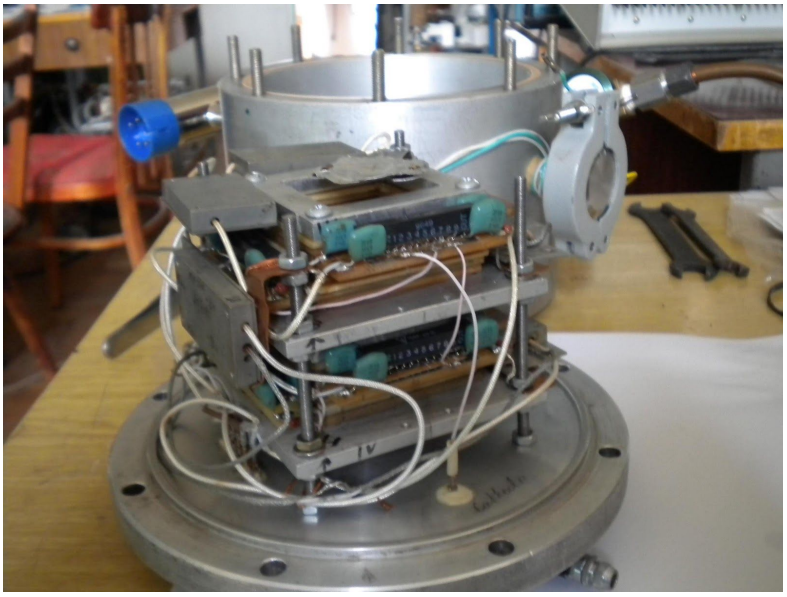

Fig. 33. The sample detector.

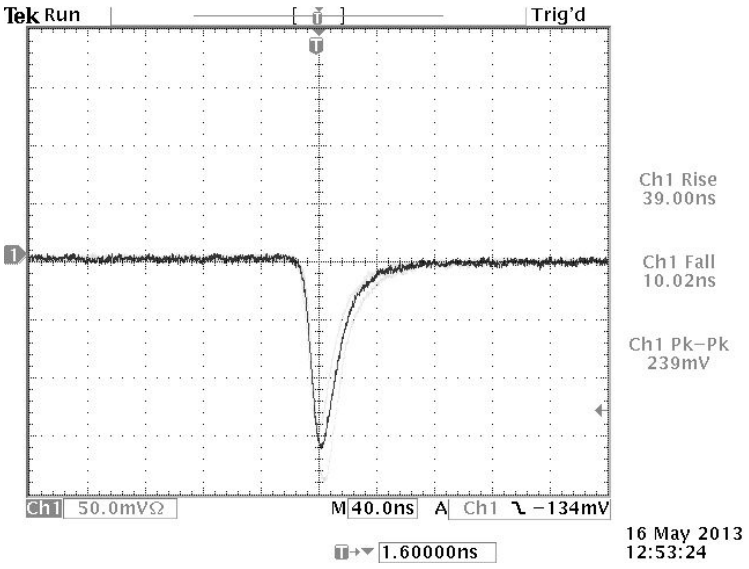

Fig. 34. The signal of alpha particles.

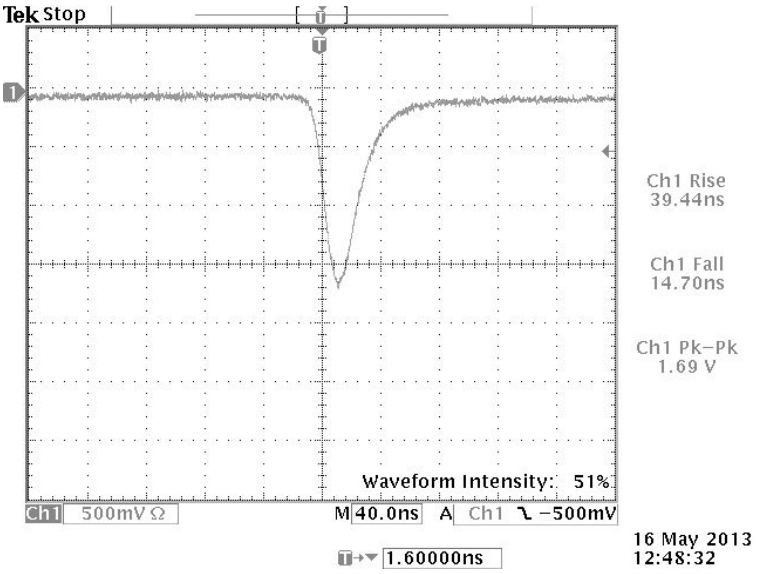

Fig. 35. The typical signal from fission fragments

An appropriate waveguide and connector were prepared to test the detector sample under the electron-photon beams of the injector at AANL. The detector is inserted into the ring at the end of the parallel electronic beam (Avakian et al. 2010), after the deviational magnet, Fig. 36. The deviational magnet(M3 in Fig. 36) was used to get a photon beam.

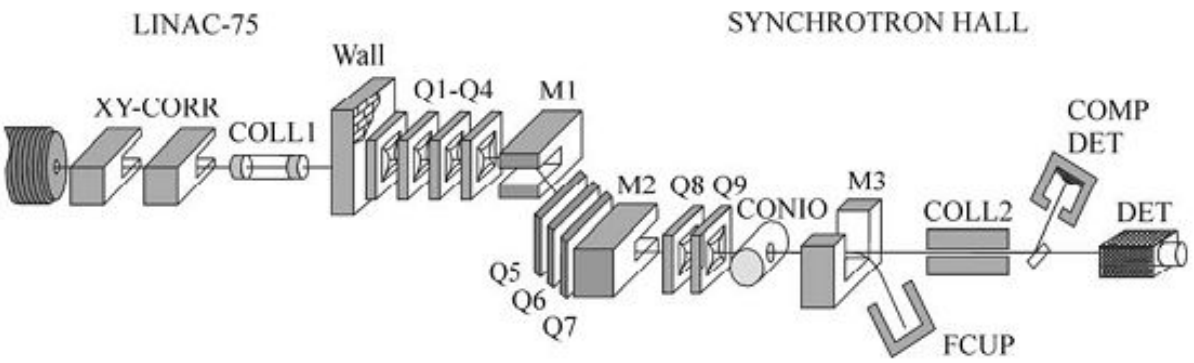

Fig. 36. The schematic view of the electron beam of the injector at AANL (Avakian et al. 2010).

During the operation of the injector klystron, about 20 mW noises were generated on the cables that come out of the ring, Fig. 37. These noises, however, do not amplify in the amplifier. On the other hand, the fission fragment signals are one order of magnitude greater than the noise, Fig. 38. Therefore, these noises will not cause problems in the fission experiments. These noises are the same level as the alpha particle signals. In this case, noise can be removed from the MWPC plate signals by further amplification and using appropriate thresholds. However, these noises can essentially affect the energy resolution of silicon detectors. Fortunately, these noises can be completely avoided by using new cables that come directly from the ring to the side ring.

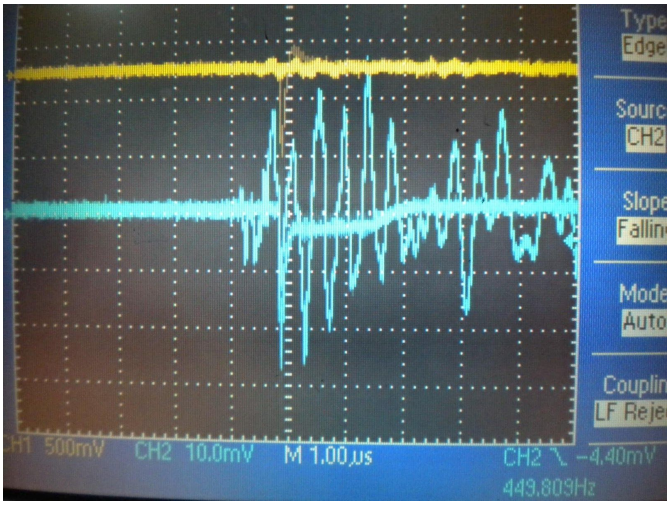

Fig. 37. The signals of the detector during photon beam operation.

The interaction of the 50 Hz, 1 msec, 40 nA electron beam with the radiator having 0.01 radiation length creates a photonic beam. The signals produced from the

nuclear fragments and alpha particles that are produced when the photon beam interacts with the hexane vapor molecules inside the detector are registered via digital scope are depicted in Fig. 38,39. The following two important conclusions can be drawn from this picture. First, the LPMWPC have over 1 MHz speed. Secondly, in the presence of all other conditions, they can work in about 10,000 times more intense photon beams, i.e. photon beams received from electron beams in an average of 400 μA. It opens up new possibilities for performing experiments of astrophysical interest in low energy domains, such as the study of the photodisintegration of the oxygen into an alpha particle and carbon nuclei reaction.

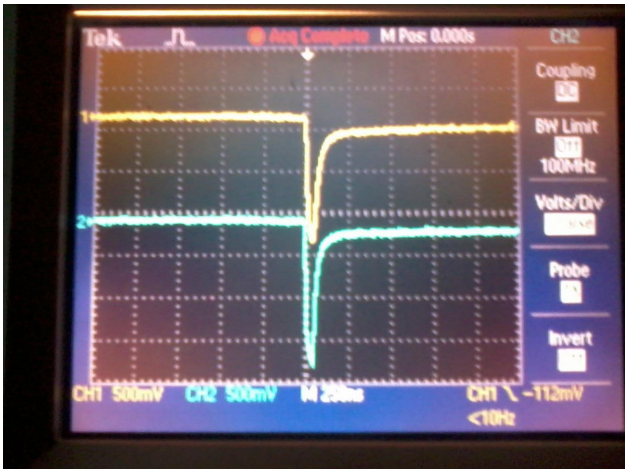

Fig. 38. The typical signals of fission fragments produced from the interaction of the photon beam and ^{235}U

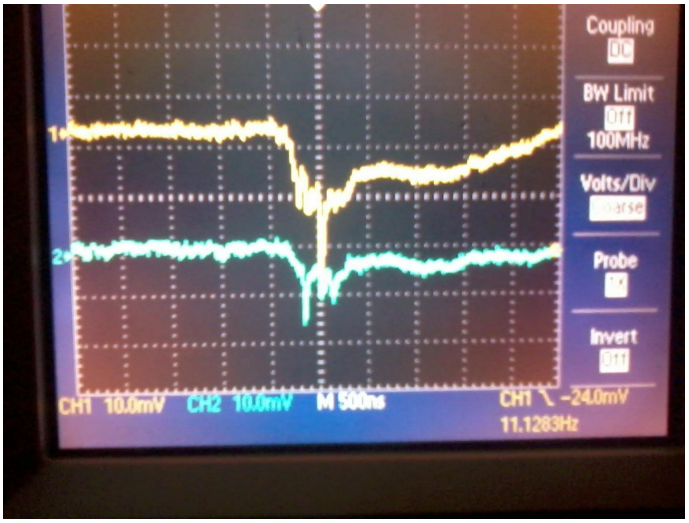

Fig. 39 The typical signals of alpha particles produced from the interaction of the photon beam with hexane vapor.

Chapter 3

Active target for $^{12}C(\alpha, \gamma)^{16}O$ reaction

Theory and recent studies

Light nuclei are expected to exhibit cluster-like properties in excited states with a low-density structure. Such states should exist particularly at excitation energies near the separation energies for these clusters, as depicted in the diagram by Ikeda et al. (Ikeda, Horiuchi, and Saito 1980). The Hoyle state, the 0_2^+ state at excitation energy (E_x) 7.654 MeV in ^{12}C, is considered archetypal of a state that exhibits α-particle structure, with a possible configuration being a 3-α gas-like structure similar to a Bose-Einstein condensate, consisting of three α particles all occupying the lowest 0S state (Schuck et al. 2013; Tohsaki, Horiuchi, Schuck, and Roepke 2017). This is schematically shown in Fig. 40. It is expected that equivalent Hoyle-like states should also exist in heavier α-conjugate nuclei such as ^{16}O and ^{20}Ne (Maruhn et al. 2006). Early discussions of extended structures in ^{16}O were instigated by the Chevallier et al. (Chevallier et al. 1967) who investigated low-energy α + ^{12}C scattering. A measurement of the $^{12}C(^4He,^8Be)^8Be$ excitation function indicated that a series of 2^+ to 6^+ resonances were populated in the E_x = 16–21 MeV energy range.

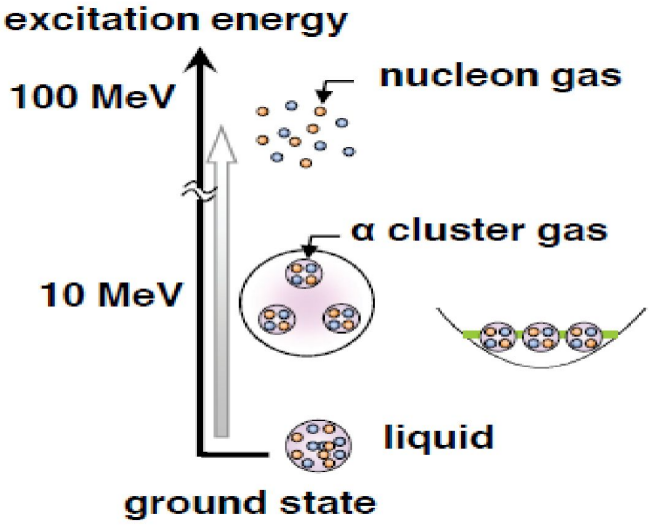

Fig. 40. Schematic of excitation energies of a cluster gas states and nucleon gas states for the case of ^{12}C (depicted from (Tohsaki, Horiuchi, Schuck, and Röpke 2017)).

The search for analogues of the Hoyle state in heavier α-conjugate nuclei is ongoing. Candidate states in ^{16}O below the four-α-particle breakup threshold ($S_{4\alpha}$ = 14.437 MeV) include the 0_4^+ state at Ex = 13.6 MeV, discovered in 2007 and observed via inelastic scattering at E_{lab} = 400 MeV (Wakasa et al. 2007). Another candidate is the 0_5^+ state at Ex = 14.032 MeV (Schuck et al. 2013). A potential Hoyle-like candidate above the four-α-particle breakup threshold in ^{16}O has been identified by Funaki et al. (Funaki et al. 2008), who solved a four-body equation of motion based on the Orthogonality Condition Model (OCM) that succeeded in reproducing the observed 0^+ spectrum in ^{16}O up to the 0_6^+ state. In Fig. 41 the comparison of the OMC prediction with the experimental spectrum is presented. The interpretation goes as follows: the first four excited 0^+ states have a α + ^{12}C structure where the α orbits in 0S, 0D, 1S configurations around the ground-state core of ^{12}C and a 0P wave orbital on the first 1^- state of ^{12}C. The α-particle condensed state is found slightly above the 4α threshold, as the 0_6^+ state. This 0_6^+ state is shown to have an analogous structure to the Hoyle state $^{12}C(0_2^+)$ and can be identified with the

experimental 0^+ state at 15.1 MeV. It is just hundreds of keV above threshold, and is strongly excited by inelastic electron scattering which means that the monopole transition is large. The 0_6^+ state obtained from the OCM calculation is 2 MeV above the four-α-particle breakup threshold and has a large radius of 5 fm, indicating a dilute density structure.

Ohkubo and Hirabayashi (Ohkubo and Hirabayashi 2010) showed that a rotational band with a developed α + ^{12}C(0_2^+) cluster structure, in which three α particles are locally condensed, is located near the four-α threshold. This was achieved by using a double folding potential which reproduces elastic and inelastic α-particle scattering from ^{12}C. The calculations suggest that the α-chain state should have the α + ^{12}C* [7.65 MeV, 0_2^+] structure, where the three α particles in the ^{12}C* [7.65 MeV, 0_2^+] Hoyle state are condensed.

The bandhead, suggested to be a superfluid of four α particles, is found to be the 0^+ state at 15.1 MeV. The moment of inertia of the 0^+ state at 15.1 MeV, just above the four-α threshold, is drastically reduced compared to the α + ^{12}C states.

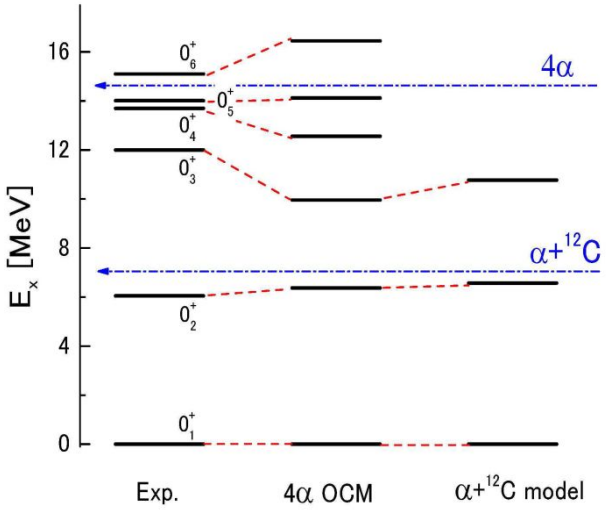

Fig. 41. Comparison of excitation energies from experiment and calculations made using the 4 α OCM, where the α+^{12}C and 4α thresholds are shown (depicted from (Funaki et al. 2008)).

The non-zero-spin α + Hoyle rotational states in ^{16}O, which are analogous to the Hoyle state, i.e. are members of the same family as the 0_6^+ state, was investigated. It was found that some states characteristically have large components of α + Hoyle state, where the α-particle orbits around the Hoyle state in S, P, D, F, and G waves for $J^\pi = 0^+, 1^-, 2^+, 3^-$, and 4^+, respectively ((Funaki et al. 2013) and references therein). In Fig. 42, we show the spectra as a function of J(J + 1). One can postulate that these form rotational bands with α + Hoyle-state structure, with $K^\pi = 0^+$ for the positive parity states and $K^\pi = 0^-$ for the negative parity states. There are probably many states in ^{16}O which can be interpreted as excited states out of the condensate and it is of great importance to study the cluster structures in the 15-21 MeV region in greater detail.

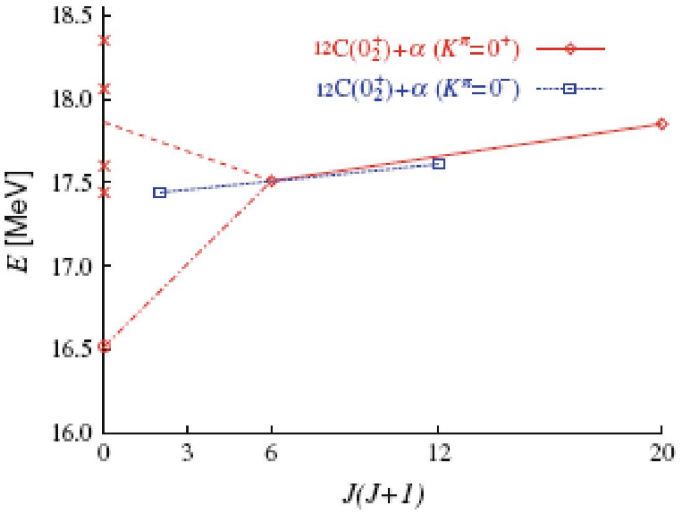

Fig. 42. Excitation energies of the rotational band of the α + Hoyle state. Dotted line is connected from the averaged excitation energy of the four 0^+ states over the 0_6^+ state at 16.5 MeV (depicted from (Funaki et al. 2013)).

One way of characterizing the cluster content is by measuring the charged-particle decays of populated states, which can provide valuable information

about the underlying structure of these states. The decay properties of the Hoyle-like state and the α+Hoyle-like rotational states were investigated by using the OCM model ((Funaki et al. 2013)and references therein). In Table I, the partial and total α-decay widths of the 0_6^+ state Γ_L decaying into the $\alpha+^{12}C(0_1^+)$, $\alpha+^{12}C(2_1^+)$ and $\alpha+^{12}C(0_2^+)$ channels are presented. The total α-decay width of 136 keV obtained is in good agreement with the corresponding experimental value of 166 keV (Tilley, Weller, and Cheves 1993).

Table I: Partial α decay widths of the 0_6^+ state according to the 4α OCM. The observed total width is 166 keV.

	$\alpha+^{12}C(0_1^+)$	$\alpha+^{12}C(2_1^+)$	$\alpha+^{12}C(0_2^+)$	Total
Γ_L (keV)	104	32	$8*10^{-7}$	136

Calculations performed with the Tohsaki-Horiuchi-Schuck-Ropke (THSR) α-cluster wave function (Funaki et al. 2010) results a total width of 34 keV for the 0_6^+ state (Funaki, Horiuchi, von Oertzen, Röpke, et al. 2009), much smaller than the OCM or experimentally observed values.

The decay widths are sensitive to details of the angular distributions of the decay products and are strongly dependent on the Coulomb barrier. This highlighted the need for an experiment that detects decay particles with high energy and angle resolution for reaction processes capable of preferentially populating 0^+ states or its rotational bands. A measurement of the $^{16}O(\alpha,\alpha')$ reaction at zero degrees, coupled with coincident observations of the ^{16}O decay products, was performed recently at the iThemba Laboratory for Accelerator-Based Sciences (iThemba LABS) in South Africa (Li et al. 2017). In contrast to transfer reaction measurements, inelastic α-particle scattering at zero degrees has the advantage that it predominantly excites low-spin natural parity states. The $^{16}O(\alpha,\alpha')$ reaction was studied at $\theta_{lab} = 0^\circ$ at an incident energy of $E_{lab} = 200$ MeV using the K600 magnetic spectrometer at iThemba

LABS. Proton decay and α-decay from the natural parity states were observed in a large-acceptance silicon strip detector array at backward angles. This array (Coincidence Array for K600 Experiments (CAKE) (Adsley et al. 2017)), consisted of four double-sided silicon strip detectors. The detection of coincident charged-particle decay with the CAKE array enables the characterization of resonances through the measurement of branching ratios and angular correlations of various decay modes. The associated decay channels of the ^{16}O nucleus, the α decay to the ground state of ^{12}C and proton decay to the ground state of ^{15}N are designated α_0 and p_0, respectively, while α decay to the first excited state $^{12}C(2_1^+)$ is designated α_1. By gating upon a particular decay channel and projecting onto excitation energy, the resonance line shape corresponding to a particular decay mode was observed in isolation. By fitting the K600 focal plane detector spectra for inclusive events and those gated on the α_0-, p_0-, and α_1-decay modes, the resonance energies and widths from the resonances at $E_x \approx 15$ MeV were extracted. These results are displayed in Table II.

Table II. Extracted single-channel *R*-matrix fit parameters from the inclusive and coincidence spectra at ~15 MeV.

J^π	Decay mode	E_R(MeV)	Γ_{total} (keV)	Branching ratio (%)
2^+	Inclusive	14.930	101	-
	p_0	14.929	40	21
0^+	Inclusive	15.076	162	-
	α_0	15.090	162	72
	α_1	15.046	216	67

In the inclusive spectrum, a prominent resonance was observed at E_x = 15.076 MeV with an associated width of 162 keV. This is in good agreement with previous measurements of the 0_6^+ resonance. In contrast, the observed width of 101 keV for the neighboring 2^+ resonance at E_R =14.926 MeV does not agree well with the corresponding literature value of 54 keV. The coincident charged-particle measurements were used to characterize the decay channels of the 0_6^+ state in ^{16}O located at E_x = 15.097 MeV. This state is identified by several theoretical cluster calculations to be a good candidate for the 4-α cluster state. The angular correlations observed in this experiment suggest the presence of a previously unidentified resonance at $E_x \approx 15$ MeV that does not exhibit a 0^+ character. The existence of a previously unresolved new resonance may explain the disparity between the theoretical and experimentally observed widths of 34 keV and 166 keV, respectively. A narrower and therefore longer-lived 0_6^+ resonance located above the 4-α-particle breakup threshold ($S_{4\alpha}$ = 14.437 MeV) could be considered a better candidate for a Hoyle-like state in ^{16}O.

The $^{13}C(\,^4He,4\alpha)n$ breakup reaction has been studied recently at beam energies of 27.0, 27.5, and 28.0 MeV (Curtis et al. 2016). A comparison with previous measurements of the $^{12}C(\,^4He,\,^8Be)^8Be$ excitation function and $^{12}C(\,^{16}O,4\alpha)^{12}C$ breakup channel suggests the $^8Be_{gs} + {}^8Be_{gs}$ decay of ^{16}O, observed from a possible 2^+ state at 17.3 ± 0.2 MeV, a 4^+ state at 18.0 ± 0.2 MeV, a 2^+ or 4^+ state at 19.4 ± 0.2 MeV, and a 4^+ or 6^+ state at 21.0 ± 0.2 MeV. More experimental studies are needed to confirm these findings.

We consider the application of the active ^{16}O target, based on the low-pressure MWPC technique and Si detectors, for study of the Hoyle like states in ^{16}O in the

15-20 MeV energy region, excited by means of proton and monochromatic, polarized photon beams.

Active ^{16}O target

The Hoyle like state in ^{16}O is expected at 15.1 MeV. The partial decay widths of such a state are shown in Table I, it decays mainly through the following two channels:

1) $^{16}O(15.1\ MeV) \rightarrow \alpha + {}^{12}C(0_1^+)$
2) $^{16}O(15.1\ MeV) \rightarrow \alpha + {}^{12}C(2_1^+) \rightarrow \alpha + {}^{12}C(0_1^+) + \gamma$

The neighboring 2^+ resonance has a decay channel $^{16}O(2^+) \rightarrow p + {}^{15}N(1/2^-)$. Detecting decay protons, α-particles, ^{12}C and ^{15}N nuclei from resonance states at Ex ≈ 15 MeV, produced by means of different type incident particles (proton, photon, etc.), requires a high resolution and large-acceptance experimental setup. This is crucial for identifying the Hoyle like state in ^{16}O and studying its structure. The resonance states in ^{16}O at Ex ~ 15 MeV cannot decay strongly into the 4α channel. There are, however, a number of resonances at 16-21 MeV energy range that decay to the $^{8}Be+^{8}Be$ or ^{12}C(Hoyle)+alpha final-states (Curtis et al. 2016). It is worthy to mention that even experimental study the decay of the 15.1 MeV state into two ^{8}Be's (i.e. into four low-energy α-particles) may be a very rewarding subject in order to elucidate further it's α cluster structure (Tohsaki, Horiuchi, Schuck, and Roepke 2017).

There are currently two experimental approaches under consideration for measurement of the inverse $^{16}O(\gamma, \alpha)^{12}C$ reaction, which is more accessible than the direct $^{12}C(\alpha, \gamma)^{16}O$ reaction. One is based on the bubble chamber technique and a bremsstrahlung photon beam (DiGiovine et al. 2015); the other employs an Optical Time Projection Chamber (O-TPC) (Gai et al. 2010) and a Laser Compton

Backscattered (LCB) γ-ray beam (Arutyunian and Tumanian 1963; Weller et al. 2009; Filipescu et al. 2015).

The reciprocity theorem of nuclear reactions relates the cross-sections of forward- and time-reversed nuclear processes. It relates the cross-section of an (α, γ) process to that of the time-reversed (γ, α) reaction:

$$\omega_A \frac{\sigma_A(\alpha,\gamma)}{\lambda_A^2} = \omega_B \frac{\sigma_A(\alpha,\gamma)}{\lambda_B^2} \quad (18)$$

where $\sigma_A(\alpha,\gamma)$, $\sigma_B(\gamma,\alpha)$ are the cross-sections of the direct $^{12}C(\alpha, \gamma)^{16}O$ and inverse $^{16}O(\gamma, \alpha)^{12}C$ reactions, $\lambda\!\!\!^{-}_A$ and $\lambda\!\!\!^{-}_B$ are the channel wavelengths for capture and photodisintegration, and ω_A and ω_B are the respective spin factors. In the energy region discussed here, i.e., Eγ = 8.0–8.5 MeV, the transformation factor provides a gain of ~50 in cross-section. Thus, at an equivalent center of mass energy of ~0.9 MeV, the direct (α, γ) cross-section is ~60 pb, while the inverse (γ, α) cross-section at ~8 MeV is 3 nb. The photodisintegration of ^{16}O at 8.0 MeV produces ^{4}He and ^{12}C with energies 675 and 225 keV, respectively, flying back-to-back, which aids the positive identification of this channel.

We present a new active target for measuring the cross-section of the ^{16}O (γ, α)^{12}C reaction, using an LCB γ-ray beam of energy Eγ = 8–10 MeV. It is a position- and time-sensitive detector system based on low-pressure Multi Wire Proportional Chamber (MWPC) technology. This enables the trajectories and velocities of 4He and 12C fragments of a few hundred keV energy to be determined.

Methods

The new method is based on two technologies: (1) an active target based on low-pressure MWPC, and (2) a gamma-ray beam from backscattering of laser photons from several hundred MeV electrons. The latter produces an intense monochromatic gamma-ray beam with small angular divergence ($<2 \times 10^{-4}$ rad)

(Filipescu et al. 2015). Methylal ((OCH3)2CH2) and hexane (C6H14), at a pressure of a few Torr, serve as the filling gases for operation of the MWPC. Operation with hexane is intended for evaluation of the background from carbon nuclei in methylal. The proposed active-target system employs a gas pressure of 3–9 Torr to detect low-energy nuclear fragments and determine their trajectories and velocities. The low pressure renders it very insensitive to minimum ionizing particles and γ-rays, but the disadvantage of this is low luminosity due to the small density of target atoms. Laser backscattering delivers a highly-directed, pencil-like photon beam so that this drawback can be mitigated by using a multimodular active-target system with sufficient total length to provide the necessary luminosity for the experiment. For example, at ELI-NP, the angular divergence of the LCB γ-ray beam is expected to be less than 0.2×10^{-4} rad, which means that over a 10 m distance the transverse size of the beam will increase by only 2 mm. Therefore, the active-target system could, in principle, consist of a stack of some hundreds of modules with a total length equal to 10 m.

A schematic drawing of the prototype, active-target module is shown in Fig 43. It consists of four low-pressure chamber units (1, 2, 3 and 4), which form two symmetric arms. The MWPC units are windowless in order to present the minimum amount of material to the incident, low-energy nuclear fragments. The geometrical acceptance of the active target depends on the L1, L2 and L3 dimensions, where the optimal sizes will be determined in future Monte Carlo and experimental studies. In the present study, we used prototype MWPC units with an active area of 30 × 30 mm2.

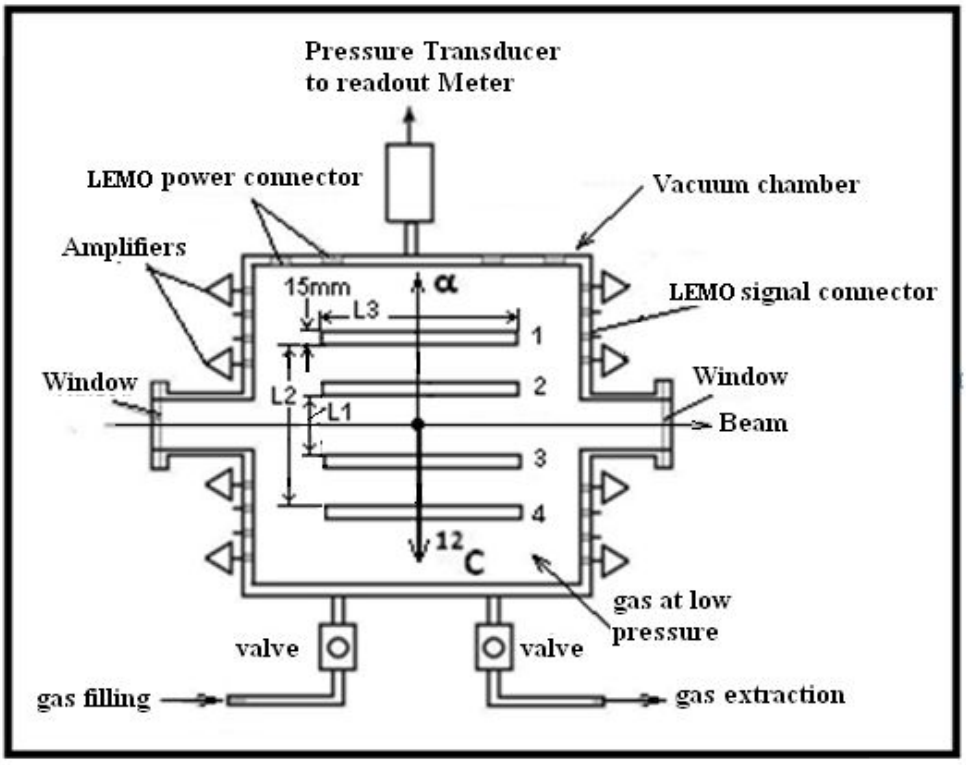

Fig. 43. Schematic of the active target: Multi Wire Proportional Chamber (MWPC) units 1, 2, 3, 4.

The methylal gas serves as an ionization medium for MWPC operation, and in addition the oxygen atoms of the methylal molecules serve as an experimental ^{16}O target. The number of oxygen atoms in the target can be calculated by $N_O = N_A*\rho*p*L*n/A$, were L is the target thickness, n is the number of oxygen atoms per $C_3O_2H_8$ molecule (n = 2), ρ is the density of the methylal gas at 20° C (ρ = 0.0042 mg/Torr/cm^3), p is the vapor pressure in Torr, N_A is Avogadro's number, and A is the molecular weight of $C_3O_2H_8$ in a.m.u. (A =76). For L = 3 cm and p = 3 Torr, we have $N_O = 6*10^{17}$ atoms/cm^2.

Using a multi module active-target system consisting of some hundreds of modules, the number of oxygen atoms can be increased by over two orders of magnitude. This is presented schematically in Fig 44. Assuming that the number of oxygen atoms seen by the beam is 3×10^{20} atoms/cm^2, the detection efficiency for the

$^{16}O(\gamma, \alpha)^{12}C$ reaction (geometrical acceptance included) is 30%, the γ-ray intensity is 5×10^9 photons/s (Filipescu et al. 2015), and the cross-section of the $^{16}O(\gamma, \alpha)^{12}C$ reaction is 3 nb, then the $^{16}O(\gamma, \alpha)^{12}C$ reaction rate is equal to $3 \times 1020 \times 5 \times 109 \times 0.3 \times 3 \times 10^{-33} = 0.00135$ event/s.

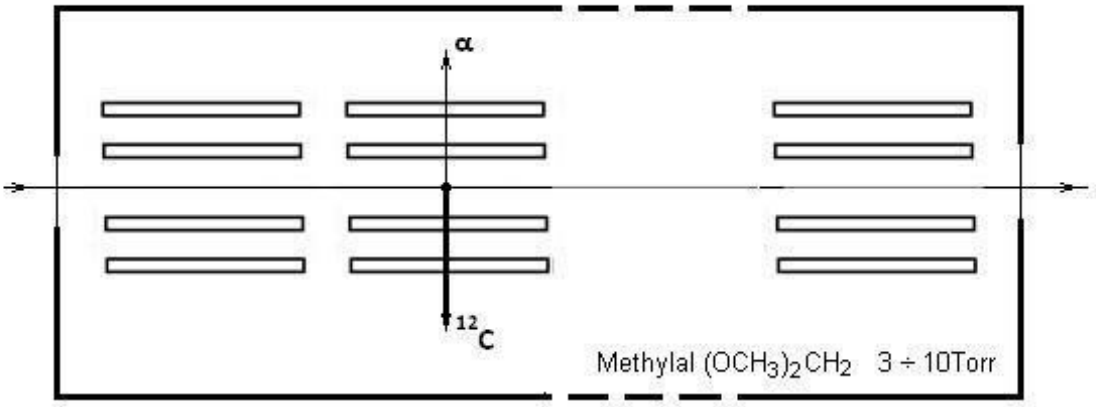

Fig. 44. Schematic of the multi module active target.

Timing information is an important consideration when using the active target. Firstly, the real coincidence between modules and beam bunches must be separable event-by-event. At ELI-NP, the separation between photon beam bunches is 16 ns, so the timing resolution of ~1 ns is necessary for separating the events from different bunches. Secondly, the time-of-flight between the low-pressure MWPC units can be used to determine the velocity of the produced alpha particles and ^{12}C nuclei, thus providing an additional criterion to separate real $^{16}O(\gamma, \alpha)^{12}C$ events from the background. Good position resolution is needed to identify back-to-back fragments and to separate these from the huge amount of electromagnetic background (the electron-positron pair production cross-section in this energy region is about 100 mb, i.e., 10^8 times larger than the photodisintegration cross-section of ^{16}O).

Simulations to justify the experiment

To be detected, low-energy decay particles require enough energy to pass through the module, i.e., they are required to have a range of at least 5.5 cm to generate signals in both MWPC units. In Fig 45, the electronic stopping powers (ionization energy losses) for He and C ions in methylal, simulated by means of the SRIM (ZIEGLER and F n.d.) software package, are displayed. The corresponding ranges of He and C ions in methylal, derived from the SRIM stopping powers, are presented in Fig 46. From Figs 45 and 46, it can be seen that an active-target detector system filled to 3 torr methylal is capable of detecting alpha particles with energies above 50 keV and ^{12}C nuclei with energies higher than 100 keV. This is crucial for the detailed study of the photodisintegration of ^{16}O at energies $E\gamma$ = 8.0–8.5 MeV, where the α-particles have energies of ~0.6 MeV and the ^{12}C nuclei have energies of ~0.2 MeV. The respective α-particle and ^{12}C ranges in methylal at 3 torr pressure are 0.3 mg/cm^2 (24 cm) and 0.1 mg/cm^2 (8 cm).

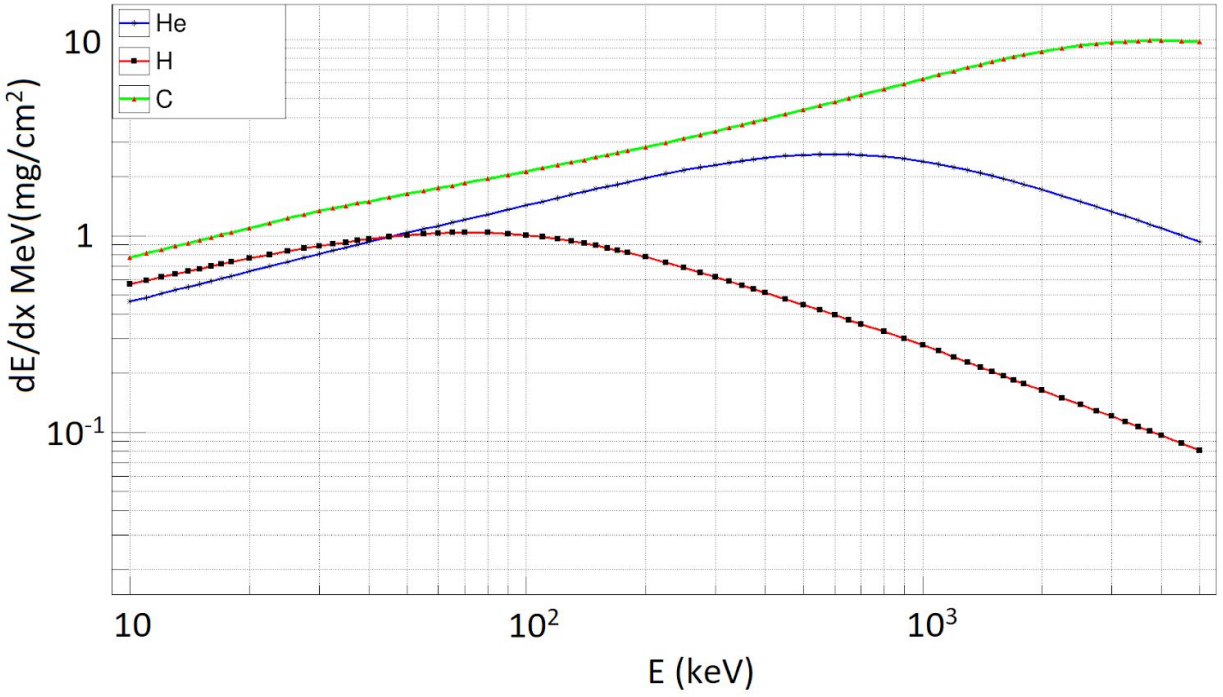

Fig. 45. The electronic stopping power of H, He and C ions in methylal.

In Fig. 46 the corresponding ranges of H, He and C ions in methylal simulated by formulae, using SRIM electronic stopping powers are presented.

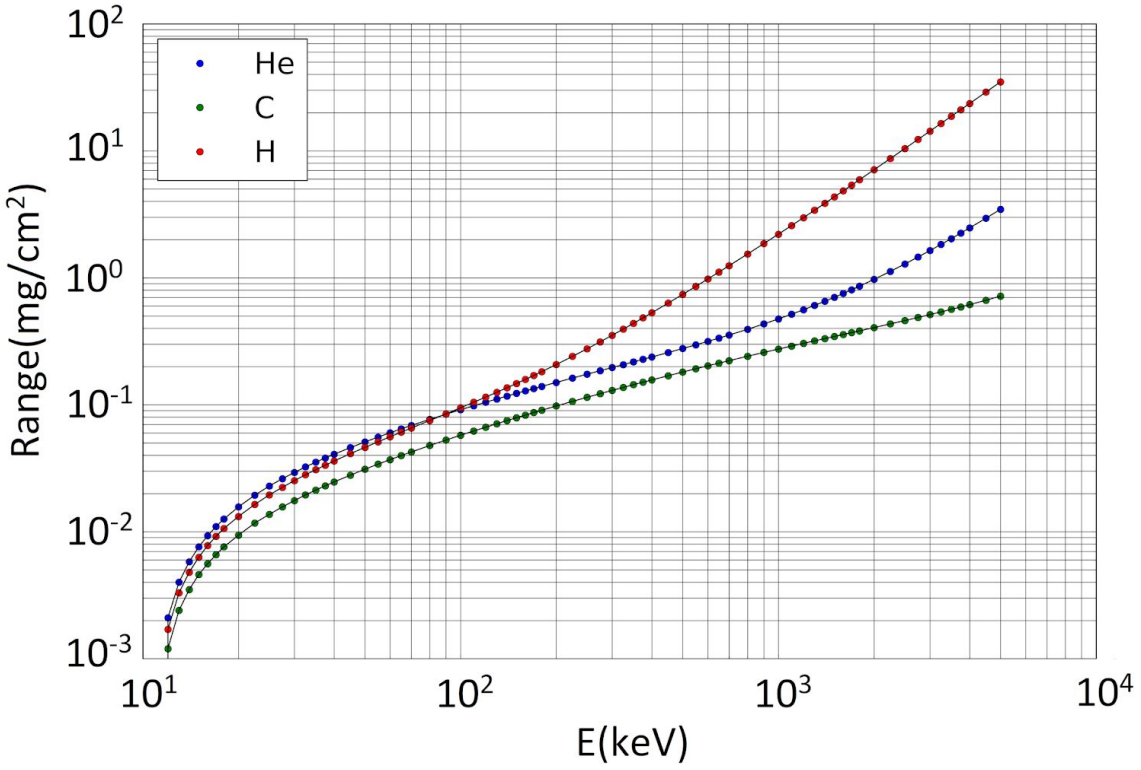

Fig. 46. The ranges of H, He, C ions in methylal vs energy.

Timing information is an important consideration when using the active target. First of all, the real coincidences between modules must be separable event-by-event. The active target is planned for use at the proton beam of the Yerevan cyclotron and at the laser Compton backscattered photon beams of ELI-NP, where the separation between particles bunches is 25 ns and 16 ns, respectively. Timing resolution of the order of 1 ns is necessary for separating of events from different bunches. Correlating the time-of-flight between low-pressure MWPC units and energy deposit in the SSD helps to select different decay channels. Excitation energy vs silicon energy (corrected for energy loss in the gas) can be constructed, showing how different excited states decay. Meanwhile, the time-of-flight between low-pressure MWPC

units can be used to determine the energies of slowing down decaying species such as 50-500 keV protons, alpha particles, and ^{12}C nuclei with energies higher than 100 keV, were Si detectors can't be used.

The windowless MWPC units will be located as close as possible to the incident beams to maximise geometrical acceptance and to minimize energy loss effects in the gas environment. It is expected that many background particles, e.g. due to elastic proton-proton scattering, will be produced. Therefore the rate capability of the MWPC units is a crucial factor. Typical signals from the anode plane of the MWPC1, placed next to ^{239}Pu source without any collimator, are displayed over a time scale of around 12 μs in Fig. 47. From this we infer that the MWPC has the capability to operate properly at rates up to few MHz.

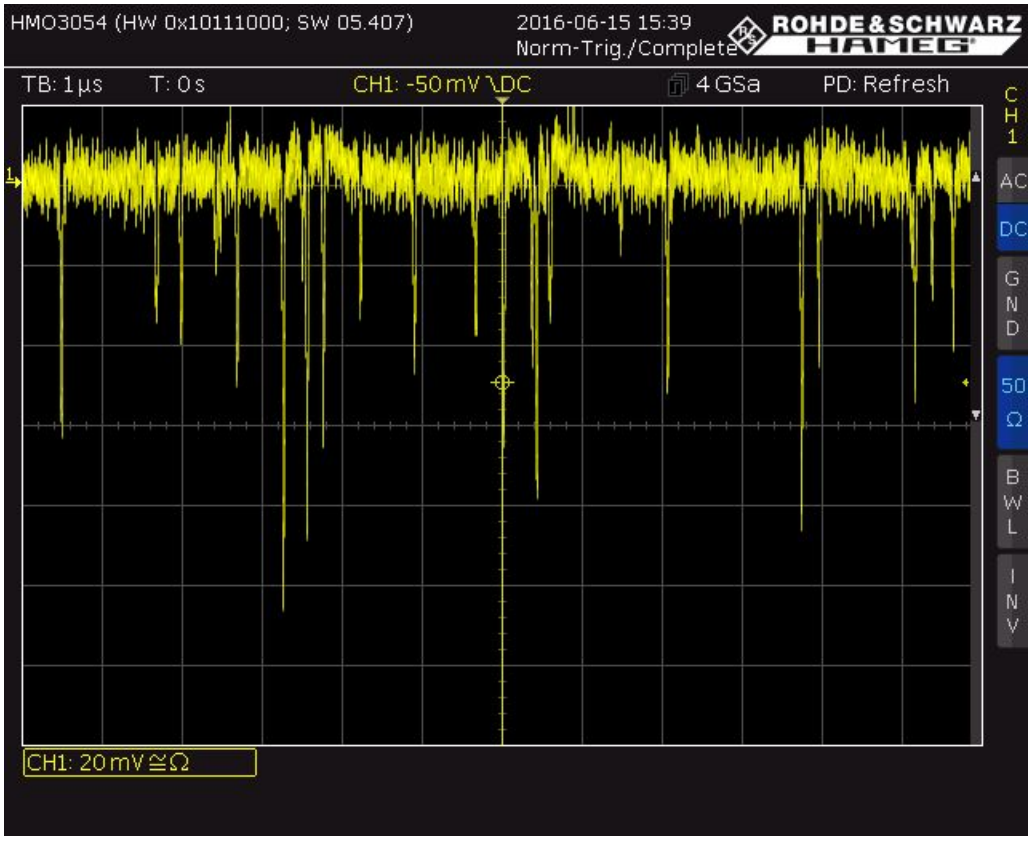

Fig. 47: Typical signals from the anode plane of MWPC1, displayed on a 500 MHz oscilloscope. The alpha source is ^{239}Pu, with no collimation applied. MWPC

conditions are: hexane 2.85 Torr, +300 V on the anode, 0 V on the cathodes and -300 V on the guard planes.

Given that huge numbers of electron-positron pairs will be produced, the sensitivity of the low-pressure MWPC to minimum ionizing particles was measured by replacing the ^{239}Pu α-particle source with a β-particle source (^{90}Sr). The rejection factor for a single MWPC unit, i.e., the ratio of β-particle to α-particle detection efficiencies is about 10^{-4}. Since the ^{16}O photodisintegration event will be detected in four (1, 2, 3 and 4) MWPC units, the overall β-particle to α-particle detection efficiency will reduce to 10^{-16}. However, this rejection factor will be checked in dedicated experimental studies.

The energy resolution of α-particles and ^{12}C nuclei depends on the L1, L2 and L3 dimensions (see Fig 43) and is expected to be in the range of 10–20%. The time resolution for α-particles with energies lying in the range 0.1–5.0 MeV will be ~0.45 ns and a flight time of ~10 ns. This will result in better than 10% energy resolution. In comparison, the bubble chamber experiment (DiGiovine et al. 2015) provides no kinematic information, while the O-TPC experiment (Gai et al. 2010) provides only energy information but with a resolution several times better than the present proposed technique. However, in the present case, both angle and energy information will be recorded. Selection of back-to-back ^{16}O(γ, α)^{12}C reaction products will be used to reject background photodisintegration events from ^{12}C and ^{16}O nuclei, initiated by high-energy bremsstrahlung photons. This selection will also suppress any residual pair-production events. The separation of signal from background will be studied in realistic experimental conditions in future test experiments.

Exploratory experiments at HIγS

We propose to carry out an exploratory experiment at HiγS starting with a check on the in-beam background conditions for the $^{16}O(\gamma,\alpha)^{12}C$ reaction at photon energy around 8 MeV, where the reaction cross section is very small. This will be followed by a measurement of this reaction cross section at photon energy around 9.5 MeV, where the cross section is ~10^4 larger and then a measurement of the $^{12}C(\gamma, 3\alpha)$ reaction cross section in the energy region 9.5-15.5 MeV. These exploratory measurements will be carried out using an experimental setup based on the prototype chamber (Fig. 48), which is similar to that displayed in Fig. 43, but with a converter (C) and target (T) added. The converter will be used to produce electron-positron pairs, mimicking the type of background conditions which are expected for the real experiment. The target will be a 1 μm thick Mylar (Polyethylene terephthalate: $(C_{10}H_8O_4)_n$) or Polyethylene $(C_2H_4)_n$ film angled at ~20 deg, with respect to the beam direction, which increases the effective thickness presented to the beam by a factor ~3.

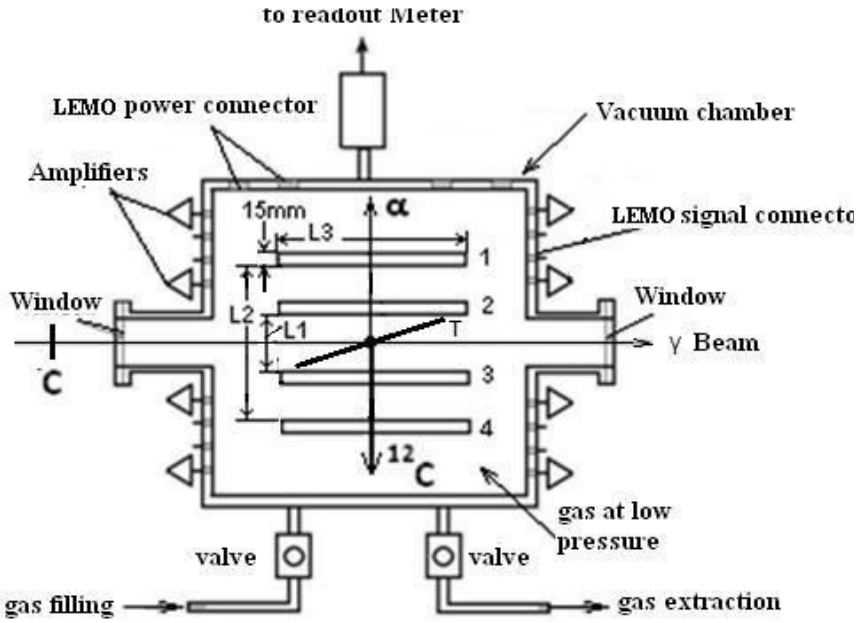

Fig. 48. Schematic of the experimental setup for exploratory experiments. C-converter, T-target, other notations as in Fig.43.

Study of background conditions at 8 MeV

The first measurement will study background conditions at photon energy around 8 MeV. Angular distributions, total cross-sections and, E1 and E2 transition cross sections of the $^{16}O(\gamma,\alpha)^{12}C$ reaction, induced by polarized photons have been calculated at low nuclear astrophysics energies using resonance theory (Xu et al. 2007). Polarized differential cross-sections of $^{16}O(\gamma,\alpha)^{12}C$ are shown in Fig. 49. The polar scattering angle Θ and the azimuthal angle ϕ with respect to the photon polarization orientation are illustrated in Fig. 50. From Fig. 49 we can see the differential cross-sections for a given polar angle has a maximum value at $\phi = 0$, when the photon polarization orientation vector is located in the reaction plane, which is defined by the orientation of the incident photon beam and the outgoing alpha particle. Furthermore the differential cross-section is equal to zero as $\phi = \pi/2$, where the photon polarization orientation is perpendicular to the reaction plane. Therefore,

the experimental yield is largely confined to the plane around $\phi = 0$. This prediction will be used to arrange a measurement of the differential cross-sections of $^{16}O(\gamma,\alpha)^{12}C$ reaction.

The number of oxygen atoms in the Mylar target is given by $N_O = N_A \times \rho \times p \times L \times n/A$, were L is the target thickness, n is the number of oxygen atoms per $C_{10}H_8O_4$ molecule (n = 4), ρ is the density of the Mylar ($\rho = 1.38 g/cm^3$), N_A is Avogadro's number, and A is the molecular weight of $C_{10}H_8O_4$ in a.m.u. (A = 192). For L = 3 μm effective thickness, $N_O = 5.2\times10^{18}$ and $N_C = 2.5\times5.2\times10^{18} = 1.3\times10^{19}$. In addition we have 1.2×10^{18} oxygen and 1.8×10^{18} carbon atoms from the 6 Torr and 3 cm of Methylal gas of the MWPC. In total from the Methylal and tilted Mylar we have 6.4×10^{18} oxygen and 1.48×10^{19} carbon atoms. The photon flux at HIγS in the energy region 8 - 10 MeV is 2.4×10^8 photon/s or about 10^{12} photon/h. The $^{16}O(\gamma,\alpha)^{12}C$ reaction cross-sections at the 8 MeV ($E_{c:m} \sim 1$ MeV) and 9.5 MeV ($E_{c:m} \sim 2.2$ MeV) are approximately 3 nb and 10000 nb respectively (see Fig. 51). Assuming 50% detection efficiency we will have rates of 10^{-2}/h and 32/h respectively for 8 MeV and 9.5 MeV photons. We will select the converter to produce electron-positron pair rates 100 times higher than those expected in real experimental conditions. The goal of this measurement is to demonstrate that the experimental setup is insensitive to the expected electromagnetic background.

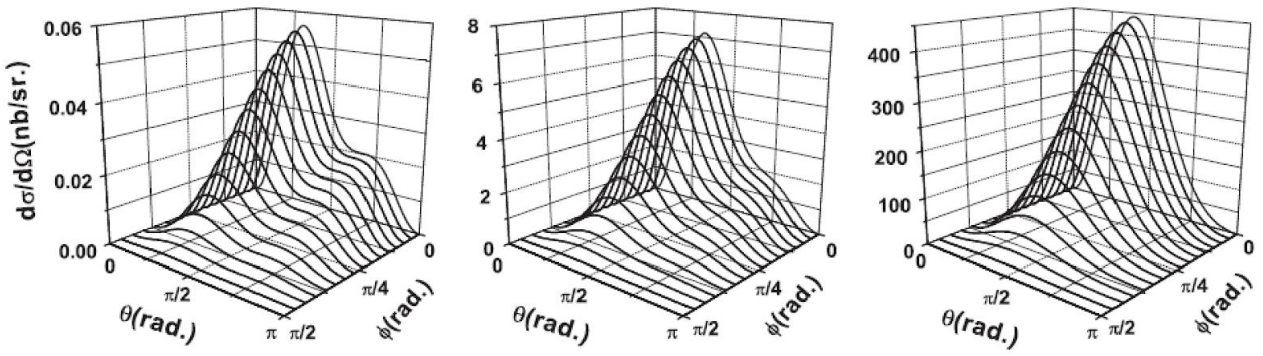

Fig. 49. The differential cross-sections of $^{16}O(\gamma,\alpha)^{12}C$ at $E_{c:m}$ = 0.8MeV (left panel), $E_{c:m}$ = 1.4MeV (middle panel) and $E_{c:m}$ = 2.2MeV (right panel) (taken from (Xu et al. 2007)).

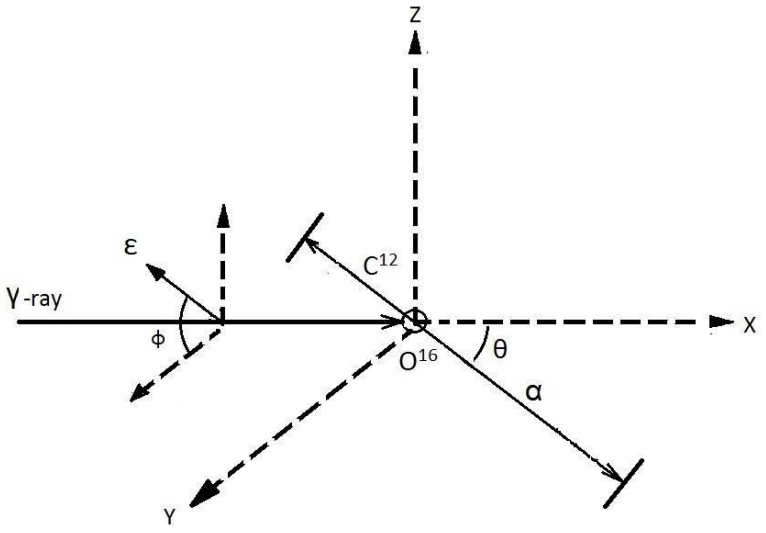

Fig. 50. The sketch of the reaction of $^{16}O(\gamma,\alpha)^{12}C$ and experimental setup (see (Xu et al. 2007) for details.

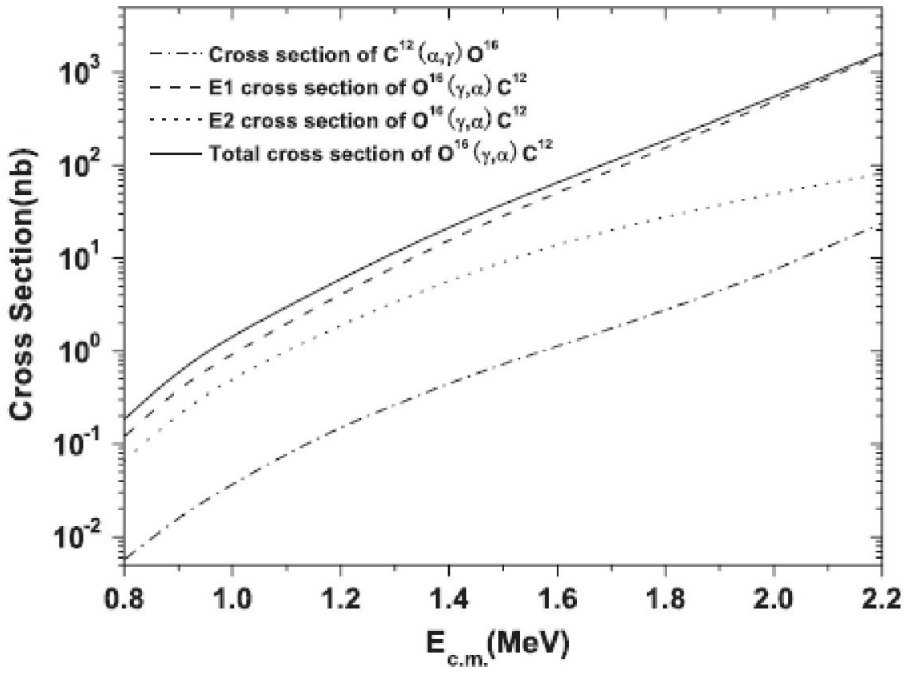

Fig. 51. The E1(dash line), E2(dot line), and total (solid line) cross-sections of $^{16}O(\gamma,\alpha)^{12}C$. The cross-section of $^{12}C(\alpha, \gamma)^{16}O$ ^{12}C (dash-dot line) is also shown for comparison (see (Xu et al. 2007) for details).

Test experiments

We propose to carry out two more exploratory measurements as a proof of principle of the technique. In the first of these we propose to take data with a 9.5 MeV energy photon beam. The cross sections of the $^{16}O(\gamma,\alpha)^{12}C$ and $^{12}C(\gamma, 3\alpha)$ reactions at 9.5 MeV are 10 μb and 6 μb (see below) and consequently the expected rates of these reactions are 32/h and 45/h. The recorded time and track information from the ^{12}C and ^{16}O dissociation events will be used for separation of these reactions.

In addition the second of these we propose to measure ^{12}C photodisintegration in the energy range 9.5- 15.5 MeV, by using 6 Torr hexane (C_6H_{14}) as a working

MWPC gas and a ~20° tilted 1μm thick Polyethylene (C_2H_4) film as a target. In total from 3 cm hexane and 3μm effective thickness of Polyethylene film, we have 1.56×10^{19} carbon atoms. The $^{12}C(\gamma, \alpha)\ ^{8}Be$ reaction is interesting in connection with 3α reaction, which plays a crucial role in stellar helium burning (Fowler 1984; Weaver and Woosley 1993). The photodisintegration of carbon into three α-particles was investigated in the past mainly by using the photo-emulsion technique (Goward and Wilkins 1953; V. N. Maikov 1958; Murakami 1970; Kotikov et 2002). The cross-section for the photodisintegration of $^{12}C(\gamma,3\alpha)$ has been determined for γ-ray energies up to about 70 MeV from a study of 2500 stars in nuclear emulsions (Xu et al. 2007). The cross-section exhibits at least five resonances, situated at γ-ray energies Eγ = 17.3, 18.3, 21.9, 24.3 and 29.4 MeV (see Fig. 52 and Fig. 53 depicted from (Xu et al. 2007)). The integrated cross-section is 1.21 ± 0.16 MeV mb for Eγ<20.5 MeV, a further 2.8 ± 0.4 MeV mb for 20.5≤Eγ<42 MeV, and less than 0.2 MeV mb for 42≤Eγ<60 MeV.

The energy-release E_T (= ΣE_r, E_r are the particle energies, r = 1, 2 and 3) are illustrated in Fig. 54, which combines the data from 33 and 70 MeV bremsstrahlung beams (see (Goward and Wilkins 1953) for details). The experimental E_γ (E_T) resolution, FWHM, is ≤1 MeV.

The data obtained in the experiments (Goward and Wilkins 1953; V. N. Maikov 1958; Murakami 1970; Kotikov et 2002). are, however, quite sparse and contradictory as shown in Fig. 55.

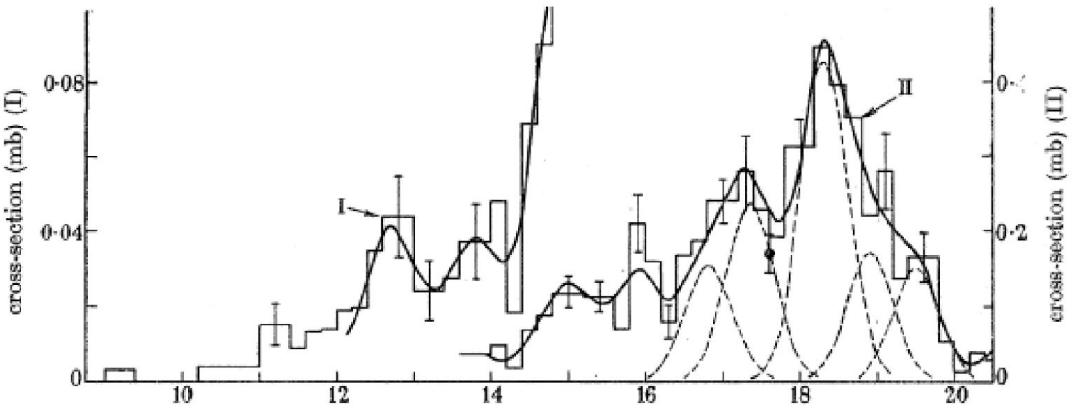

Fig. 52. $^{12}C(\gamma,3\alpha)$ cross-sections for γ-ray energies less than 20.5 MeV.

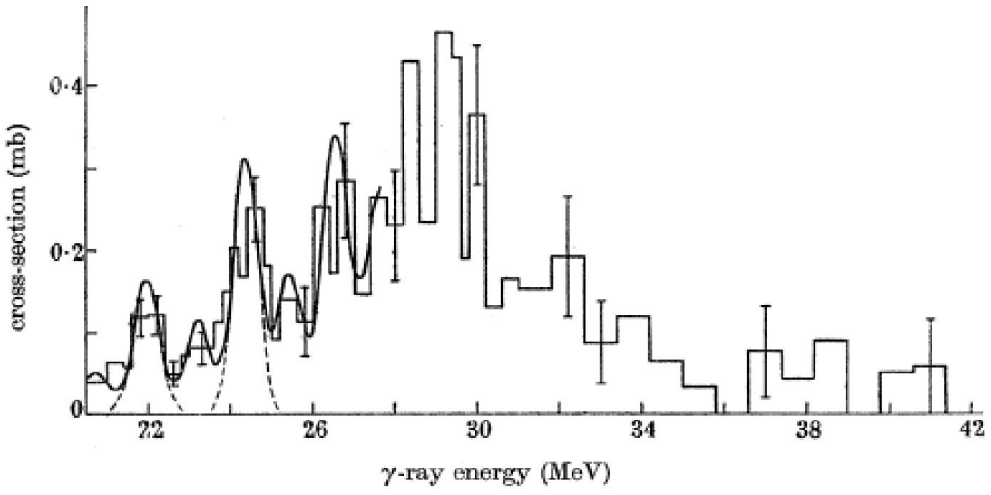

Fig. 53. $^{12}C(\gamma,3\alpha)$ cross-sections for γ-ray energies above 20.5 MeV.

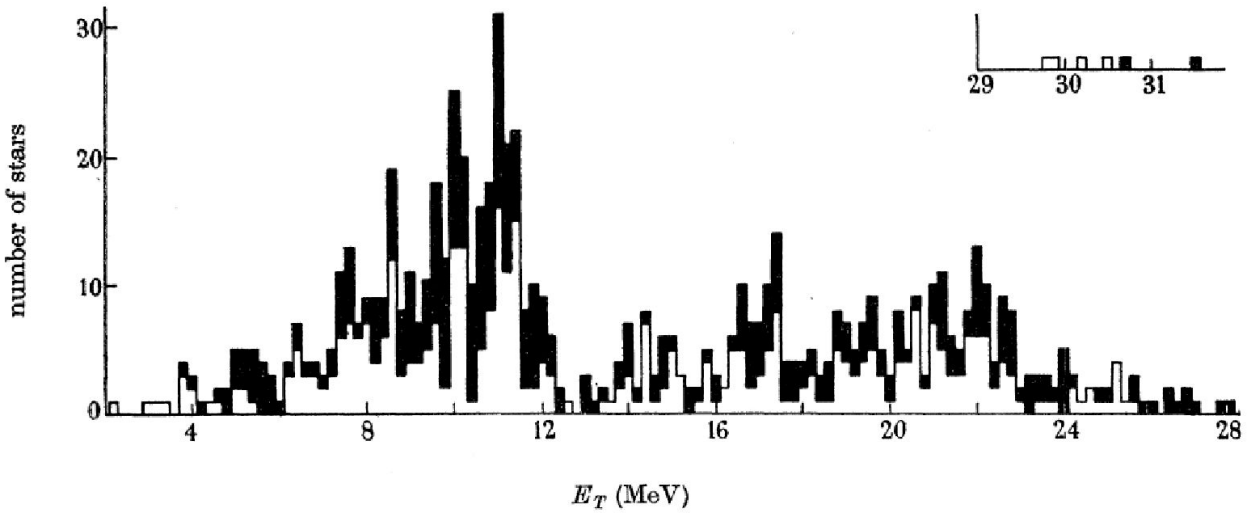

Fig. 54. Energy-release E_T histogram of $^{12}C(\gamma,3\alpha)$ stars produced by 33 MeV and 70 MeV bremsstrahlung beams (taken from (Goward and Wilkins 1953).

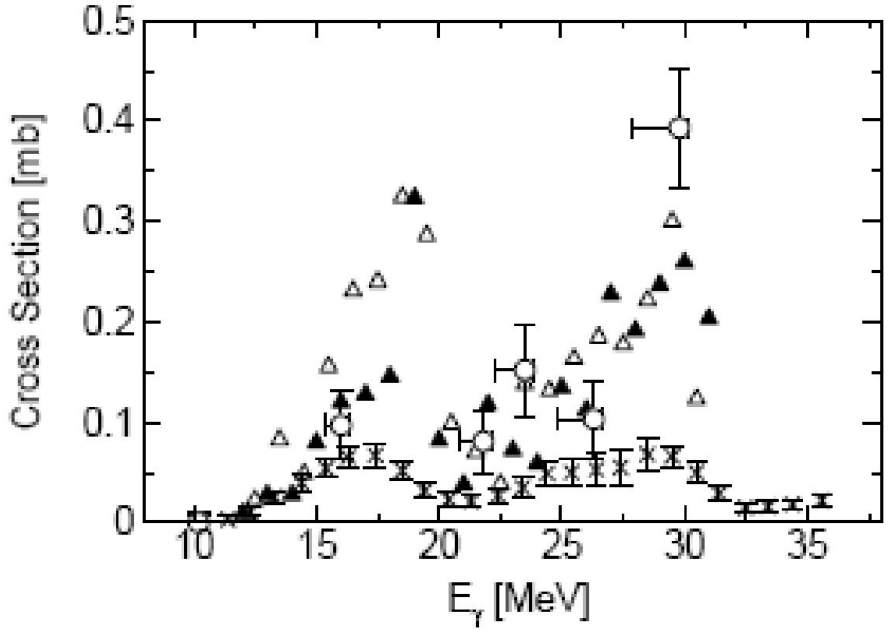

Fig. 55. The $^{12}C(\gamma, 3\alpha)$ reaction cross sections. Closed triangles; Maikov et al. (V. N. Maikov 1958), open triangles; Murakami et al. (Murakami 1970), diagonal crosses; Kotikov et al. (Kotikov et 2002), open circles; Shima (Shima 2006)

Recently the $^{12}C(\gamma,3\alpha)$ channel has been studied by using a Compton backscattered γ-ray beam (Shima 2006). Some preliminary results obtained with such a beam and a Time Projection Chamber (TPC) filled with 20% methane (CH_4) and 80% natural helium are shown in Fig. 55. The total pressure of the gas mixture was 1000 Torr.

The photodisintegration of carbon into three α-particles have been studied using a bremsstrahlung photon beam with $E_{\gamma max}$ = 150 MeV and a diffusion chamber placed in a 1.5 T magnetic field (Afanas'ev and Khodyachikh 2004). The chamber was filled with a mixture of 12.5% methane (CH_4) and 87.5% helium pressure near at a pressure around 1 bar. The use of a diffusion chamber offers some advantages: an almost background-free target; a low (~300 keV) threshold for α-particle registration due to the low density of the target; reliable identification of reaction products using the magnetic field and ionization energy losses. The obtained total cross-section of the $^{12}C(\gamma,3\alpha)$ reaction in the energy interval from the reaction threshold up to 40 MeV is presented in Fig. 56(a).

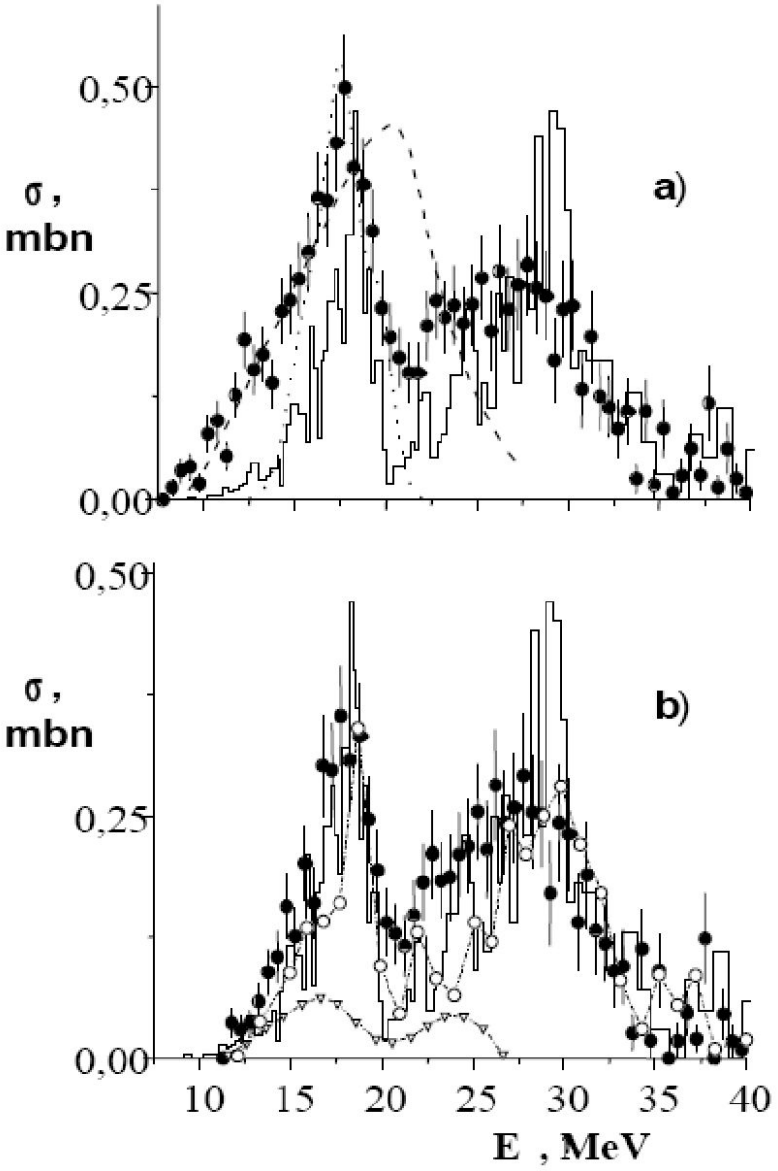

Fig. 56. The total cross-section for the $^{12}C(\gamma, 3\alpha)$ reaction, histogram (Goward and Wilkins 1953), closed circles(Afanas'ev and Khodyachikh 2004), open circles(V. N. Maikov 1958), open triangles (Kotikov et 2002) (see text for details).

The error bars are statistical. The integrated cross-section is 5.58 ± 0.16 MeV mb. Two maxima are observed in the carbon excitation distribution. The first one is at $E_\gamma = 17.17 \pm 0.12$ MeV with a half-width 2.65 ± 0.14 MeV, and the second one is at $E_\gamma = 27.12 \pm 0.34$ MeV with a half-width 4.56 ± 0.14 MeV.

For comparison, the results of earlier works (V. N. Maikov 1958; Murakami 1970; Shima 2006) are presented in Fig. 56(a) (reproduced from (Afanas'ev and Khodyachikh 2004)). It should be noted that the structure of the distributions is similar with two maxima. However the cross-section values differ noticeably. In the near-threshold region the cross-section, obtained with the diffusion chamber, exceeded the results of all the previously performed measurements and showed evidence of resonance like behavior at photon energies 9.5 MeV and 10.5 MeV. About 30 % of events detected by the diffusion chamber have, at least, one α - particle with a kinetic energy less than 1 MeV (Afanas'ev and Khodyachikh 2004). In Fig. 56(b) the points display the total cross-section determined without these events. The results are in better agreement with the other data. Therefore one can conclude that a low density detector is needed for detection of all events, especially events with low-energy alpha particles near the threshold energies. The second 2^+ state of ^{12}C, predicted over 50 years ago as an excitation of the Hoyle state, has been observed in a $^{12}C(\gamma, \alpha)^8Be$ reaction (Zimmerman et al. 2013). An O-TPC operating at 100 torr with the gas mixture of CO_2 (80%) and N_2 (20%) (Gai et al. 2010) was used to detect the outgoing alpha particles. Data were collected at beam energies between 9.1 and 10.7 MeV using the gamma-ray beams at the HIγS facility. The total E1 and E2 cross sections and the relative E1-E2 phase (ϕ_{12}) extracted using the angular distribution data are shown in Fig.57.

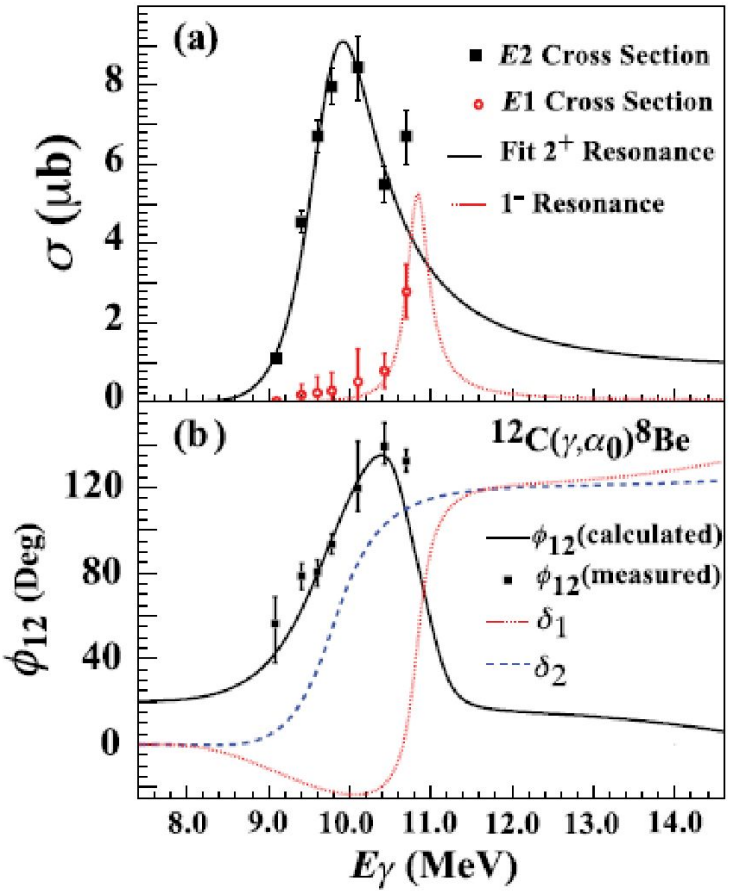

Fig. 57 (color online). (a) The measured E1 and E2 cross sections of the $^{12}C(\gamma, \alpha)^{8}Be$ reaction. (b) The measured E1-E2 relative phase angle (ϕ_{12}) together with the phase angle calculated from a two-resonance model (taken from (Zimmerman et al. 2013)).

The expected rate of the $^{12}C(\gamma, \alpha)^{8}Be$ reaction in this setup, if assume 50% detection efficiency, will be about 7events/μb/h.

Sources of errors and their estimated magnitudes

Experiment	Energy (MeV)	Statistic error	Systematic error
Study of electromagnetic background	8	Rejection factor ≤ 10^{-9}	Rejection factor ≤ 10^{-9}

Study of the $^{16}O(\gamma,\alpha)^{12}C$ reaction	9.5	≤ 5%*	≤ 5%
Study of the $^{12}C(\gamma,\alpha)^{8}Be$ reaction	9.5-15.5	≤ 5%	≤ 5%

* 5% statistical error for cross sections ≥ 5 μb.

1. Run Plan

• equipment setup and alignment; 8 hrs

• setup commissioning and instrumentation calibration without beam; 8hrs

• data collection with beam; 200 hrs

• post-measurement calibrations without beam; 8 hrs

• decommissioning (removal of equipment from beam line). 8 hrs

Chapter 4

A new approach for decay pion spectroscopy

Abstract

In this section we will discuss the application of MWPC in decay pion spectroscopy of light hypernuclei at electron- and proton-beam facilities, using the recoil distance technique for separation of produced hypernuclei and a magnetic spectrometer for precise measurement of the decay pion momentum. In chapter 1, 2 we presented the distinct features of Low-pressure MWPCs: registering low energy charged particles, providing position and time information, highly insensitive to gamma-ray and electron background. This feature can be useful for low-energy nuclear recoil detection. By using the present proposed approach the rate of the detected hypernuclei can be increased by one-to-two orders of magnitude compared to a recent experiment carried out at the MAMI electron accelerator in Mainz. The possibility of realizing a high luminosity decay pion spectroscopy experiment with proton beams is also discussed.

Introduction

The binding energy of the Λ hyperon in the hypernuclear ground state gives one of the basic pieces of information on the Λ-nucleus interaction. This binding energy is defined as:

$$B_{\Lambda}(g.s.) = M_{core} + M_{\Lambda} - M_{HY}$$

where M_{core} is the mass of the nucleus that is left in the ground state after the Λ particle is removed, M_{HY} is the mass of the initial hypernucleus and M_{Λ} is the mass of the Λ. The binding energies B_A have been measured in emulsion-based experiments for a wide range of light ($3 \le A \le 15$) hypernuclei (Gajewski et al. 1967; Bohm et al. 1968; Jurič et al. 1973), exclusively from kinematic analysis of their weak π^- -mesonic decays. The binding energies of light hypernuclei provide the most valuable experimental information to constrain various models of the Y-N interaction. Table III, where the numbers are taken from reference (Nemura, Akaishi, and Suzuki 2002), lists the Λ separation energies obtained from *ab initio* theoretical calculations using different Y-N interactions, along with the existing experimental results. In addition to the quoted statistical errors, the experiments also have systematic errors of about 0.04 MeV. Precise experimental measurements of the binding energies of light hypernuclei can discriminate between various models of Y-N interactions. In particular, accurate measurements of the separation energies of light Λ-hypernuclei are a unique source of information on charge symmetry breaking in the Λ –N interaction in Λ-hypernuclei (Gal 2015; Gazda and Gal 2016).

Table III. Λ separation energies, B_Λ given in units of MeV, of A = 3-5 Λ hypernuclei for different Y-N interactions.

Y-N	$B_\Lambda(\Lambda 3H)$	$B_\Lambda(\Lambda 4H)$	$B_\Lambda(\Lambda 4H^*)$	$B_\Lambda(\Lambda 4He)$	$B_\Lambda(\Lambda 4He^*)$	$B_\Lambda(\Lambda 5He)$
SC97d(S)	0.01	1.67	1.20	1.62	1.17	3.17
SC97e(S)	0.10	2.06	0.92	2.02	0.90	2.75
SC97f(S)	0.18	2.16	0.63	2.11	0.62	2.10
SC89(S)	0.37	2.55	Unbound	2.47	Unbound	0.35
Experiment	0.13±0.05	2.04±0.04	1.00±0.04	2.39±0.03	1.24±0.04	3.12±0.02

In 2007 the use of magnetic spectrometers to measure precisely the momenta of

pions from weak, two-body decays of electroproduced hyperfragments was proposed for Jefferson Lab (Margaryan et al. 2006; Grigoryan et al.,) A similar experimental program was started at MAMI in Mainz (Esser et al. 2013), where the first high resolution spectroscopy of pions from decays of strange systems was performed after electro-disintegration of a 9Be target (Esser et al. 2015; P. Achenbach et al. 2016, 2011). About 103 weak pionic decays of hyperfragments and hyperons were observed in a two-week period (~150 h). The pion momentum distribution shows a monochromatic peak at p ≈ 133 MeV/c, corresponding to the unique signature for the two-body decay of hyper hydrogen $\Lambda 4H \rightarrow 4He + \pi^-$, where the $\Lambda 4H$ stopped inside the target. Its binding energy was determined to be B_Λ = 2.12±0.01 (stat.) ± 0.09 (syst.) MeV with respect to the $3H + \Lambda$ mass.

In the 2012 and 2014 experiments the MAMI beam, with an energy of 1.5 GeV and a current of 20-50 μA, was incident on a beryllium foil of either 125 mm or 250 mm thickness. The ^{9}Be target was tilted by 54° with respect to the beam direction to minimize the energy straggling of negative pions leaving the target in the direction of the spectrometer. A significantly thicker target with the same arrangement would have caused too large a spread of the pion momentum. Also, an increase in the luminosity could not be achieved by an increase of the beam current, due to high counting rates in the forward angle kaon spectrometer. Even a factor of two increase of the beam intensity would have raised the count rate caused by background coincidences beyond an acceptable level.

Recently a new experiment was proposed at MAMI for the study of the binding energy of the Λ in the lightest hypernucleus: the hypertriton, which can reveal important details of the strong nucleon-hyperon interaction. In this experiment a new design of lithium target was considered to increase the rate of the detected hypernuclei by about an order of magnitude (Patrick Achenbach et al. 2018).

We propose a new experiment to perform decay pion spectroscopy of light

hypernuclei, using the recoil distance technique for separation of produced hypernuclei and a magnetic spectrometer for precise measurement of the decay pion momentum. Low-pressure MWPCs are proposed for low-energy recoil detection since they provide precise position and time information, and are highly insensitive to electrons and gamma rays. Possible experimental studies at the MAMI electron-scattering facility and the JPARC proton beam facility are discussed.

The Hyperfragment Electroproduction Experiment at MAMI-C

This experiment was carried out by the A1 Collaboration at the spectrometer facility at the Mainz Microtron MAMI . A 1.508 GeV electron beam with a current of 20 μA was incident on a 125 μm thick ^{9}Be target foil angled at 54 degrees with respect to the beam direction. Pions were detected by two high-resolution spectrometers (SpekA and SpekC), each having a quadrupole-sextupole-dipole-dipole(QSDD) configuration (Fig. 58, left).

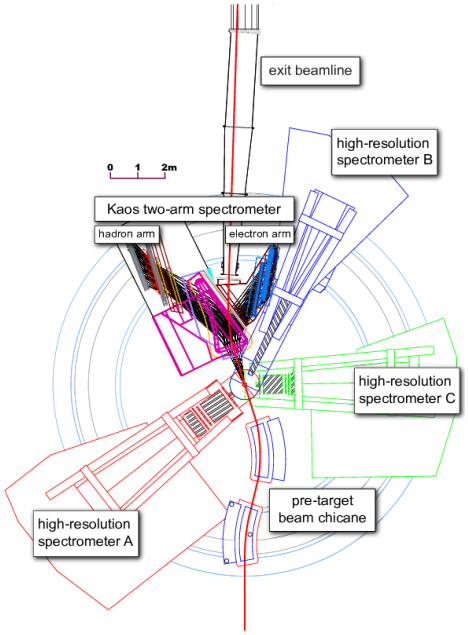

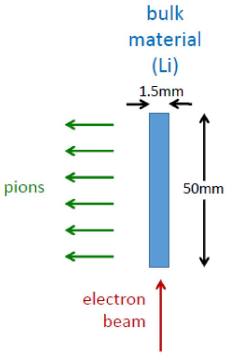

Fig. 58. Left: floor plan of the electron beam-line and magnetic spectrometers in the experimental hall at the Mainz Microtron MAMI. Right: schematic of the lithium target, which is proposed for new experiments at MAMI.

The spectrometers achieve a relative momentum resolution of $\delta p/p \approx 10^{-4}$ and were operated at central momenta of 115 (SpekA) and 125 (SpekC) MeV/c with momentum acceptances of $\Delta p/p = 20\ \%$ (SpekA) and 25 % (SpekC) with a solid angle acceptance 20 - 30 msr. The tagging of kaons was performed by the Kaos spectrometer, positioned at zero degrees with respect to the electron beam direction. The central momentum was 924 MeV/c, covering a momentum range of $\Delta p/p = 50\ \%$ with a solid angle acceptance of $\Omega_K = 16$ msr.

The Fig. 59 shows the pion momentum distribution in SpekC for the events selected within the $K^+ - \pi^-$ coincidence time gate. The distribution above the accidental background is attributed to mesonic weak decay (MWD) events. About 10^3 pionic weak decays of hyperfragments and quasi-free produced hyperons were observed within the entire momentum acceptance of SpekC. The pion momentum distribution shows a monochromatic peak at ~133 MeV/c, corresponding to the unique signature of about 50 two-body decays of $\Lambda 4H \rightarrow 4He + \pi^-$. From this the $\Lambda 4H$ binding energy was determined.

No localized excess of counts over expectations of background from quasi-free hyperon decays were found in the pion momentum distribution of SpekA. This was set to detect decay pions in the momentum range 103-127 MeV/c, which is outside the region of interest for $\Lambda 4H$.

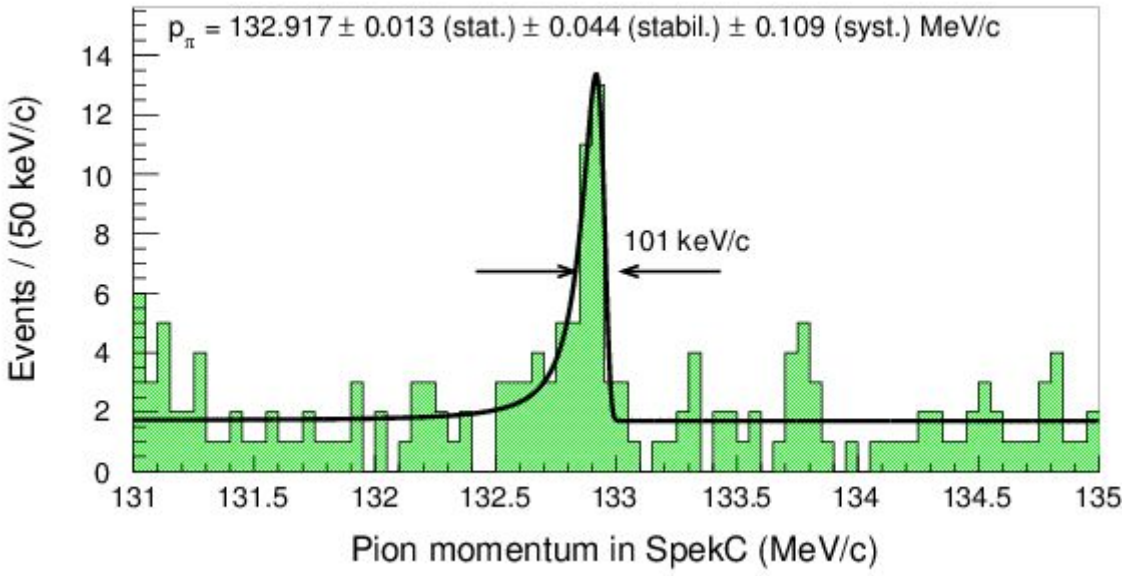

Fig. 59. Pion momentum distribution in SpekC for true coincidences with Kaos. A monochromatic peak at 133 MeV/c was observed which is a unique signature for the two-body decay of 50 stopped hyperhydrogen $\Lambda 4H \rightarrow 4He + \pi^-$.

Statistical model predictions for the hyperfragmentaion yields from for $6,7Li$ and $9Be$ target nuclei, with subsequent two-body pionic decay at rest, are presented in Table IV (for details see (Mornacchi and A2 collaboration 2018)).

Because of the large two-body branching ratio, $\Lambda 4H$ is the most likely hyperfragment to be produced. All other hypernuclear decays are produced with significantly lower rates and, therefore, only $\Lambda 4H$ could be detected with very low statistics in the first experiments. For observation of other hyperfragments, in particular the hypertriton $\Lambda 3H$ or $\Lambda 6H$, one needs to increase the luminosity of the experiment significantly. An increase of the luminosity by about an order of magnitude can be achieved by using a new target geometry at MAMI (Mornacchi and A2 collaboration 2018) (see Fig. 58 (right)) for a schematic view of the target and detection geometry). Instead of employing a tilted target, the beam would be incident on a 1.5mm wide surface of a 50 mm long target block, aligned along the

beam axis. Pions emitted at 90 degrees with respect to the beam direction toward the spectrometers, would traverse only a thin layer of target material, keeping their momentum spread acceptably low.

Table IV: Statistical model predictions for the probabilities in % of forming a hyperfragment LAZ with subsequent two-body π^- decay (Patrick Achenbach et al. 2018).

		^{9}Be target		^{7}Li target	^{6}Li target
ΛAZ	p_π (MeV/c)	$\Lambda^{9}Li^{*}$	$\Lambda^{8}Li^{*}$	$\Lambda^{7}He^{*}$	$\Lambda^{6}He^{*}$
$\Lambda^{3}H$	114.37 ± 0.08	0.56 0.67	1.18	1.49	2.48
$\Lambda^{4}H$	132.87 ± 0.06	3.56 7.51	3.74	12.61	8.81
$\Lambda^{6}H$	135.13 ± 1.52	0.03 0.23	<0.01	0.10	–
$\Lambda^{6}H$	108.47 ± 0.18	2.44 1.47	1.25	3.53	–
$\Lambda^{7}H$	114.97 ± 0.15 ± 0.17	2.12 1.35	0.44	–	–
$\Lambda^{8}H$	116.50 ± 1.08	0.04	– –	–	–
$\Lambda^{7}Li$	108.11 ± 0.05	1.54	1.68 –	–	–
$\Lambda^{8}Li$	124.20 ± 0.05	0.85	– –	–	–

Decay Pion Spectroscopy of the Λ-Hypernuclei: A New Approach

In the experiments described above (Fig.58), the produced kaons and decay pions were detected simultaneously by magnetic spectrometers Kaos for kaons (HKS) and SpekA, SpekC for pions ($H\pi S$).

The detection probability $R_{K^+}(HKS)$ of produced K^+ in the momentum acceptance $P_0 \pm \Delta P$ of HKS is: $R_{K^+}(HKS) = [\Delta\Omega/(4\pi)] \times \varepsilon_s^K \times \varepsilon_{ef} \approx 10^{-3}$, were $\Delta\Omega = 20 - 30$ msr is the acceptance of HKS, $\varepsilon_{ef} \cong 0.5$ is the survival probability of the K^+, $\varepsilon_{ef} \cong 0.5$ is the detection efficiency of the detector package, and the accepted momentum bite $\Delta P \cong 100$ MeV/c. A similar figure is obtained for the detection probability of decayed pions: $R_{\pi^-}(H\pi S) \approx 10^{-3}$. The two events are correlated in time, and their simultaneous detection probability is $R_{K^+\&\pi^-} = R_{K^+}(HKS) \times R(\pi^-) \times R_{\pi^-}(H\pi S)$, where $R(\pi^-) \le 10^{-2}$ is the probability of decay pion formation for each produced K^+ (Grigoryan et al.,). Therefore, for this type of experiment the useful event probability for each produced K^+ is $R_{K^+\&\pi^-} \approx 10^{-8} / K^+$.

The useful event rate can be increased by several orders of magnitude by using the concept of "*delayed-*π^-" spectroscopy (Margaryan et al. 2014). The experimental setup in this case consists only of the decay pion spectrometer, $H\pi S$, i.e. SpekA and SpekC in Fig. 58. The tracking detector package of $H\pi S$ is the same as before, but an ultra-high precision timing detector, based on Cherenkov radiators coupled to Radio Frequency Photomultiplier Tubes (RF PMT) (Margaryan et al. 2017) will be added. The expected time resolution of such detectors is better than 10 ps, FWHM. The expected reconstructed transit-time spread of pions in HπS is ~ 20 ps, FWHM,

and consequently the expected total time resolution is also ~ 20 ps, FWHM. The time structure of the CW electron beams at Jefferson Lab and MAMI has beam buckets of ~ps duration separated at ~ns intervals. By correlating the decay pion time with the particular beam bucket that caused the event, it can be separated from the huge amount of promptly produced background, without detecting K^+ mesons as a positive tag of strangeness production. Indeed, the probability to find promptly produced (non-decay) pions at times larger than 100 ps is less than 10^{-5}, while ~70% of decay pions from Λ or hyperfragments (lifetime 260 ps) are delayed more than 100 ps. Therefore, the $H\pi S$ equipped with RF PMT based Cherenkov detectors will make "delayed π^- spectroscopy", similar to "delayed γ-ray spectroscopy", a feasible technique. The useful, decay pion event probability in a "delayed π^- spectroscopy" experiment is: $R_{\pi^-} = 0.7 \times R_S \times R(\pi^-) \times R_{\pi^-}(H\pi S)$, were R_S is the probability of strangeness production. In this case, all two body reactions, were the virtual photon produces strangeness, contribute. These reactions are: $1: \gamma + p \to \Lambda + K^+$; $2: \gamma + p \to \Sigma^0 + K^+$; $3: \gamma + p \to \Sigma^+ + K^0$; $4: \gamma + n \to \Lambda + K^0$; $5: \gamma + n \to \Sigma^- + K^+$; $6: \gamma + n \to \Sigma^0 + K^0$.

In addition the entire useful virtual photon spectrum participates, unlike previous experiments where only virtual photons producing K^+ with momentum inside the HKS acceptance contributed. Due to this, the expected rate of useful events for "delayed π^- spectroscopy", would be 10^3 times higher than the rate expected in previous experiments.

The RF PMT-Cherenkov detector will also provide an absolute momentum calibration of the $H\pi S$ by measuring the time-of-flight (TOF) differences of pairs of particles with different masses (Margaryan et al. 2017). Monte Carlo simulations demonstrated that the magnetic spectrometers at the MAMI electron-scattering facility can be calibrated absolutely with an accuracy $\delta p/p \leq 10^{-4}$, which will be

crucial for high precision determination of hypernuclear masses (Margaryan et al. 2017). In addition by measuring lifetimes of the low lying hypernuclear states and by applying the "tagged-weak π^- method" (Margaryan et al. 2011), the electromagnetic excitation rates of such states with lifetimes down to $\cong 10^{-11}$ s could be investigated, which is another avenue for hypernuclear studies. The experimental information on these characteristics of the ΛN interaction is essential to test and improve baryon-baryon interaction models, which are needed for a comprehensive understanding of the strong interaction between hyperons and high density nuclear matter (Margaryan et al. 2014).

Here, we propose a new experiment for decay pion spectroscopy of light hypernuclei, which would be suitable both for electron- and proton-beam facilities. Identification of produced hypernuclei is realized by detecting the low-energy recoils and using the recoil distance technique. The general layout of the experimental setup is shown in Fig. 60. The incident electron (or proton) beam hits the 2 mg/cm^2 target and produces a hyperfragment, which exits the target and decays after ~ 200 ps outside the target, resulting in a decay pion and recoil nucleus. The flight distance from the primary interaction point is estimated to be ~ 1 mm. Decay pions are detected in the high-resolution magnetic spectrometer - $H\pi S$ located at ~90 degrees. In this case, the hyperfragment decays outside of the target, and as a result the monochromatic spectrum of produced pions is broadened by kinematics. The recoil nucleus is detected by means of the recoil detector, which is located at the opposite side of the beam to the $H\pi S$. This is a low-pressure (LP) MWPC, which is very insensitive to gamma rays and minimum ionising particles and has good position resolution for the low energy recoiling particles. In this case the decay pion event probability is: $R_{\pi^-}(rd) = \varepsilon(rd) \times R_S \times R(\pi^-) \times R_{\pi^-}(H\pi S)$, where $\varepsilon(rd)$ is the detection efficiency for the recoiling particle after a recoil distance analysis has been performed. It is expected that $\varepsilon(rd) \geq 0.1$, so that the useful, decay pion event

probability is: $R_{\pi^-}(rd) \geq 0.1 \times R_{\pi^-}$, which increases event rate by about two orders of magnitude, compared to previous experiments. In addition, this technique can also be applied to proton induced experiments.

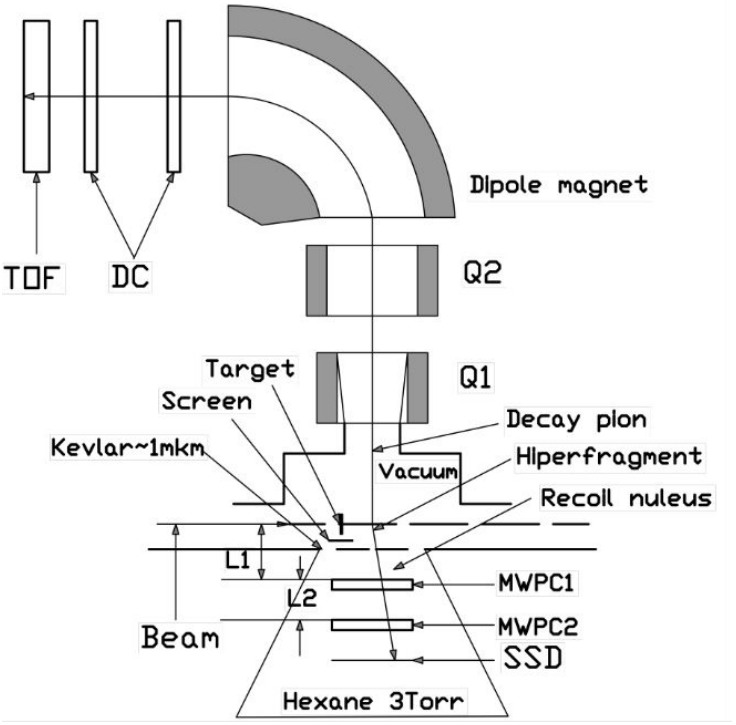

Fig 60. Schematic view of the proposed experiment consisting of the high-resolution pion spectrometer ($H\pi S$) and the low-energy recoil detector for detection of the recoiling nuclei in coincidence with the decayed pions.

Low-Energy Recoil Detector

A Recoil Detector (RD) is shown schematically in Fig. 60. It consists of two LP MWPC units (MWPC1, MWPC2) and a solid state detector (SSD) which form a position, time and energy sensitive low energy particle telescope. The LP MWPCs have an active area of 30×30 mm^2, a separation distance of L2 cm and are windowless to enable passage of low energy nuclear fragments, starting from heavy hydrogen isotopes. Heptane or Hexane at about 3 Torr pressure will be the MWPC

gas. The distance from MWPC1 to the center of the experimental target is L1 and dimensions L1 and L2 (Fig. 60) will be determined in dedicated experimental studies. The target is a thin foil of thickness ~2mg/cm^2, so that most produced hyperfragments exit and decay outside of the target. The RD is screened from the central beam-on-target region, to enhance the signal for hyperfragments produced outside of the target, and separated from the accelerator vacuum by a 1-2 μm Mylar or Kevlar foil. In Fig. 60 the recoiling nuclei are detected by MWPC1, MWPC2 and the SSD, while decay π^- mesons are detected by the magnetic spectrometer HπS. In principle the RD can operate without an SSD. In that case the energy of the recoiling nucleus would be determined by its velocity with its type determined from the decay pion momentum.

To be detected, low-energy recoils, i.e. low-energy ^3He, ^4He, ^6He (and heavier species) require enough energy to pass through the Kevlar window and both MWPC units. In Fig. 61 the stopping powers (differential energy losses) and ranges for H, He and C ions in hexane, simulated using the SRIM software package (ZIEGLER, F. J) are displayed. Fig.62 presents the corresponding distributions for Kevlar.

From Fig. 61 and 62 we calculate that an LPMWPC based RD system (Fig. 60) filled to 3 torr with hexane is capable of detecting ^3He, ^4He, ^6He recoils with energies above 35, 50, 70, keV and ^{12}C nuclei with energies higher than 100 keV.

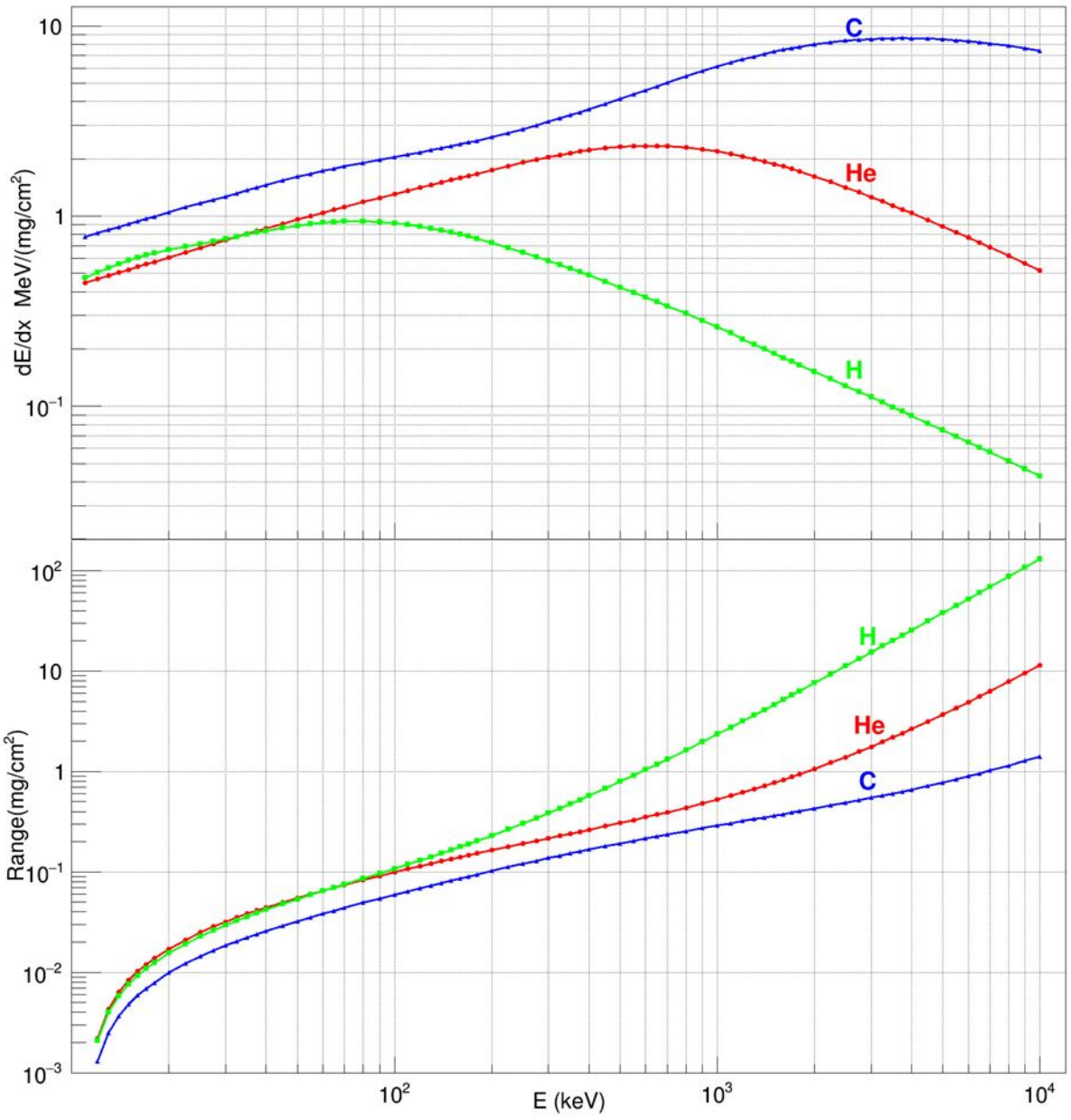

Fig. 61. The stopping powers and ranges of H, He and C ions in Hexane vs. energy.

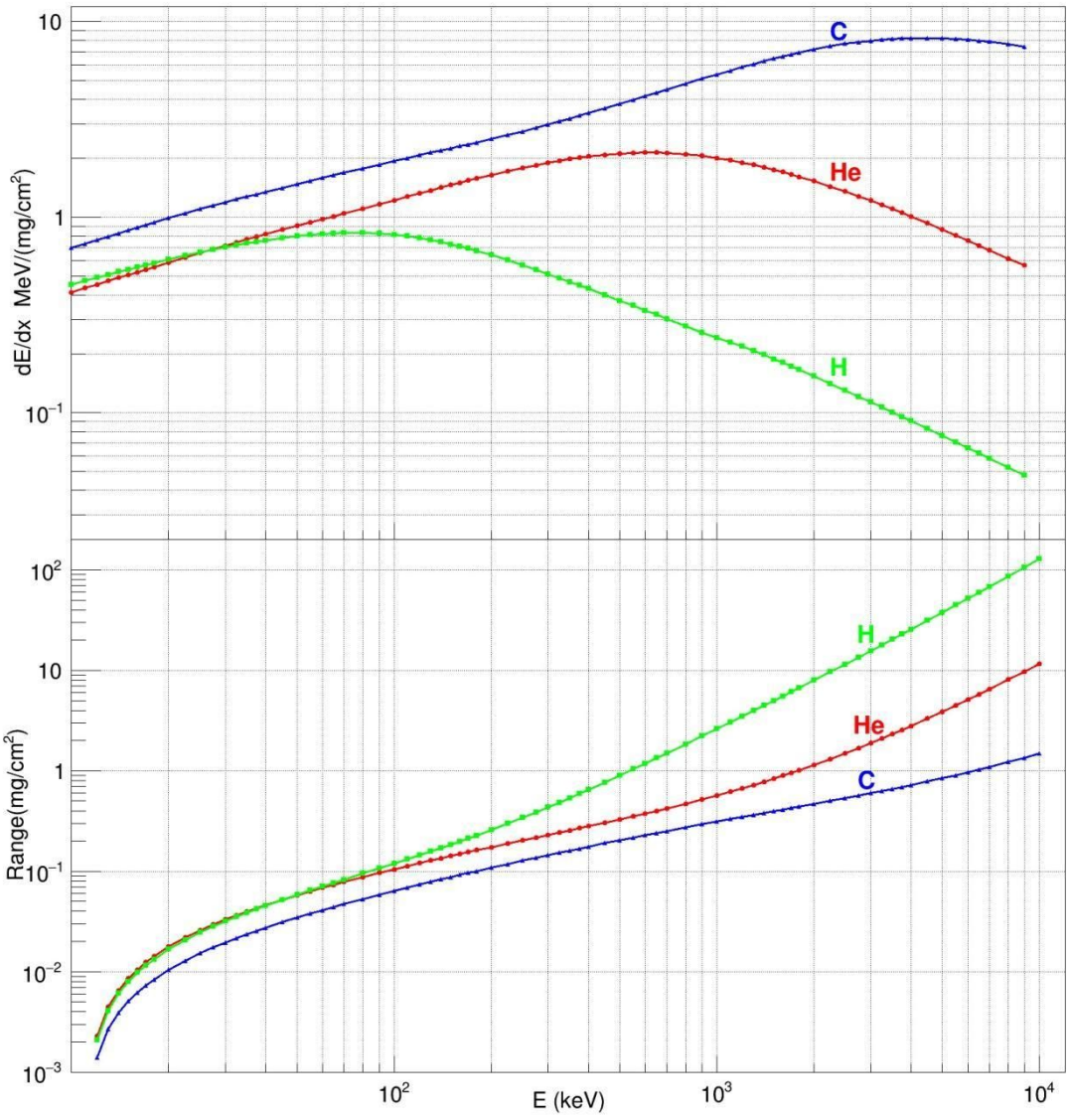

Fig. 62. The stopping powers and ranges of H, He and C ions in Kevlar vs. energy.

Since the RD will be located near to the incident beam to maximize the geometrical acceptance it is expected that many background particles, e.g. due to electromagnetic processes, will be produced. Even though the sensitivity to electrons and photons is very low, the rate capability of the MWPC units is a crucial factor. As we showed in the Chapter 2 MWPC has the capability to operate properly at rates in excess of 1 MHz.

The rejection factor for a single MWPC unit, i.e., the ratio of β-particle to α-particle detection efficiencies is about 10^{-4} for the 30 mV thresholds used typically in the electronics. Since the recoil nuclei will be detected in two MWPC units, the overall β-particle/α-particle detection efficiency will reduce to ~10^{-8}. A more quantitative value for this rejection factor and other characteristics of the RD will be obtained under realistic experimental conditions in future test experiments.

Monte Carlo Simulation Studies

The Monte Carlo simulation consists of a hypernuclear event generator which feeds particles into a model of the detection apparatus. Using the simulated response (energy, time, position, etc.) of the detectors, the effective masses and binding energies have been reconstructed in a manner analogous to a real experiment. The hypernuclear mass (M_{HY}) was calculated using the kinematic relation:

$$M_{HY} = \sqrt{\left(m_R^2 + m_\pi^2 + 2\times\sqrt{p_R^2 + m_R^2}\times\sqrt{p_\pi^2 + m_\pi^2} - p_R p_\pi cos\,(\psi)\right)} \qquad (19)$$

Where m_R and m_π, p_R and p_π are the masses and momenta of the recoil nucleus and decay pion, respectively and ψ is the angle between recoil nucleus and pion (the so called folding angle). Thus there are three kinematic variables to be measured: p_π, p_R and ψ. In the Monte Carlo simulations we assumed the following:

1. The momentum distribution of the produced hypernuclei is assumed to be isotropic in angle with uniformly distributed magnitude in the range 0-100 MeV/c. Hypernuclei are assumed to be produced outside of the target.
2. The relative momentum resolution ($\Delta p/p$) of the pion spectrometer ($H\pi S$) is described by a Gaussian of width $\sigma_p = 10^{-3}$.
3. The energy resolution of the RD is described by a Gaussian of width $\sigma_E = 50$ keV.

4. The folding angle precision is described by a Gaussian of width $\sigma_\psi = 2$ degree.

A simulated distribution of the folding angle between ^3He and π^- for $^3_\Lambda H \to {}^3He + \pi^-$ decays is shown in Fig. 63. This distribution shows that the $3He$ recoil nuclei are directed in the angular region around 180 deg. relative to the π^- direction. This can be used to optimize the design of the geometry of the RD.

Simulated distributions of recoil-nucleus energies, decay-pion momenta, binding energies and track lengths of hypernuclei for $^3_\Lambda H \to {}^3He + \pi^-$ and $^4_\Lambda H \to {}^4He + \pi^-$ decays are shown in Fig. 64 and Fig. 65 respectively. For the decays we assume the Λ binding energy for $^6_\Lambda H$ to be $4.18\,MeV$ which is the Λ binding energy of the hypernucleus. The resulting distributions are shown in Fig. 66.

The resulting resolutions ($\Delta p/p$) for decay-pion momenta arise from two body kinematics and lie in the range 1-2% (r.m.s.). The resolutions for binding energies, which are calculated on the basis of Eq. 3, are about 120 keV (r.m.s.).

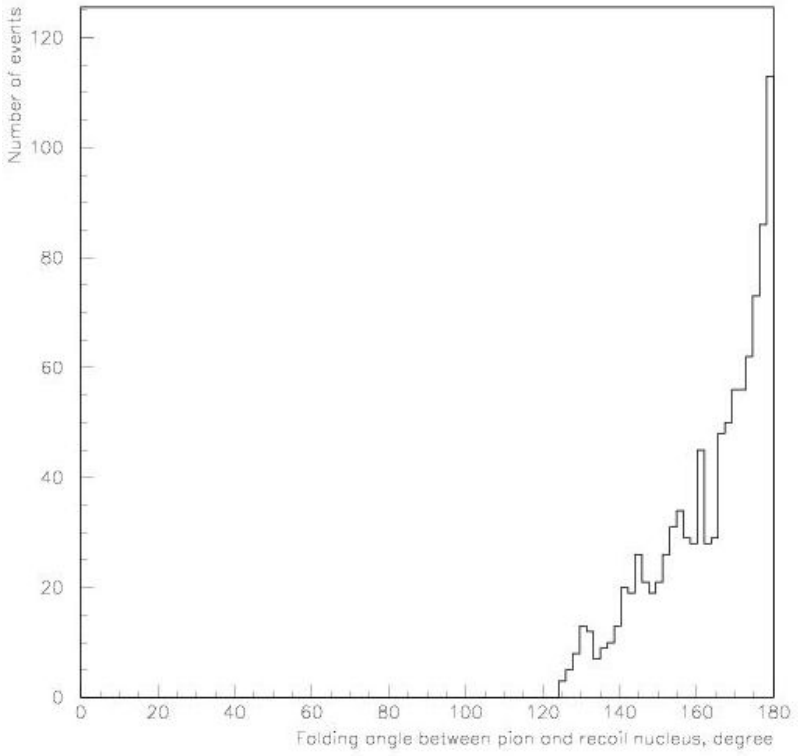

Fig. 63. The simulated folding angle distribution between the pion and recoil nucleus, for ${}^{3}_{\Lambda}H \to {}^{3}He + \pi^{-}$ decays.

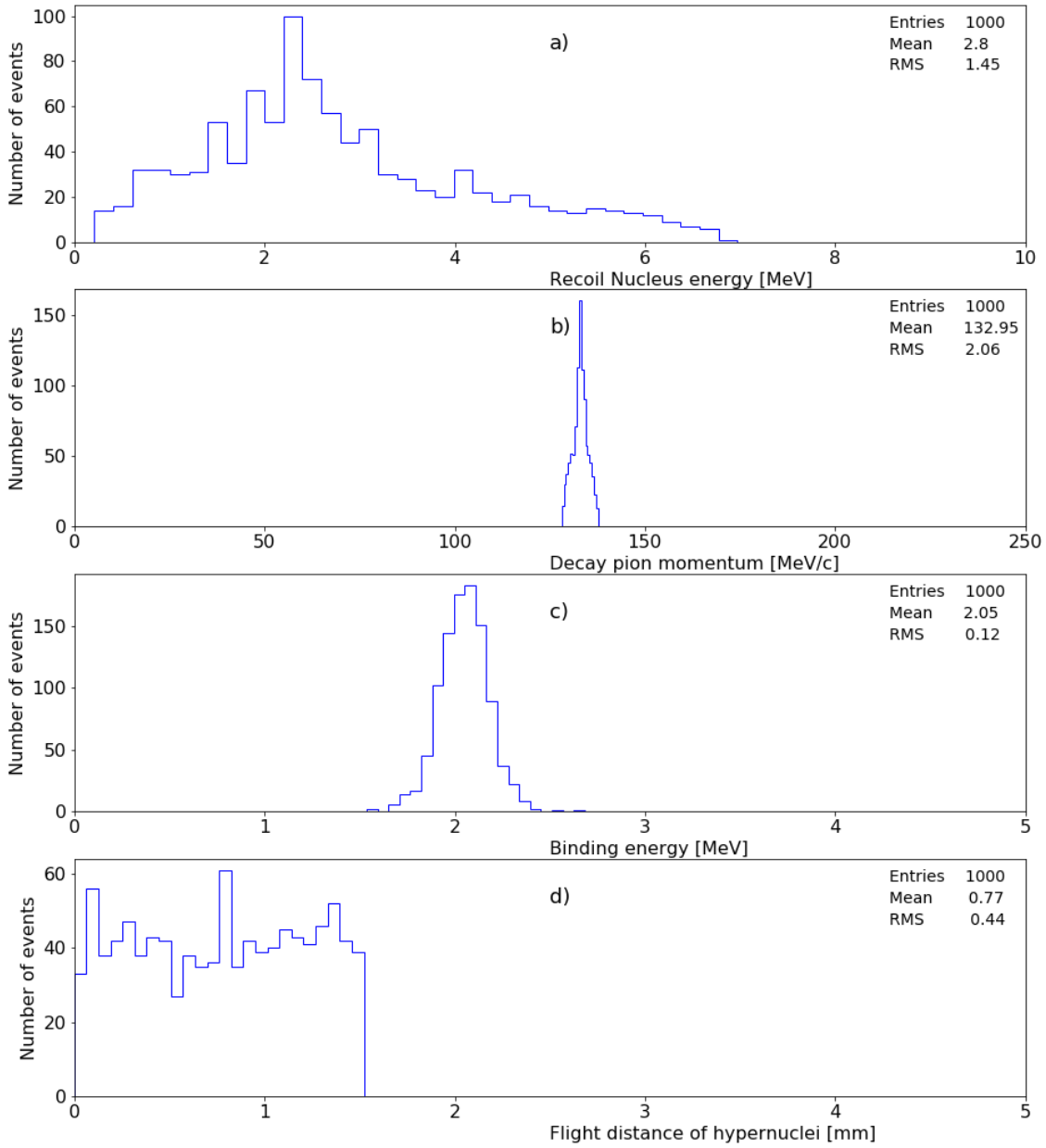

Fig. 64 Simulated distributions for ${}^{3}_{\Lambda}H \to {}^{3}He + \pi^{-}$ decays: energy of ${}^{3}He$ (a), decay pion momentum (b), binding energy (c), and flight distance of ${}^{3}_{\Lambda}H$ hypernuclide (d).

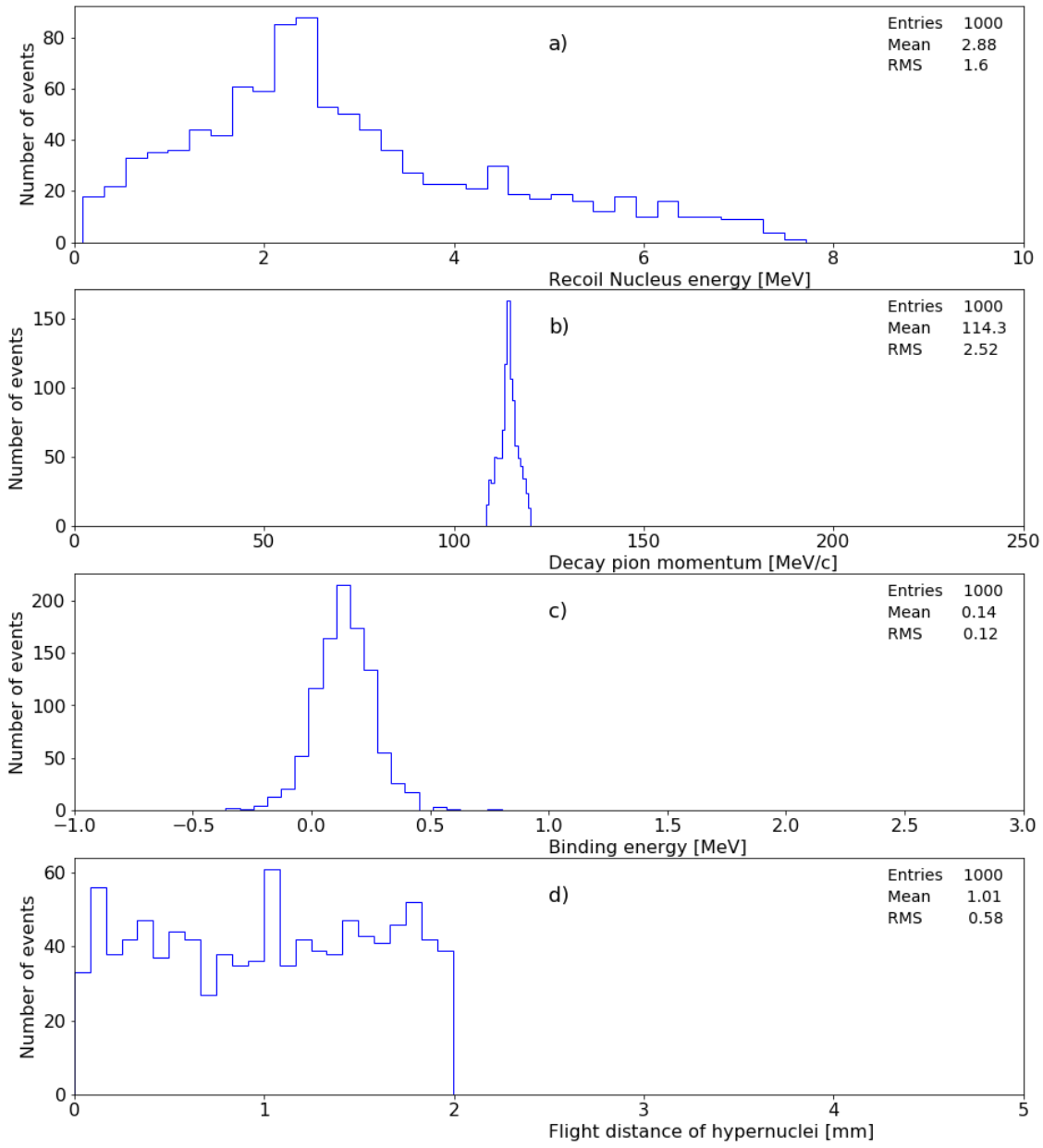

Fig. 65. Simulated distributions for ${}^{4}_{\Lambda}H \rightarrow {}^{4}He + \pi^{-}$ decays: energy of ${}^{4}He$ (a), decay pion momentum (b), binding energy (c), and flight distance of ${}^{4}_{\Lambda}H$ hypernuclide (d).

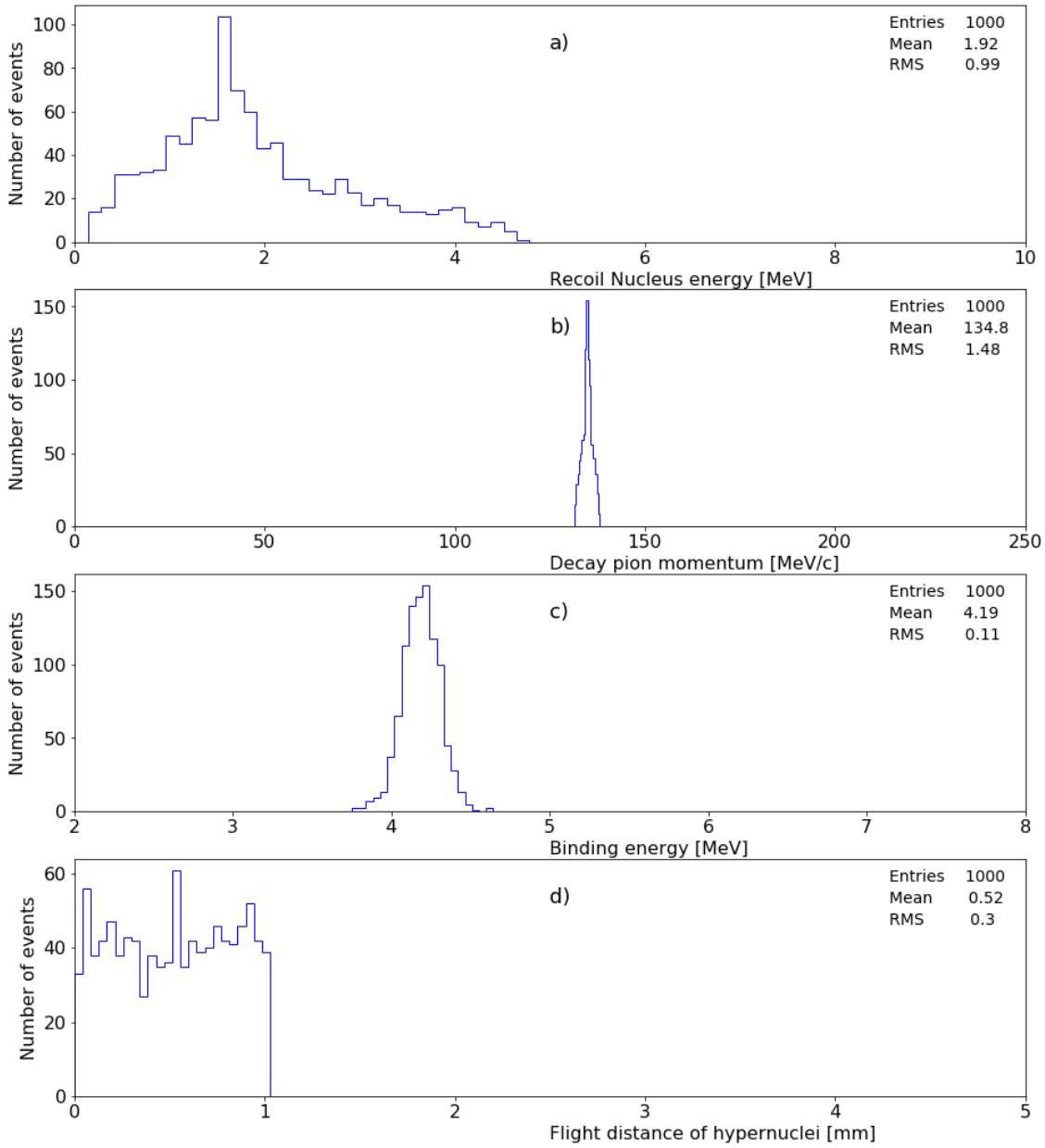

Fig. 66. Simulated distributions for ${}^{6}_{\Lambda}H \to {}^{6}He + \pi^{-}$ decays: energy of ${}^{6}He$ (a), decay pion momentum (b), binding energy (c), and flight distance of ${}^{6}_{\Lambda}H$ hypernuclide (d).

Background

In real experimental conditions the monochromatic pion spectra will be masked by a huge amount of background originating from three sources:

a) Promptly produced pions;

b) Decay pions from Λ particles produced by "quasi-free" processes;

c) Accidentals.

The promptly produced pions will be excluded by detection of the recoil nuclei, using a "vertex cut" which requires the reaction point (in the target) and the decay point (outside of the target) to be separated. The RD, which will be screened from direct view of the target, will provide precise determination of the trajectories of recoiling nuclei.

The "quasi-free" background will be suppressed by identification of the heavy recoiling particle species by the RD.

After screening from the target, the RD rate will be much lower than that of the HKS (Sec.2) which was used in previous Mainz experiments to identify hypernuclear events. As a result the level of accidentals between the RD and $H\pi S$ will be much lower than was observed previously between the HKS and $H\pi S$.

Detailed MC studies of background processes, which include realistic models of experimental geometry and the RD response, are in progress.

Yield Estimation

Yield estimate for experimental studies at MAMI

In the first experiment at MAMI, a 1.508 GeV, 20 μA electron beam was directed at a 125 μm thick ^{9}Be target, tilted at 54° to give an effective thickness of 27.7 mg/cm2. About 50 events from the two-body decays of stopped hyperhydrogen $\Lambda^{4}H \rightarrow {}^{4}He + \pi^{-}$ were observed in a period of ~150 h. On this basis we estimate the rates for the proposed new experiment. The target in a new experiment must be about 10 times thinner to allow hyperfragments to exit and decay outside of the target. However the decay pion detection probability in similar experimental conditions (Sec. 2) is more than two orders of magnitude higher than previous experiments.

Therefore the event rate will be increased more than an order of magnitude. In addition the quasi-free background will be eliminated, since recoil detection excludes weak decay pions from quasi-free produced Λ-particles.

Yield estimate for internal target experiments

Electron-beam experiments would also be possible at an internal-target facility on a stored-beam accelerator, such as the Yerevan electron synchrotron. Some characteristics of the Yerevan electron synchrotron are listed in Table V and are used to estimate potential hyperfragment yields at this facility.

Table V: Parameters of the Yerevan electron synchrotron.

Energy (GeV)	1.5
Mean radius (m)	34.49
Mean orbit length (m)	216.72
RF frequency (MHz)	132.79
Circulating current (mA)	22
Intensity (electron/cycle)	10^{11}
Intensity (electron/second)	5×10^{12}
Number of accelerated cycles Injection frequency?	50
Revolution period (μs)	0.723
Electron bunch length (ns)	0.7
Number of bunches	96
Electron internal target interaction time (ms)	2
Duty factor (%)	10

We will consider a 1.5 GeV electron beam and a $9Be$ target with thickness of 2.8 mg/cm^2. For stored-beam electron accelerators, the effective target length is equal to about 0.1 radiation length (r. l.) of the employed target material, due to the multiple passing of electrons through the target. This means that the effective length of the thin $9Be$ target becomes ~ 6.5 g/cm^2 equivalent to around 2300 beam passes through the target. For a modest 3 mA stored electron beam a 2.8 mg/cm^2 thick target (which is equivalent to 7×10^{11} electron/second and 6.5 g/cm^2 target thickness) and with a similar experimental setup to that described in Sec.3 for the extracted beam situation, we estimate 500(events)×6.5(g/cm^2)×0.11(μA)/20(μA)/.0028(g/cm2) ≈ 6000 events in a period of 150 hrs, i.e. more than an order of magnitude increase in event rate compared to an extracted-beam experiment. This kind of experiment could also be realized at the stretcher-booster ring of Tohoku University (Hinode et al., n.d.).

It is also worth mentioning that the first experiments performed at the Yerevan electron synchrotron were small-angle elastic electron scattering from the proton and deuteron, where the recoiling proton or deuteron was detected using solid state detectors (Akimov et al. 1972).

Yield estimation for experimental studies at proton beams

The proposed experiment can also be realized with proton beams. In this case the expected hyperfragment production rates can be estimated from old emulsion data (Fry 1958) or from recent theoretical predictions (Sun et al. 2018). In that work the theoretical production cross section of a $12C$ beam impinging on a hydrogen target with energies from 1 to 10 GeV/nucleon is calculated for $\Lambda2n$, $\Lambda3n$, $\Lambda3H$, $\Lambda4H$, $\Lambda6H$, $\Lambda7Li$, and $\Lambda7Be$ hypernuclei and it was predicted that the $\Lambda4H$ production cross section in $12C + 1H$ collisions at 5 GeV is about 10 μb. The two-body decay probability of heavy hyperhydrogen $\Lambda4H \rightarrow 4He + \pi^-$ is 0.5. Taking this into

account the $\Lambda 4H$ production and two body decay rate for a 5 GeV, 1 μA proton beam incident on a 2.8 mg/cm^2 thick $12C$ target can be estimated to be $6\times10^{12}\times0.5\times10^{-29}\times2.8\times10^{-3}/12\times6.02\times10^{23}$/s = 4.34×10^3/s. For the detected decay pion rate we have $R_{\pi^-}(pC) = \varepsilon(rd)\times\varepsilon(\pi^-)\times4.34\times10^3 \geq 0.4\ event/s$, where $\varepsilon(rd)\geq0.1$ and $\varepsilon(H\pi S) \sim 10^{-3}$ are the efficiencies of the RD and pion spectrometer with geometrical acceptances included. Even a modest 1 μA proton beam current produces a huge increase in the detected $\Lambda 4H$ hyperfragment rate, namely 216000 in a 150 h beam time, compared to 50 events observed at MAMI with a 20 μA electron beam. Thus experiments with a proton beam will be ideally suited for the detection of the very rare hyperfragments such as $\Lambda 6H$ and $\Lambda 8H$. Recently $\Lambda 2n$ and $\Lambda 3n$ exotic hypernuclei were extensively discussed and looked for in relativistic ion experiments and also in an electron scattering experiment (Rappold et al. 2013; Dönigus 2015; Tang et al., n.d.) . If such bound systems exist in nature they could be observed after a proton-carbon interaction by the mesonic decay processes $\Lambda 2n \rightarrow d + \pi^-$ and $\Lambda 3n \rightarrow t + \pi^-$.

Discussion

A new experiment for two-body π^- decay spectroscopy of light hypernuclei is proposed. It employs a magnetic spectrometer for precise measurement of the decay pion momentum in conjunction with a detector of the recoiling nucleus for separation of produced hypernuclei from background. Low-pressure MWPCs are proposed as the position and time sensitive devices for low-energy recoil detection and their position and timing characteristics have been studied using ~5 MeV α-particles. The desirable features of this recoil detector include: good timing and position resolution; high rate capability; identification of heavy recoils; large acceptance ≥0.1; insensitivity to electromagnetic background and minimum ionizing particles.

Experiments of this type can be carried out using electron, photon or proton beams

and Li, Be, or C targets. Produced hyperfragments such as ${}^{\Lambda 3H}$ and $\Lambda 4H$, $\Lambda 6H$ and $\Lambda 8H$ exit the target and decay in the vacuum. The monochromatic momentum spectrum of the produced pions is broadened by kinematics, but the absolute value is not changed by any secondary process such as ionization energy losses before detection in the magnetic spectrometer. Therefore average values of the π^- momenta will reproduce exactly the two-body decay kinematics, so that they can be used for accurate determination of the binding energies of Λ-particles in light hypernuclei. This is especially crucial for the lightest hypernucleus, $\Lambda 3H$, for which the binding energy of the Λ-particle is about 0.130 MeV.

For experiments with electron beams a simple analysis estimates that the expected yields of detected hyperfragments will be one-to-two orders of magnitude higher than was observed in previous experiments carried out at MAMI. Two-body π^- decay spectroscopy of $\Lambda 3H$ and $\Lambda 4H$ hyperfragments using an RF structured electron beam and RF PMT based time-of-flight detectors will provide ultra-precise values of the binding energies of Λ-particles to $\Lambda 3H$ and $\Lambda 4H$ hyperfragments. These can be used to check theoretical predictions and as a reference for other hyperfragments.

Experiments with proton beams will have a very high yield compared to electron experiments. They can be used to extend the study of light hypernuclei to the exotic $\Lambda 2n$ and $\Lambda 3n$ hypernuclei and to the heavy hyperhydrogens $\Lambda 6H$ and $\Lambda 8H$.

In all cases, for realistic estimation of expected hyperfragment yields, test studies are needed to determine the maximum intensity of the incident electron/photon or proton beams at which the recoil detector will operate smoothly.

The described detector system may also be useful to study exclusive breakup reactions in low energy electron scattering experiments (e.g. 3He(e,e'd)p or 7Li(e,e'd)5He) where a low momentum recoil nucleus needs to be detected (see e.g. (Merkel, n.d.)).

Chapter 5

Ionization Energy Losses of Low-Energy Alpha Particles in Methylal

Abstract.

The ionization energy losses of alpha particles have been measured in Methylal gas and compared with the Stopping and Range of Ions in Matter SRIM-2013. The alpha particle energy losses have been experimentally determined for ^{239}Pu α-particle source using a dedicated experimental setup based on low-pressure multi-wire proportional chambers(LPMWPC); such losses are observed to deviate significantly from the calculated ones. The deviations suggested that in the low (≤ 1 MeV) energy region the stopping powers given by SRIM-2013 might be overestimated of about 5-10%.

Introduction

Stopping of charged particles and ions in the matter has been a subject which has received great theoretical and experimental interest. Stopping powers have been reviewed in many articles (see e.g. Ahlen 1980; Kaplan 1963; 1980). Stopping and Range of Ions in Matter (SRIM-2013) (ZIEGLER and F J) software acquires the most updated dataset of stopping powers in different media. In the present work, we compare the alpha-particle energy losses in Methylal obtained from experiments and from stopping powers given SRIM-2013. The ionization energy losses of alpha-particles have been experimentally determined for ^{239}Pu source using dedicated experimental setup; such losses are observed to deviate significantly from the calculated ones. The deviations suggested, that in the energy region less than 1 MeV,

the stopping powers given by SRIM-2013 might be too high of about 10%, which is also suggested in other works as well(Yu et al. 2003). In the present work, we propose a new method to verify these stopping powers. In this method, the alpha-particle energy losses in Methylal are measured directly by using a dedicated experimental setup based on Low-Pressure Multi-Wire Proportional Chambers (LPMWPCs) (Breskin, Chechik, and Zwang 1979; Assamagan et al. 1999; Margaryan et al. 2010).

Experimental setup

An experimental setup based on the LPMWPCs was developed in order to investigate ionization energy losses of low-energy alpha particles in Methylal. The alpha source employed in the present study was a planar, 0.14 mg/cm^2 thick, 30×30 mm^2 ^{239}Pu source. This has three lines: 11% - 5.099, 20% - 5.137 and 69% - 5.150 MeV. The geometry of the setup is shown in Fig. 67. It consists of two MWPC1 and MWPC2 units, mounted at 5.5 cm distance from each other and detected the α-particles, which were collimated by 7 mm holes bored in 100 μm Mylar ($C_{10}H_8O_4$) absorbers.

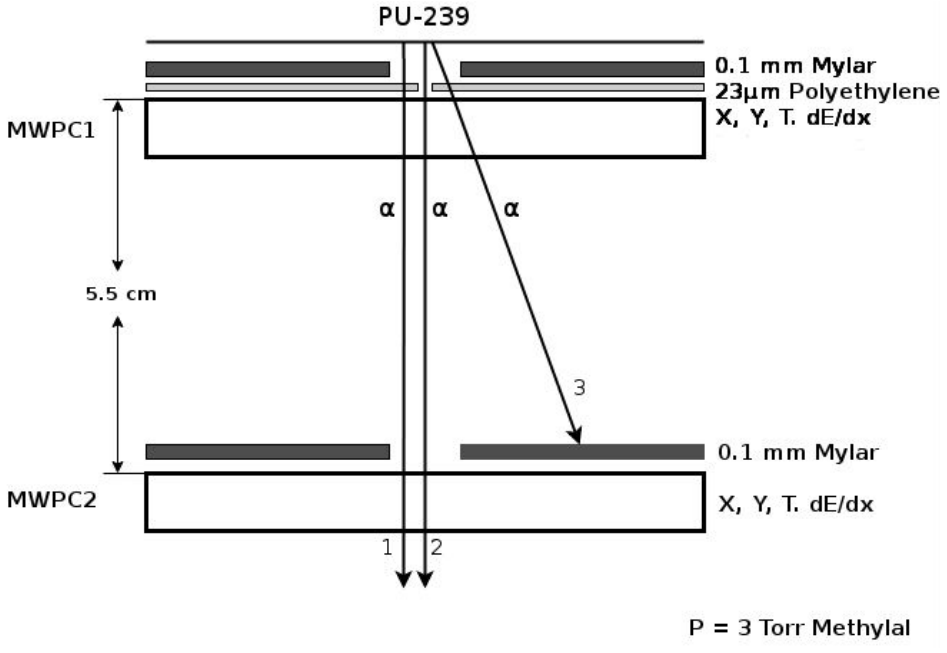

Fig. 67. The schematic view of the experimental setup. 1- alphas that pass through 23 μm Polyethylene and 5.5 cm 3 Torr Methylal, 2 - alphas that pass through Methylal, 3 - alphas that are absorbed.

The structure and operational mode of LPMWPCs are described in (Ajvazyan et al. 2018), it is a multi-wire proportional chamber with the active area of 3×3 cm^2. The time of flight(TOF) and *dE/dx* distributions from the MWPCs were recorded. In these studies, data was also obtained for reduced α-particle energies, by placing a polyethylene absorber between the first Mylar collimator and the MWPC1. In this case, the holes in the Mylar collimators had 7 mm diameter and the polyethylene$(C_2H_4)_n$ absorber had a 3 mm hole, which allowed simultaneous detection of incident α-particles and α-particles after passing through the polyethylene moderator.

The electronics and logic of signal extraction and processing.

The analog signals from anode1(A1) and anode2(A2) of the MWPC1 and MWPC2 modules were registered with Picoscope 6407 series, with 5 GS/s and 1 GHz analog bandwidth. As the Picoscope voltage range is 100mv the amplified signals which reach about 500V were attenuated with 15 and 10 dB attenuators for A2 and A1 channels respectively. The trigger was formed with the A2 signal and signals with the minimum amplitude of less than -5 mV were registered. The average signals of ADC1 and ADC2 are depicted in (Fig. 68). The connection between Picoscope and the Labview was performed with the help of Picoscope GitHub

examples (Pico Technology Ltd 2014-2017). The signal waveform pairs were written event by event in a CSV file.

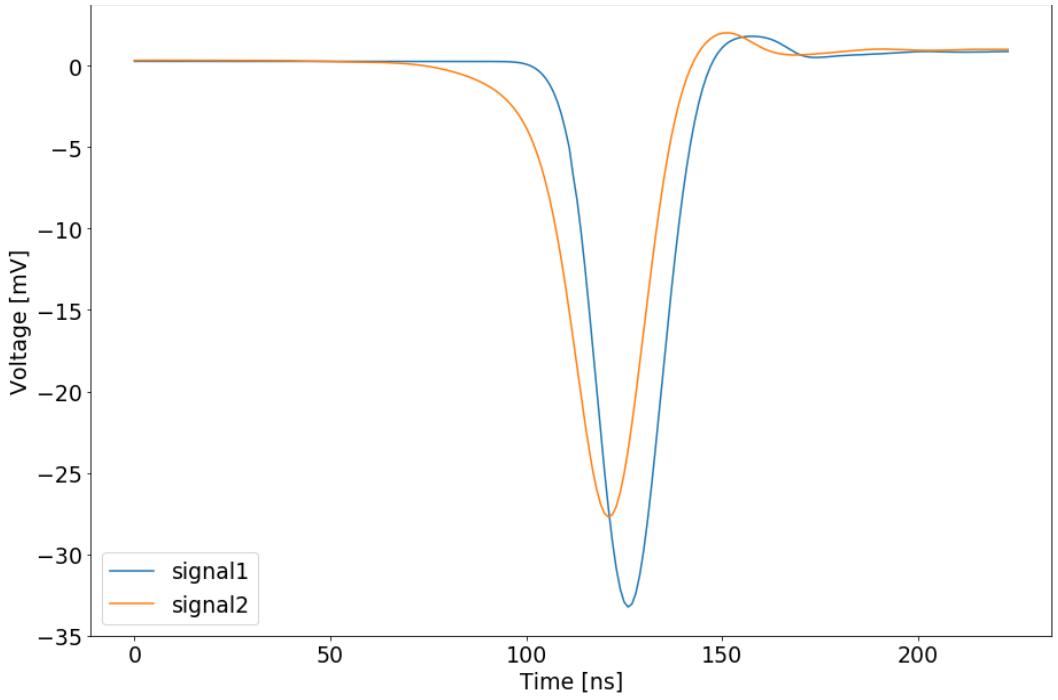

Fig 68. The average signals from the anodes: signal1 and signal2 are from A2 and A1 respectively.

The detector signals were mostly good signals, but to be sure that bad signals or noises are eliminated and they can't effect to the distribution of the TOF and the signal amplitude a subtle method was applied. As we know from the shape of the signals, a perfect signal should be like gaussian function, and the alternation from the function means that it is potentially a noise. Every signal pair were fitted with the Gaussian function and the chi-square was calculated with the help of Python software package and Gaussian Model from lmfit library (Fig. 69).

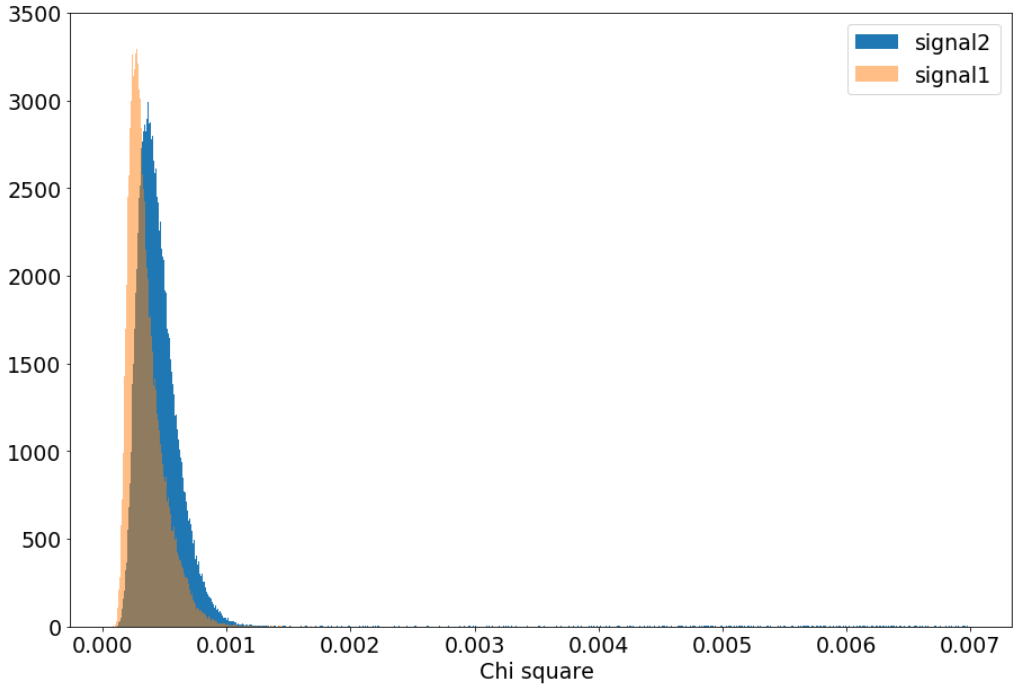

Fig 69. The distribution of Chi-square: signal2 is from A1 and signal1 from A2 signals.

The shape of the signals which has chi-square bigger than 0.001 were mostly bad signals or noise coming from either drastic changes of the voltage in the electrical network, or from other charged particles with less ionization energy. Thus the 0.001 threshold was applied and the only good signals were chosen to obtain maximum good resolution.

For digitization of the signal waveform (ADC- Analog to digital converter), the minimum of the fitted Gaussian peak function was taken. The ADC of each signal corresponds to deposited energy of the alpha particles in the Methylal gas which is respectively proportional to the energy of the alpha particle. So the distribution of ADC will show the overall deposited energy in the detector (Fig 70.). On the other hand, the difference of the argmins of the ADC's for A1 and A2 signals will determine the TDC (Time to digital converter) which is the TOF of the alpha

particles. From TOF we can simply get the velocity of alpha particles consequently composing the energy distribution.

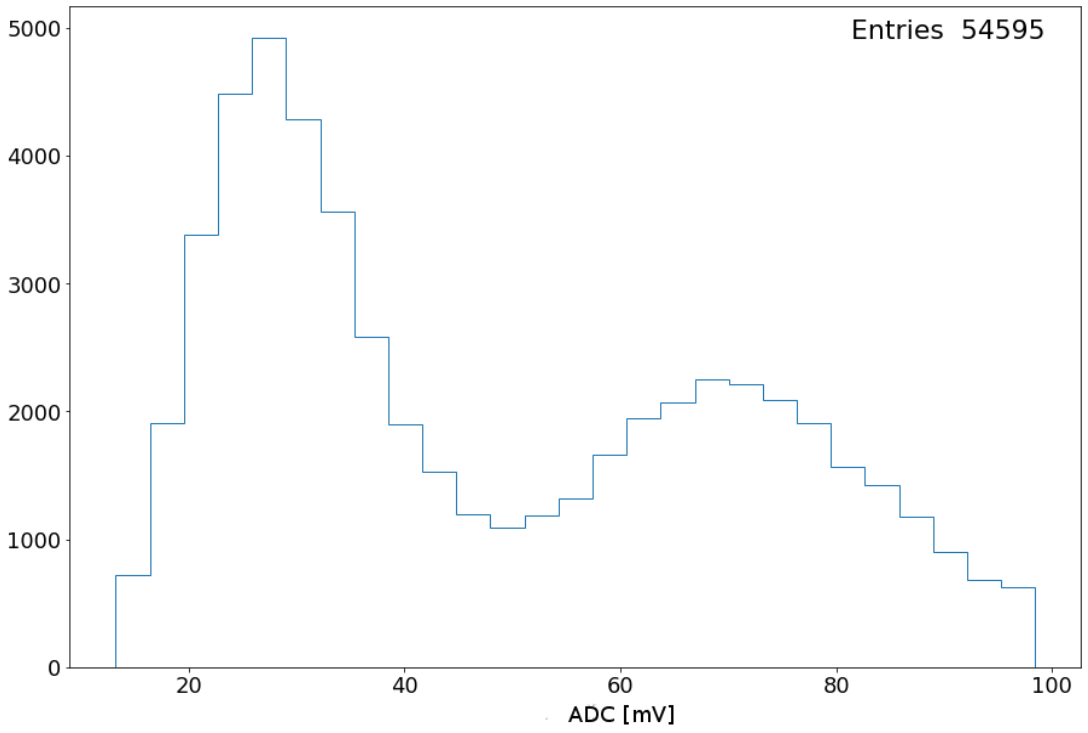

Fig 70. The ADC distribution of the A2 signal in mV.

We can observe two peaks in Fig. 71. The first one is the alpha particles that passed directly through the Methylal gas without interacting with polyethylene moderator, and the second peak is alphas after interacting with polyethylene. In order to calibrate the energy from the time information, the mean of the first peak has been adjusted to the 5.15 MeV, which is the mean energy of alpha particles emitted from ^{239}Pu source.

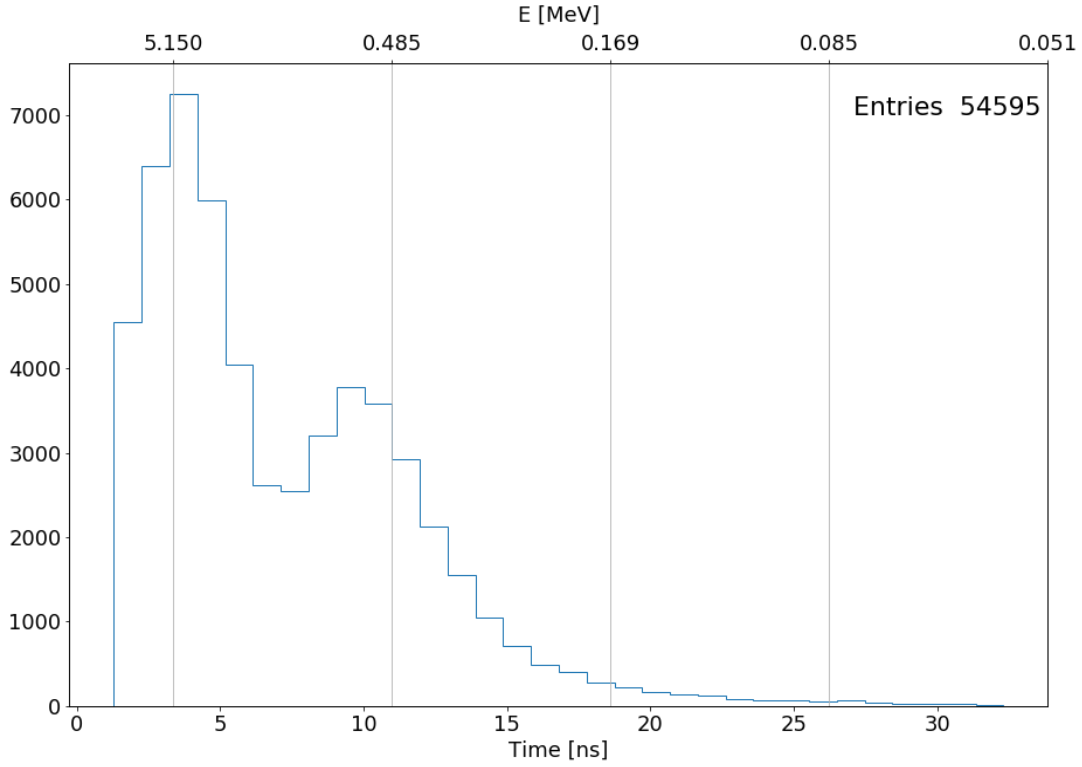

Fig 71. The TOF distribution of alpha particles. Lower axis shows the time of flight of alpha particles, and upper axis shows their corresponding energies.

The distribution of the TOF was divided into small chunks and for each chunk, ADC distribution was generated. The mean of the ADC distribution then was picked which is, in fact, the *dE/dx* for that given chunk of time(therefore Energy). The errors of the experimental points were determined as the $\sigma/\sqrt{n}$ where the σ is the standard deviation and n is the number of events for each chunk. The errors turned out to be neglectable with respect of the absolute value of ADC. Consequently for every Energy the *dE/dx* was determined, nevertheless, it needs to be calibrated because the absolute value of the peaks has no meaning. In the experimental data, the absolute value of the ADC corresponding to the 5.15 MeV is 25(Fig. 72).

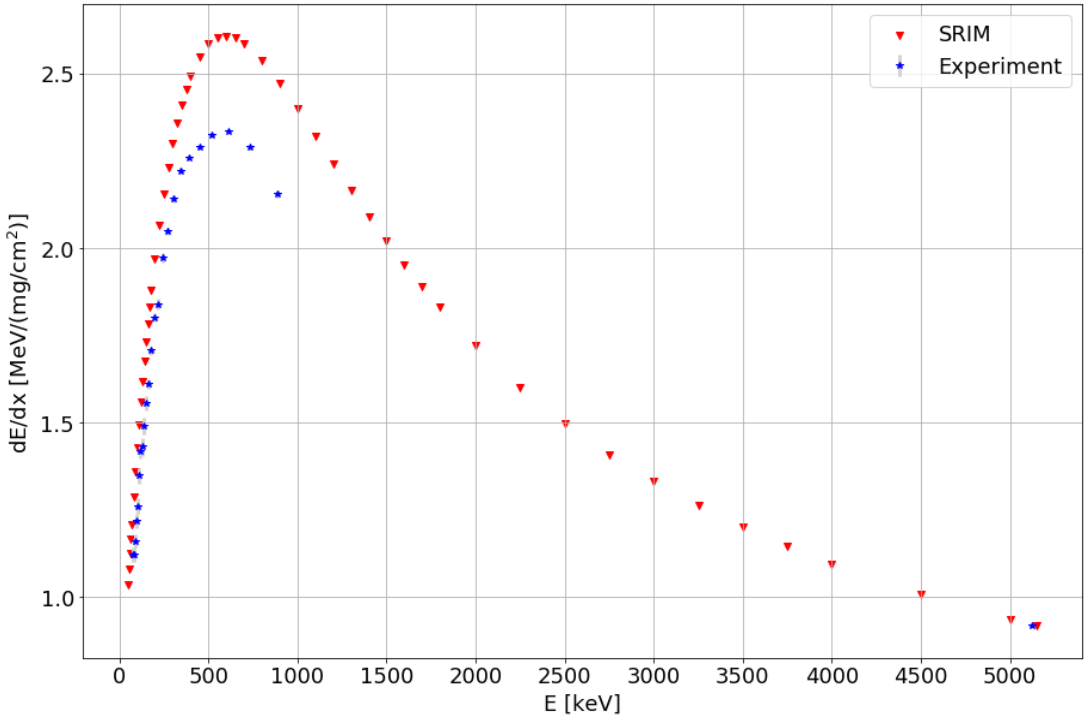

Fig 72. The energy loss of the alpha particles in methylal. Red-triangle is the SRIM data and the blue-star is the experimental data(In the experimental value of 5.15 Mev that is colored in the blue star is a little bit shifted to be distinguishable from the red triangle)

To calibrate the ADC values, the corresponding v(25mV) should be scaled to the 0.91 MeV/(mg/cm^2) which is the corresponding energy loss of the alpha particles in methylal according to the SRIM software dataset (ZIEGLER and F n.d.)(we trust SRIM at this energies): see the red triangle in 5.15 Mev in Fig 72. Henceforth, we transform each ADC values in the following way: *ADC*0.91/25* and obtain *Mev/(mg/cm^2)* units. We then employed the stopping powers provided by the SRIM-2013, which calculated the stopping and range of ions (10 eV–2 GeV/amu) into matter using a quantum mechanical treatment of ion-atom collisions (the manual of SRIM refers to the moving atom as an ‘‘ion’’, and all target atoms as ‘‘atoms’’). On the main menu of the SRIM-2013 software, the stopping and range table was selected. In this table, we selected ‘‘Helium’’ in the ion row and added $C_3H_8O_2$ to be

the target with no Bragg correction. Finally, we clicked ‘‘Calculate Table’’ and a list of total stopping powers and estimates of the range for alpha particles in methylal was generated. The SRIM dataset results alongside with the empirical data are depicted in Fig.72.

The results of the experimental data show that the SRIM dataset in low energy regions has inaccuracy and shows about 5-10% more than those in the experiment. This means that alpha particles have higher ranges than it is estimated in SRIM dataset.

More precise experiment is under development where we planned to use different gases. Besides, in the current experiment only A1 signals were used for ADC distribution, the A2 signals are slightly larger than A1 which we do not understand and will try to explain in upcoming papers.

Conclusion

A new active target has been developed to be used to investigate low energy nuclear reactions. It is based on the low-pressure MWPC technique and Si detectors. Methylal ((OCH3)2CH2) at a pressure of a few Torr serves as a working gas for MWPC operation. The detector system has been tested in lab condition with alpha and betta sources, as well as using bremsstrahlung photon beam from MeV Electron beam. The time and position resolutions of the MWPC for ~5 MeV α-particles are about 450 ps and less than 1.5 mm, respectively. The detector system has a modular structure. Each of four modules consists of two MWPC units and a SSD detector, which allows the measurement of trajectories, velocities and energies of low-energy,

highly-ionizing particles, such as α-particles or light nuclei. The active area of the MWPC units and SSD detector is 30×30 mm^2. The active-target MWPC can also be operated using hexane (C_6H_{14}) at a few Torr pressure, which produces even better timing and position resolution for the MWPC. The active-target detector system filled with hexane can be used for evaluation of the background from carbon nuclei in methylal. Both hexane and methylal give an alpha particle detection threshold of about 50 keV. It is worth mentioning that for SSD detectors the alpha particle detection threshold is about 400 keV. For heavier ions, such as ^{12}C, the threshold detection energy of the MWPC is around 100 keV.

We are planning to use this active-target technique for measuring $^{16}O(\gamma, \alpha)^{12}C$ reaction cross-sections in the 8–10 MeV photon energy region, at the Yerevan 18 MeV proton cyclotron and at ELI-NP, Magurele, Romania, which produces a monochromatic, polarized photon beams by Compton backscattering of laser photons and LCB γ-ray facilities of HIγS, TUNL, Durham, USA. The advantages of this active-target system include good timing and position resolution, high rate capability, detection and identification of both photodisintegration fragments, and insensitivity to the electromagnetic background. The main disadvantage of this device is the low density of target nuclei, which is due to the low-pressure gas. This drawback can be compensated when using highly-directed, pencil-type LCB γ-ray beams by using a multi module active-target system stacked up to a total length of ~10 m.

It is also proposed to utilize the LPMWPC technique for two-body π^- decay spectroscopy of light hypernuclei. It employs a magnetic spectrometer for precise measurement of the decay pion momentum in conjunction with a detector of the recoiling nucleus for separation of produced hypernuclei from background. Low-pressure MWPCs are proposed as the position and time sensitive devices for low-energy recoil detection. The desirable features of this recoil detector include: good timing and position resolution; high rate capability; identification of heavy

recoils; large acceptance ≥0.1; insensitivity to electromagnetic background and minimum ionizing particles. Experiments of this type can be carried out using electron, photon or proton beams and Li, Be, or C targets. Produced hyperfragments such as $\Lambda 3H$ and $\Lambda 4H$, $\Lambda 6H$ and $\Lambda 8H$ exit the target and decay in the vacuum. The monochromatic momentum spectrum of the produced pions is broadened by kinematics, but the absolute value is not changed by any secondary process such as ionization energy losses before detection in the magnetic spectrometer. Therefore average values of the π^- momenta will reproduce exactly the two-body decay kinematics, so that they can be used for accurate determination of the binding energies of Λ-particles in light hypernuclei. This is especially crucial for the lightest hypernucleus, $\Lambda 3H$, for which the binding energy of the Λ-particle is about 0.130 MeV.

The LPMWPC are also perfect devices for carrying out measurements of *dE/dx* of low energy heavy particles. Especially we have measured α-particles in Methylal using a position sensitive LPMWPC system with active area 3×3 cm^2. A thorough measurement and analysis were performed using Picoscope data acquisition and python software to filter noise from the pure signal. The results show that if the energy loss of the alpha particles in SRIM-2013 dataset reduced by 10% they would agree satisfactorily with the experimental data. This detector system with compact picoscope DAQ can be used as a perfect University lab device for students to measure ionization energies of alpha particles in different gases.

References

1. Achenbach, Patrick, Sebastian Bleser, Josef Pochodzalla, and Marcell Steinen. 2018. “High-Precision Measurement of the Hypertriton Mass.” In *Proceedings of XVII International Conference on Hadron Spectroscopy and Structure — PoS(Hadron2017)*, 207. Trieste, Italy: Sissa Medialab.
2. Achenbach, P., C. Ayerbe Gayoso, J. C. Bernauer, R. Böhm, D. Bosnar, M. Bösz, L. Debenjak, et al. 2011. “Strange Hadrons – Strangeness in Strongly Interacting Particles.” *The European Physical Journal Special Topics*. https://doi.org/10.1140/epjst/e2011-01496-9.
3. Achenbach, P., F. Schulz, S. Aulenbacher, J. Beričič, S. Bleser, R. Böhm, D. Bosnar, et al. 2016. “Experimental Investigations of the Hypernucleus Λ4H.” *EPJ Web of Conferences* 113: 07001.
4. Adsley, P., R. Neveling, P. Papka, Z. Dyers, J. W. Brümmer, C. Aa. Diget, N. J. Hubbard, et al. 2017. “CAKE: The Coincidence Array for K600 Experiments.” *Journal of Instrumentation*. https://doi.org/10.1088/1748-0221/12/02/t02004.
5. Afanas’ev, S. N., and A. F. Khodyachikh. 2004. “TOTAL AND PARTIAL CROSS SECTIONS OF THE 12C (γ, 3α) REACTION.” http://vant.kipt.kharkov.ua/ARTICLE/VANT_2004_5/article_2004_5_14.pdf.
6. Ahlen, Steven P. 1980. “Theoretical and Experimental Aspects of the Energy Loss of Relativistic Heavily Ionizing Particles.” *Reviews of Modern Physics* 52 (1): 121–73.
7. Ajvazyan, Robert, John R. M. Annand, Dimiter L. Balabanski, Nersik Grigoryan, Vanik Kakoyan, Patrik Khachatryan, Vachik Khachatryan, et al. 2018. “Active Oxygen Target for Studies in Nuclear Astrophysics with Laser Compton

Backscattered γ-Ray Beams." *Particles* 1 (1): 126–37.

8. Akimov et al., Yu. 1972. *ZhETF,* 62 (4): 1231.
9. Arutyunian, F. R., and V. A. Tumanian. 1963. "The Compton Effect on Relativistic Electrons and the Possibility of Obtaining High Energy Beams." *Phys. Letters* 4. https://www.osti.gov/biblio/4715434.
10. Assamagan, K., K. Baker, G. Bayatyan, R. Carlini, S. Danagoulian, T. Eden, K. Egiyan, et al. 1999. "Time-Zero Fission-Fragment Detector Based on Low-Pressure Multiwire Proportional Chambers." *Nuclear Instruments & Methods in Physics Research. Section A, Accelerators, Spectrometers, Detectors and Associated Equipment* 426 (2): 405–19.
11. Avakian, R. O., A. E. Avetisyan, A. Z. Babayan, K. A. Ispirian, V. Ts Nikoghosian, and S. P. Taroyan. 2010. "Design of a 20 MeV Electron Beamline for Experiments on Radiation Processes." *Journal of Contemporary Physics* 45 (1): 47–49.
12. Balantekin, A. B. 2013. "An Outlook on Nuclear Physics." *arXiv [nucl-Th]*. arXiv. http://arxiv.org/abs/1301.0911.
13. Binon, F., V. V. Bobyr, P. Duteil, M. Gouanere, L. Hugon, M. Spighel, and J. P. Stroot. 1971. "Low Pressure Multiwire Proportional Chambers with High Time Resolution for Strongly Ionizing Particles." *Nuclear Instruments and Methods* 94 (1): 27–28.
14. Bohm, G., J. Klabuhn, U. Krecker, F. Wysotski, G. Coremans, W. Gajewski, C. Mayeur, et al. 1968. "A Determination of the Binding-Energy Values of Light Hypernuclei." *Nuclear Physics B* 4 (6): 511–26.
15. Breskin, A., R. Chechik, and N. Zwang. 1979. "Heavy Ion Timing with Very Low Pressure MWPCs." *Nuclear Instruments and Methods*. https://doi.org/10.1016/0029-554x(79)90316-1.
16. A. Breskin. 1980. "Properties of Very Low Pressure Multiwire Proportional

Chambers.” *IEEE Transactions on Nuclear Science* 27 (1): 133–38.

17. Brun, Rene, and Fons Rademakers. 1997. “ROOT — An Object Oriented Data Analysis Framework.” *Nuclear Instruments and Methods in Physics Research Section A: Accelerators, Spectrometers, Detectors and Associated Equipment*. https://doi.org/10.1016/s0168-9002(97)00048-x.
18. Burbidge, E. Margaret, G. R. Burbidge, William A. Fowler, and F. Hoyle. 1957. “Synthesis of the Elements in Stars.” *Reviews of Modern Physics* 29 (4): 547–650.
19. Cameron, A. G. W. 1959. “Pycnonuclear Reations and Nova Explosions.” *The Astrophysical Journal* 130 (November): 916.
20. Charpak, Georges, and Fabio Sauli. 1979. “Multiwire Proportional Chambers and Drift Chambers.” *Nuclear Instruments and Methods* 162 (1-3): 405–28.
21. Chevallier, P., F. Scheibling, G. Goldring, I. Plesser, and M. W. Sachs. 1967. “Breakup ofO16intoBe8 Be8.” *Physical Review*. https://doi.org/10.1103/physrev.160.827.
22. Curtis, N., S. Almaraz-Calderon, A. Aprahamian, N. I. Ashwood, M. Barr, B. Bucher, P. Copp, et al. 2016. “Be 8+ Be 8 and C 12+ α Breakup States in O 16 Populated via the C 13 (He 4, 4 α) N Reaction.” *Physical Review C: Nuclear Physics* 94 (3): 034313.
23. DiGiovine, B., D. Henderson, R. J. Holt, R. Raut, K. E. Rehm, A. Robinson, A. Sonnenschein, G. Rusev, A. P. Tonchev, and C. Ugalde. 2015. “Bubble Chambers for Experiments in Nuclear Astrophysics.” *Nuclear Instruments and Methods in Physics Research Section A: Accelerators, Spectrometers, Detectors and Associated Equipment*. https://doi.org/10.1016/j.nima.2015.01.060.
24. Dönigus, Benjamin. 2015. “Exotica Production with ALICE.” *EPJ Web of Conferences* 97: 00013.
25. Epelbaum, Evgeny, Hermann Krebs, Timo A. Lähde, Dean Lee, and Ulf-G

Meißner. 2012. “Structure and Rotations of the Hoyle State.” *Physical Review Letters* 109 (25): 252501.

26. Esser, A., S. Nagao, F. Schulz, P. Achenbach, C. Ayerbe Gayoso, R. Böhm, O. Borodina, et al. 2015. “Observation of H Λ 4 Hyperhydrogen by Decay-Pion Spectroscopy in Electron Scattering.” *Physical Review Letters* 114 (23): 232501.
27. Esser, A., S. Nagao, F. Schulz, S. Bleser, M. Steinen, P. Achenbach, C. Ayerbe Gayoso, et al. 2013. “Prospects for Hypernuclear Physics at Mainz: From KAOS@ MAMI to PANDA@ FAIR.” *Nuclear Physics. A* 914: 519–29.
28. Filipescu, D., A. Anzalone, D. L. Balabanski, S. S. Belyshev, F. Camera, M. La Cognata, P. Constantin, et al. 2015. “Perspectives for Photonuclear Research at the Extreme Light Infrastructure - Nuclear Physics (ELI-NP) Facility.” *The European Physical Journal A* 51 (12): 185.
29. Fowler, William A. 1984. “Experimental and Theoretical Nuclear Astrophysics: The Quest for the Origin of the Elements.” *Reviews of Modern Physics*. https://doi.org/10.1103/revmodphys.56.149.
30. Freer, M., H. Fujita, Z. Buthelezi, J. Carter, R. W. Fearick, S. V. Förtsch, R. Neveling, et al. 2009. “2+ Excitation of the C 12 Hoyle State.” *Physical Review C: Nuclear Physics* 80 (4): 041303.
31. Fry, W. F. 1958. “Hyperfragments.” *Annual Review of Nuclear Science* 8 (1): 105–26.
32. Funaki, Y., H. Horiuchi, W. von Oertzen, G. Roepke, P. Schuck, A. Tohsaki, and T. Yamada. 2009. “Concepts of Alpha-Particle Condensation.” *arXiv [nucl-Th]*. arXiv. http://arxiv.org/abs/0912.2934.
33. Funaki, Y., H. Horiuchi, W. von Oertzen, G. Röpke, P. Schuck, A. Tohsaki, and T. Yamada. 2009. “Concepts of Nuclearα-Particle Condensation.” *Physical Review C*. https://doi.org/10.1103/physrevc.80.064326.
34. Funaki, Y., T. Yamada, H. Horiuchi, G. Röpke, P. Schuck, and A. Tohsaki. 2008.

"α-Particle Condensation inO16Studied with a Full Four-Body Orthogonality Condition Model Calculation." *Physical Review Letters*. https://doi.org/10.1103/physrevlett.101.082502.

35. Y. Funak et. al. 2013. "Gas-like Alpha-Cluster States and Condensates in Nuclei." *Journal of Physics. Conference Series* 436 (1): 012004.
36. Funaki, Y., T. Yamada, A. Tohsaki, H. Horiuchi, G. Röpke, and P. Schuck. 2010. "Microscopic Study of4α-Particle Condensation with Inclusion of Resonances." *Physical Review C*. https://doi.org/10.1103/physrevc.82.024312.
37. Gai, M., M. W. Ahmed, S. C. Stave, W. R. Zimmerman, A. Breskin, B. Bromberger, R. Chechik, et al. 2010. "An Optical Readout TPC (O-TPC) for Studies in Nuclear Astrophysics with Gamma-Ray Beams at HIγS1." *Journal of Instrumentation* 5 (12): P12004.
38. Gajewski, W., C. Mayeur, J. Sacton, P. Vilain, G. Wilquet, D. Harmsen, R. Levi Setti, et al. 1967. "A Compilation of Binding Energy Values of Light Hypernuclei." *Nuclear Physics B* 1 (3): 105–13.
39. Gal, Avraham. 2015. "Charge Symmetry Breaking in Λ Hypernuclei Revisited." *Physics Letters. [Part B]* 744 (May): 352–57.
40. Gazda, Daniel, and Avraham Gal. 2016. "Ab Initio Calculations of Charge Symmetry Breaking in the A=4 Hypernuclei." *Physical Review Letters* 116 (12): 122501.
41. Goldberg, L., Muller, E.A., and Aller, L.H. 1960. "The Abundance of the Elements in the Solar Atmosphere." *The Astrophysical Journal. Supplement Series* 5 (45).
42. Goward, F. K., and J. J. Wilkins. 1953. "Cross-Section for the Photodisintegration of Carbon into Three α-Particles." *Proceedings of the Royal Society of London. Series A, Mathematical and Physical Sciences* 217 (1130): 357–75.
43. Greenstein, Jesse L. 1961. "Review on Nuclear Astrophysics." *American Scientist*

49 (4): 449–73.

44. Grigoryan, N., S. Knyazyan, A. Margaryan, G. Marikyan, L. Parlakyan, S. Zhamkochyan, and H. Vardanyan. n.d. “Study of Light Hypernuclei by Pionic Decay at JLab.”
45. Grupen, Claus, and Boris Shwartz. 2008. “Particle Detectors.” https://doi.org/10.1017/cbo9780511534966.
46. Hinode, F., H. Hama, A. Kurihara, A. Miyamoto, M. Mutoh, M. Nanao, M. Oyamada, et al. n.d. “CURRENT STATUS OF A STRETCHER-BOOSTER RING.”
47. Hoyle, F. 1960. “Nucleosynthesis in Supernovae.” *American Astronomical Society*, 565–90.
48. Ikeda, Kiyomi, Hisashi Horiuchi, and Sakae Saito. 1980. “Chapter I. Introduction to Comprehensive Nuclear Structure Study Based on Cluster Correlations and Molecular Viewpoint.” *Progress of Theoretical Physics Supplement*. https://doi.org/10.1143/ptps.68.1.
49. Jurič, Mira, Georg Bohm, J. Klabuhn, U. Krecker, F. Wysotzki, Gh Coremans-Bertrand, Jean Sacton, et al. 1973. “A New Determination of the Binding-Energy Values of the Light Hypernuclei (A□ 15).” *Nuclear Physics B* 52 (1): 1–30.
50. Kaplan, Irving. 1963. *Nuclear Physics*. Addison-Wesley Publishing Company.
51. Khachatryan, V. H. 2019. “Ionization Energy Losses of Low-Energy Alpha Particles in Methylal.” *Armenian Journal of Physics* 12 (1): 124–30.
52. Kotikov et, E. 2002. *Izvestiya Rossiiskoi Akademii Nauk, Seriya Fizicheskaya* 66: 445.
53. Kumagai, H., T. Ohnishi, N. Fukuda, H. Takeda, D. Kameda, N. Inabe, K. Yoshida, and T. Kubo. 2013. “Development of Parallel Plate Avalanche Counter PPAC for BigRIPS Fragment Separator.” *arXiv [physics.ins-Det]*. arXiv.

http://arxiv.org/abs/1311.0215.

54. Li, K. C. W., R. Neveling, P. Adsley, P. Papka, F. D. Smit, J. W. Brümmer, C. Aa Diget, et al. 2017. “Characterization of the Proposed 4- α Cluster State Candidate in O 16.” *Physical Review C: Nuclear Physics* 95 (3): 031302.
55. Loeb, Leonard Benedict. 1960. *Basic Processes of Gaseous Electronics*. University of California Press.
56. Margaryan, A., P. Achenbach, R. Ajvazyan, and J. Annand. 2014. “Delayed Pion Spectroscopy of Hypernuclei.” https://digitalcommons.fiu.edu/cgi/viewcontent.cgi?article=1051&context=physics_fac.
57. Margaryan, A., J-O Adler, J. Brudvik, N. Grigoryan, K. Fissum, K. Hansen, L. Isaksson, et al. 2010. “LOW-PRESSURE MWPC SYSTEM FOR THE DETECTION OF ALPHA-PARTICLES AND FISSION FRAGMENTS.” *Armenian Journal of Physics* 3 (4): 282–91.
58. Margaryan, A., R. Ajvazyan, N. Grigoryan, V. Kakoyan, V. Khacatryan, H. Vardanyan, S. Zhamkochyan, et al. 2019. “Decay Pion Spectroscopy: A New Approach.” *arXiv [nucl-Ex]*. arXiv. http://arxiv.org/abs/1902.03075.
59. Margaryan, A., J. R. M. Annand, P. Achenbach, R. Ajvazyan, H. Elbakyan, R. Montgomery, S. N. Nakamura, et al. 2017. “High Precision Momentum Calibration of the Magnetic Spectrometers at MAMI for Hypernuclear Binding Energy Determination.” *Nuclear Instruments & Methods in Physics Research. Section A, Accelerators, Spectrometers, Detectors and Associated Equipment* 846 (February): 98–105.
60. Margaryan, A., O. Hashimoto, V. Kakoyan, S. Knyazyan, and L. Tang. 2011. “Tagged-Weak π Method.” *Physics of Atomic Nuclei*. https://doi.org/10.1134/s1063778811020141.
61. Margaryan, A., O. Hashimoto, S. Majewski, and L. Tang. 2006. “Study of

Hypernuclei by Pionic Decay." *Letter of Intent LOI-07-001, Jefferson Lab*.

62. Maruhn, J. A., Masaaki Kimura, S. Schramm, P-G Reinhard, H. Horiuchi, and A. Tohsaki. 2006. "\ensuremath{\alpha}-Cluster Structure and Exotic States in a Self-Consistent Model for Light Nuclei." *Physical Review C: Nuclear Physics* 74 (4): 044311.
63. Merkel, Harald. n.d. "EXPERIMENTS WITH INTERNAL TARGETS AT THE MAINZ ENERGY-RECOVERING SUPERCONDUCTING ACCELERATOR."
64. Mornacchi, Edoardo, and A2 collaboration. 2018. "Measurement of the Proton Scalar Polarizabilities at MAMI." *Proceedings of XVII International Conference on Hadron Spectroscopy and Structure — PoS(Hadron2017)*. https://doi.org/10.22323/1.310.0235.
65. Murakami, Akira. 1970. "6Li(γ,t)3He and6Li(γ,pd)3H Reactions." *Journal of the Physical Society of Japan*. https://doi.org/10.1143/jpsj.28.1.
66. Nemura, H., Y. Akaishi, and Y. Suzuki. 2002. "Ab initioApproach Tos-Shell HypernucleiHΛ3,HΛ4,HΛ4e, andHΛ5ewith aΛN−ΣNInteraction." *Physical Review Letters*. https://doi.org/10.1103/physrevlett.89.142504.
67. Ohkubo, S., and Y. Hirabayashi. 2010. "α-Particle Condensate States in 16O." *Physics Letters. [Part B]* 684 (2): 127–31.
68. Overbeck, M., A. Breskin, M. Brügger, R. Chechik, Z. Fraenkel, G. Herrmann, K. Lützenkirchen, S. Polikanov, N. Trautmann, and Th Wilpert. 1990. "A Heavy-Ion Identification System for the Detection of Rare Events." *Nuclear Instruments & Methods in Physics Research. Section A, Accelerators, Spectrometers, Detectors and Associated Equipment* 288 (2): 413–20.
69. Pico Technology Ltd. 2014-2017. https://github.com/picotech/picosdk-ps6000-matlab-instrument-driver.
70. Raduta, Ad R., B. Borderie, E. Geraci, N. Le Neindre, P. Napolitani, M. F. Rivet, R. Alba, et al. 2011. "Evidence for α-Particle Condensation in Nuclei from the

Hoyle State Deexcitation." *Physics Letters. [Part B]* 705 (1): 65–70.

71. Rappold, C., E. Kim, T. R. Saito, O. Bertini, S. Bianchin, V. Bozkurt, M. Kavatsyuk, et al. 2013. "Search for Evidence of Λ 3 N by Observing D+ π- and T+ π- Final States in the Reaction of 6 Li+ 12 C at 2 A GeV." *Physical Review C: Nuclear Physics* 88 (4): 041001.
72. Schuck, P., Y. Funaki, H. Horiuchi, G. Röpke, A. Tohsaki, and T. Yamada. 2013. "Alpha-Particle Condensation in Nuclear Systems." *Journal of Physics: Conference Series*. https://doi.org/10.1088/1742-6596/413/1/012009.
73. Shima, Tatsushi. 2006. "Photonuclear Reactions of Light Nuclei Studied with High-Intensity Real Photon Beams." *PoS*, 176.
74. Suess, Hans E., and Harold C. Urey. 1956. "Abundances of the Elements." *Reviews of Modern Physics* 28 (1): 53–74.
75. Suhara, T., Y. Funaki, B. Zhou, H. Horiuchi, and A. Tohsaki. 2014. "One-Dimensional α Condensation of α-Linear-Chain States." *Journal of Physics. Conference Series* 569 (1): 012008.
76. Sun, Y. L., A. S. Botvina, A. Obertelli, A. Corsi, and M. Bleicher. 2018. "Production of Light Hypernuclei with Light-Ion Beams and Targets." *Physical Review C: Nuclear Physics* 98 (2): 024903.
77. Tang, L., F. Garibaldi, P. E. C. Markowitz, S. N. Nakamura, J. Reinhold, and G. M. Urciuoli. n.d. "Determining the Unknown Λ-N Interaction by Investigating the Λnn Resonance."
78. Tilley, D. R., H. R. Weller, and C. M. Cheves. 1993. "Energy Levels of Light Nuclei A = 16–17." *Nuclear Physics A*. https://doi.org/10.1016/0375-9474(93)90073-7.
79. Tohsaki, Akihiro, Hisashi Horiuchi, Peter Schuck, and Gerd Roepke. 2017. "Status of Alpha-Particle Condensate Structure of the Hoyle State." *arXiv [nucl-Th]*. arXiv. http://arxiv.org/abs/1702.04591.

80. Tohsaki, Akihiro, Hisashi Horiuchi, Peter Schuck, and Gerd Röpke. 2017. “Colloquium: Status of \alpha-Particle Condensate Structure of the Hoyle State.” *Reviews of Modern Physics* 89 (1): 011002.
81. Townsend, J. S. 1915. “Electricity in Gases.” *Journal of the Röntgen Society*. https://doi.org/10.1259/jrs.1915.0049.
82. Townsend JS. 1947. “Electrons in Gases, London, Hutchinson’ssci. Techn.”
83. Vardanyan, H. S. 2017. “Fast, Low-Noise Amplifiers for Low-Pressure Multi-Wire Proportional Chambers.” *Izvestiya Akademii Nauk Armyanskoj SSR, Seriya Tekhnicheskikh Nauk* 70 (3): 350–57.
84. V. N. Maikov, Zh Eksper. 1958. *Teor. Fiz.* 34 (7): 1406.
85. Wakasa, T., E. Ihara, K. Fujita, Y. Funaki, K. Hatanaka, H. Horiuchi, M. Itoh, et al. 2007. “New Candidate for an Alpha Cluster Condensed State in at 400 MeV.” *Physics Letters B*. https://doi.org/10.1016/j.physletb.2007.08.016.
86. Weaver, Thomas A., and S. E. Woosley. 1993. “Nucleosynthesis in Massive Stars and the 12C(α, γ)16O Reaction Rate.” *Physics Reports* 227 (1): 65–96.
87. Weinberg, Steven. 1990. “Nuclear Forces from Chiral Lagrangians.” *Physics Letters B*. https://doi.org/10.1016/0370-2693(90)90938-3.
88. Weller, Henry R., Mohammad W. Ahmed, Haiyan Gao, Werner Tornow, Ying K. Wu, Moshe Gai, and Rory Miskimen. 2009. “Research Opportunities at the Upgraded HIγS Facility.” *Progress in Particle and Nuclear Physics*. https://doi.org/10.1016/j.ppnp.2008.07.001.
89. Wikipedia contributors. 2019. “Townsend Discharge.” Wikipedia, The Free Encyclopedia. March 11, 2019. https://en.wikipedia.org/w/index.php?title=Townsend_discharge&oldid=887290152.
90. Xu, Y., W. Xu, Y. G. Ma, W. Guo, J. G. Chen, X. Z. Cai, H. W. Wang, C. B. Wang, G. C. Lu, and W. Q. Shen. 2007. “A New Study for 16 at the Energies of

Nuclear Astrophysics Interest: The Inverse of Key Nucleosynthesis Reaction 12." *Nuclear Instruments and Methods in Physics Research Section A: Accelerators, Spectrometers, Detectors and Associated Equipment*. https://doi.org/10.1016/j.nima.2007.08.078.

91. Yu, K. N., C. W. Y. Yip, D. Nikezic, J. P. Y. Ho, and V. S. Y. Koo. 2003. "Comparison among Alpha-Particle Energy Losses in Air Obtained from Data of SRIM, ICRU and Experiments." *Applied Radiation and Isotopes*. https://doi.org/10.1016/s0969-8043(03)00201-x.
92. ZIEGLER, and J. F. n.d. "The Stopping and Range of Ions in Matter, SRIM." *Http://www.srim.org/*. Accessed April 18, 2019. https://ci.nii.ac.jp/naid/10027319826/.
93. Ziegler J F And Littmark. 1980. "Handbook of Range Distributions for Energetic Ions in All Elements." *Ed. Pergamon Press, New York* 40 (1): 19–39.
94. Zimmerman, W. R., M. W. Ahmed, B. Bromberger, S. C. Stave, A. Breskin, V. Dangendorf, Th Delbar, et al. 2013. "Unambiguous Identification of the Second 2+ State in C 12 and the Structure of the Hoyle State." *Physical Review Letters* 110 (15): 152502.